The Spatial Distribution of Fatigue Microdamage Accumulation in Cortical Bone and Factors Influencing Fracture Risk

Travis L. Turnbull

Publication Date

23-07-2013

THE SPATIAL DISTRIBUTION OF FATIGUE MICRODAMAGE ACCUMULATION IN CORTICAL BONE AND FACTORS INFLUENCING FRACTURE RISK

A Dissertation

Submitted to the Graduate School

of the University of Notre Dame

in Partial Fulfillment of the Requirements

for the Degree of

Doctor of Philosophy

by

Travis L. Turnbull

Ryan K. Roeder, Director

Graduate Program in Aerospace and Mechanical Engineering

Notre Dame, Indiana

July 2013

THE SPATIAL DISTRIBUTION OF FATIGUE MICRODAMAGE ACCUMULATION IN CORTICAL BONE AND FACTORS INFLUENCING FRACTURE RISK

Abstract

by

Travis L. Turnbull

Human cortical bone, like many engineering materials, exhibits damage and fracture, due to cyclic loading and overloading, such as that experienced by the load-bearing long bones. Unlike engineering materials, bone possesses a unique ability to repair damage and reduce fracture risk. However, in cases such as athletes and military recruits, the rate and extent of damage formation can exceed the rate of repair, resulting in increased fracture risk until the damage is diagnosed and rest prescribed. In the elderly, and especially those afflicted with metabolic bone diseases such as osteoporosis, the rate of bone resorption exceeds the rate of formation of new bone, resulting in reduced cortical thickness, increased intracortical porosity and, thus, increased fracture risk.

The overall objective of this project was to nondestructively investigate the spatial distribution of fatigue microdamage accumulation in cortical bone and factors that, upon interaction with microdamage, influence fracture susceptibility. Contrast-enhanced micro-CT detected increased microdamage in whole rat femora loaded in cyclic three-

point bending relative to non-loaded controls, as well as the volumetric spatial distribution of microdamage relative to the whole bone morphology and non-uniform strain distribution resulting from bending. Spatial correlations between intracortical porosity, elevated mineralization, and fatigue microdamage were investigated by combining, for the first time, sequential, nondestructive, three-dimensional micro-CT measurements of each in cortical bone specimens subjected to cyclic loading followed by an overload to fracture. Microdamage at the fracture initiation site was found to be spatially correlated with intracortical porosity, but not highly mineralized tissue. The new spatial correlation methods were subsequently utilized to investigate the effects of age and loading mode on the fracture susceptibility of human cortical bone specimens. Interestingly, the influence of porosity on the initiation and propagation of microdamage was decreased in elderly (i.e., greater than 80 y/o) versus postmenopausal women donors. The observed spatial correlation between intracortical porosity and microdamage motivated future work exploring statistical predictions of fracture susceptibility based on spatial measurements of intracortical porosity, for example pore area, which predicted fracture susceptibility in a preliminary specimen cohort.

This work is dedicated to all who inspired in me the pursuit of knowledge and provided myriad opportunities for success.

CONTENTS

FIGURES

ABBREVIATIONS

$BaSO_4$	Barium Sulfate
Micro-CT	Micro-Computed Tomography
SV	Stain Volume (measure of microdamage)
TV	Total Volume (inclusive of cortical bone tissue porosity for whole rat femora, but exclusive of medullary volume)
SV/TV	Stain Volume normalized to Total Volume (measure of fatigue microdamage)
BMD	Bone Mineral Density
PV	Pore Volume
LMV	Low Mineral level Volume
HMV	High Mineral level Volume
BV	Bone Volume (exclusive of tissue porosity)
DV	Damage Volume (equivalent to SV)
DV/BV	Damage Volume normalized to Bone Volume (measure of fatigue microdamage)
RDF	Radial Distribution Function (single voxel of origin computation)
PDF	Probability Density Function (normalized two-point correlation function, multiple voxel of origin computation)
Po.Ar	Pore Area (2-D transverse area)

TABLES

ACKNOWLEDGMENTS

I first and foremost acknowledge that I could do nothing without Christ who strengthens me and enables all my efforts—all glory and honor be to the Father, Son, and Holy Spirit who was, and is, and is to come!

My achievements are a direct product of the loving support of my entire family. Heather, thank you for your friendship and eternal love—I love you! Mom, Dad, and Sarina: thank you for inspiring, providing, loving, challenging, and putting up with me all these years—I love you all! To all my grandparents: thank you for your enduring example and the work you constantly perform to better our families—I love you! To all the rest of my numerous and wonderful family members, including my married family and church family: I am blessed to know and call each of you family—thank you for your unfailing support and love, without which I would not have achieved this goal—I love you all!

To the many educators whom I have been blessed to be a pupil: I will never be able to fully express my heartfelt gratitude for your hours and years of service to all students and especially myself—your work is cherished and will never be forgotten!

To my graduate research advisor, Dr. Ryan Roeder: your presence in my life was truly a gift from God and I could not have asked for a better academic father! Your dedication and passion for teaching and research are commendable and are only eclipsed by your care and concern for those around you, especially your research group. Thank

you for instilling in me so many critical skills and abilities! My future, both professionally and personally, has undoubtedly been bettered through your efforts—with the utmost sincerity, thank you!

To the members of my dissertation committee, Drs. Glen Niebur, Diane Wagner, and Matt Ravosa: thank you for your time and efforts on my behalf. This document has been positively influenced by your active service on my committee—thank you!

To all of my colleagues, both past and present, at the University of Notre Dame: thank you for establishing and maintaining a spirit of helpfulness, friendliness, and professionalism. Our times together during social events, intramural sports, puppy play dates, football- and baseball-toss work breaks, hunting and fishing trips, etc. are treasured experiences and enabled me to enjoy life both during and outside of work—thank you! In particular, to the past and present members of Roeder Lab including Matt Landrigan, Justin Deuerling, Ryan Ross, Bob Kane, Tim Conrad, Christina Merrill, Lisa Cole, Matt Meagher, Andy Baumann, and Jenni Tilley: thank you for your individual and collective friendship and the example you set as hard-working, talented researchers.

I am indebted to Josh Gargac and Dr. Glen Niebur for developing, executing, and interpreting the finite element model simulations for the study presented in Chapter 2. Fresh-frozen rat hind limbs used in Chapter 2 were kindly provided by Freimann Life Science Center at Notre Dame. The work in Chapters 3-5 utilized computing resources maintained by the Notre Dame Center for Research Computing.

I am grateful for the funding sources that provided financial support for my graduate work at the University of Notre Dame: the U.S. Army Medical Research and Materiel Command (W81XWH-06-1-0196), through the Congressionally Directed

Medical Research Program Peer-Reviewed Medical Research Program (PR054672), and the Merck, Sharp and Dohme Corporation.

CHAPTER 1:

BACKGROUND

1.1 Hierarchical Structure and Function of Human Cortical Bone

Bones in the human body are of two classifications: cortical and cancellous (or trabecular). Cortical bone forms the hard outer shell of the long bones that provide structural support and enable locomotion via muscle attachments. Trabecular bone is located at the epiphyses of long bones (near the joints) and also comprises bones such as the vertebrae. Human cortical bone is comprised of a hierarchical ordered substructure which has various constituents at size scales ranging from millimeters to nanometers (Figure 1.1).

The smallest structural units of human cortical bone are non-collagenous proteins, Type I collagen molecules, and apatite crystals (Rho *et al.*, 1998). The apatite crystals nucleate within, and are limited in size by, the regularly spaced holes or gaps in and between the collagen molecules. Also, more than half of the apatite crystals may be located in the interfibrillar spaces (Lees and Davidson, 1977). A preferred orientation exists with the *c*-axes (long axes) of the mineral crystals coincident with the long axes of the larger collagen fibrils (Moradian-Oldak *et al.*, 1991). Neighboring collagen molecules are staggered and interconnected by cross-links (Figure 1.2). The apatite crystals and collagen molecules combine to form the next larger structural unit—the mineralized collagen fibril. Many individual collagen fibrils combine to form the larger

collagen fibers. Mineralized collagen fibers assemble into planar, sheet-like arrangements called lamellae (3-7 μm thick). In human cortical bone, an osteon is produced by approximately 15-20 lamellae forming a concentric sheath around a central vascular channel (~50 μm diameter), called a Haversian canal (Rho *et al.*, 1998). Interestingly, the collagen fibers comprising individual lamella are predominantly parallel, while the orientation of adjacent, concentric lamellae is different, often rotated on the order of 30 degrees or more (Nyman *et al.*, 2005). Osteons are the largest substructural units with a diameter of approximately 250 μm and are generally oriented along the long axis of the bone. The remaining volume of bone tissue surrounding osteons is termed interstitial tissue and comprised of older tissue that has not been recently remodeled through normal cellular activity within the bone.

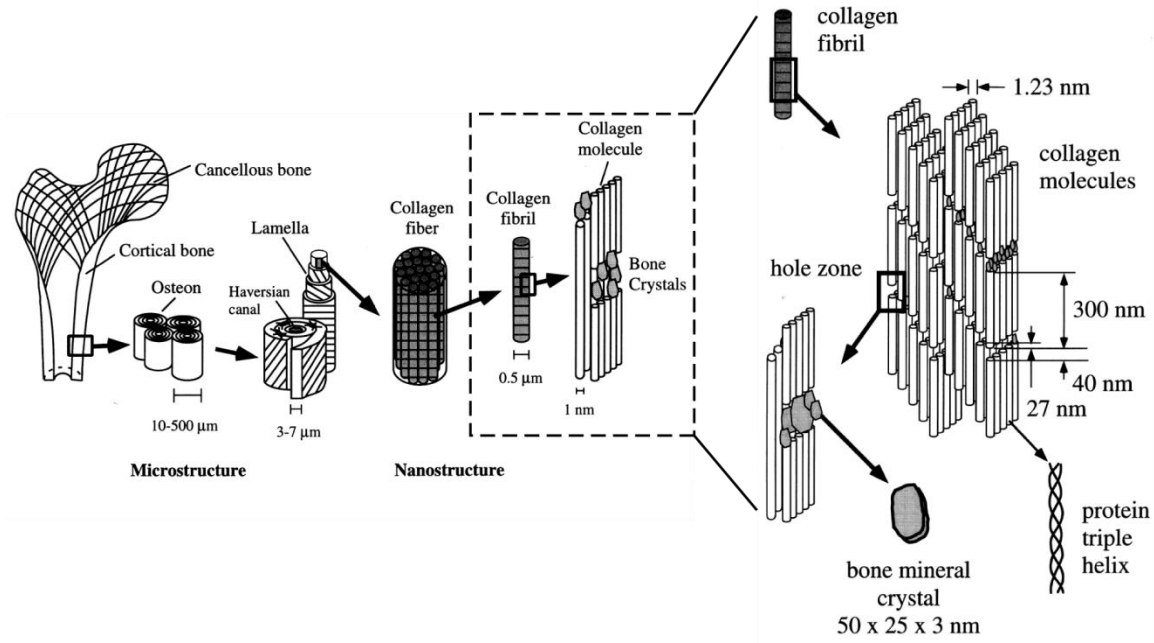

Figure 1.1: The hierarchical, ordered structure of human cortical bone. Adapted from Rho et al., 1998.

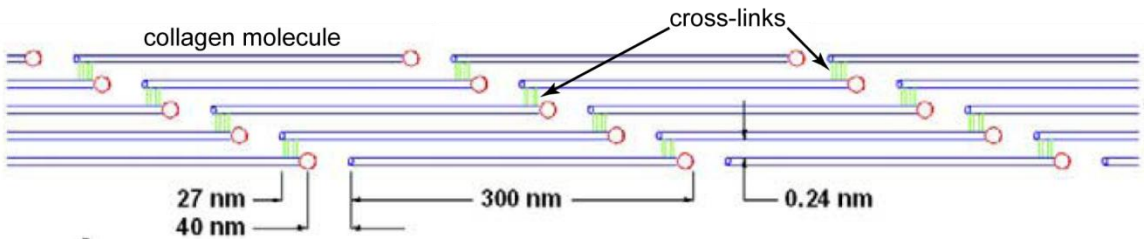

Figure 1.2: Schematic diagram showing cross-links between collagen molecules in a collagen fibril. Adapted from Nyman et al., 2005.

Healthy bones in the human body can adapt their complex hierarchical structure to changes in loading and maintain quality through processes termed modeling and remodeling, respectively (Seeman and Delmas, 2006). Cells specific to bone are responsible for carrying out the modeling and remodeling processes. Osteoclasts and osteoblasts remove and create bone tissue (i.e., extracellular matrix), respectively, and the actions of these cells are coordinated by signaling cells called osteocytes. Bones can respond to altered loading in several ways, one example is increasing the quantity of bone tissue in areas that are subjected to greater loading stress while simultaneously decreasing the quantity of bone tissue in other areas subject to less stress. Modeling typically occurs via periosteal bone formation and endosteal resorption which can result in relatively major changes to the shape and/or structure of bones. An example of this phenomenon was observed in young rats subjected to a unilateral sciatic neurectomy to render one hind limb incapable of supporting any weight (Lanyon, 1980). After 16 months the rats were examined and the tibia of the neurectomized hind limb consistently failed to attain its normal weight, thickness, cross-sectional shape, or longitudinal curvature. This demonstrated that the normal shape and size of bones is a direct response of the modeling process to mechanical stimuli.

Haversian remodeling involves a coordinated process of resorption and formation where older and/or damaged tissue is replaced by new, healthy bone tissue (Burr, 2002; Taylor *et al.*, 2007). Unlike modeling, both resorption and formation occur at the same site within bone during remodeling. As such, the remodeling process is coordinated spatially and temporally (i.e., formation follows resorption) by signaling cells called osteocytes (Klein-Nulend and Bonewald, 2008) (Figure 1.3).

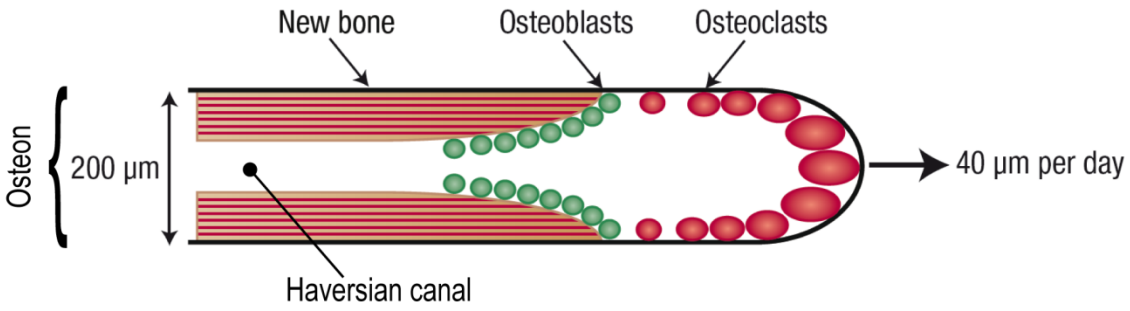

Figure 1.3: Schematic diagram of the remodeling process illustrating a basic multicellular unit (BMU) forming an osteon through the coordinated actions of bone removing cells (osteoclasts), bone forming cells (osteoblasts), and signaling cells (osteocytes). Adapted from Taylor et al., 2007.

1.2 Human Cortical Bone Microdamage

The formation of damage within bone tissue is an unavoidable consequence of daily life; both the extent and consequences of damage increase with factors such as activity level (Matheson *et al.*, 1987; Bennell *et al.*, 1999; Armstrong III *et al.*, 2004; Valimaki *et al.*, 2005) and aging (Schaffler *et al.*, 1995; Norman *et al.*, 2008). Microdamage in human cortical bone tissue occurs in the form of microcracks and/or diffuse damage as a result of repetitive (fatigue) loading both *in vivo* (Frost, 1960; Zioupos, 2001; Norman *et al.*, 2008) and *in vitro* (Zioupos *et al.*, 1996; Akkus *et al.*,

2003; Landrigan *et al.*, 2011). Microdamage has been suggested to initiate as a defect at the level of the collagen fibrils, which could involve a debonding of the fiber-matrix interface, disruption of the mineral-collagen assembly, or collagen fiber failure (Burr *et al.*, 1997). These sub-microscopic voids eventually accumulate and coalesce as a result of continued loading to form microcracks which are of a size large enough to be penetrated by dyes or contrast agents and observed at low magnification (< 250×) by microscopy and other imaging modalities.

Microcracks are predominantly observed within the older, more highly mineralized interstitial tissue of cortical bone (Schaffler *et al.*, 1995; Norman and Wang, 1997; Wasserman *et al.*, 2005) due to its more brittle behavior (Burr *et al.*, 1988; Raum *et al.*, 2006), but can also be found near osteonal cement lines (Schaffler *et al.*, 1995). This suggests that crack initiation occurs more readily in interstitial tissue, compared to recently remodeled secondary osteons. In contrast to diffuse damage, which has been described as a network of very fine and short cracks visible only at high magnification (Boyce *et al.*, 1998), microcracks are larger, sharper, linear cracks, approximately 100-500 μm in length and approximately 1 μm in width (Frost, 1960; Schaffler *et al.*, 1994; Nyman *et al.*, 2005). The three-dimensional (3-D), elliptical morphology of microcracks (Fazzalari *et al.*, 1998; O'Brien *et al.*, 2000; Mohsin *et al.*, 2006a) requires that consideration must also be given to the orientation (e.g., perpendicular or parallel to the crack plane) in which microdamage is observed since an individual microcrack could appear to be either a microcrack or diffuse damage (Voide *et al.*, 2009).

The accumulation of microdamage in cortical bone tissue has been shown to adversely affect mechanical properties by decreasing the elastic modulus (Schaffler *et al.*,

1989; Pattin *et al.*, 1996; Burr *et al.*, 1998), fracture toughness (Norman *et al.*, 1998; Diab and Vashishth, 2005), and ultimate strength (Hirano *et al.*, 2000; Zioupos, 2001). These contributions to the reduction of the mechanical integrity of bones may increase the risk of fatigue (overuse) fractures in active individuals or fragility (overload) fractures in the elderly population.

1.3 Clinical Significance of Microdamage

Microdamage has been implicated in clinical fracture susceptibility for a diverse population including active individuals, the elderly, and individuals receiving antiresorptive pharmaceutical treatments for osteoporosis. Microdamage forms as an unavoidable consequence of the cyclic loading and unloading of bones during daily physical activities and accumulates with age (Schaffler *et al.*, 1995; Norman *et al.*, 2008). Normal remodeling processes mediate the accumulation of microdamage by removing damaged tissue and forming new tissue (Burr, 2002; Taylor *et al.*, 2007). Bone fractures have been hypothesized to occur when the rate of microdamage formation exceeds the rate of repair by remodeling (Martin, 1995).

In the case of active individuals, such as runners, ballet dancers, military recruits, etc., the remodeling response may lag behind the rate of damage formation (Matheson *et al.*, 1987). For these individuals, periods of inactivity are necessary to allow damaged bone to be remodeled. Similarly, aging can result in imbalanced remodeling activity (i.e., the rate of bone formation decreases relative to the rate of resorption) such that the density of microdamage may not be reduced in the bones of elderly individuals (Schaffler *et al.*, 1995; Norman *et al.*, 2008). This reduction in the rate of damage repair and

corresponding increase in microdamage density may be further exacerbated by pharmaceutical treatments for osteoporosis which suppress remodeling in an attempt to preserve the remaining bone mass (Hirano *et al.*, 2000; Chapurlat and Delmas, 2009). Therefore, the risk of an insufficiency or fragility fracture resulting from a standing fall or otherwise normal activity is increased in bone tissue weakened by aging, osteoporosis, or related bone diseases.

The societal burden associated with bone fractures is far-reaching, including patient pain/discomfort, rehabilitation time, reduced mobility, possible complications and medical costs. In 2005, osteoporosis-related fractures resulted in $17 billion in direct medical costs in the United States and the economic burden over the next two decades was estimated at $474 billion (Burge *et al.*, 2007). Among persons suffering hip fractures, the mortality rate was reported to be as high as 25%, and 9% higher than an age-matched population, within the first 6 months following fracture (Leibson *et al.*, 2002). In 1999, stress fractures in military recruits were estimated to cost the United States Department of Defense in excess of $10 million annually in direct medical costs and lost duty (MOMRP Fact Sheet, 1999).

Current clinical assessment for fracture risk due to osteoporosis includes the identification of common risk factors and measurement of the projected areal bone mineral density (BMD) using dual-energy X-ray absorptiometry (DEXA) (Genant *et al.*, 1996; Placide and Martens, 2003). Although DEXA has proven useful in predicting fracture risk in postmenopausal women, approximately one-half of fractures occur in patients with BMD measured to be above the threshold for clinical diagnosis of osteoporosis (Siris *et al.*, 2001). In addition to a lack of specificity, DEXA measurements

also lack sensitivity—more than half of diagnosed patients do not suffer a fracture (Marshall *et al.*, 1996).

Stress fractures are similarly, if not more, difficult to diagnose to the extent that there currently exists no robust diagnostic method. For example, diagnosis often requires consideration of patient history in combination with the results of various imaging methods (Buckwalter and Brandser, 1997). X-ray radiographs can be normal for up to four weeks after a patient becomes symptomatic; bone scans employ radiolabeled contrast agents that are nonspecific for damage; computed tomography (CT) can be limited in resolution; and magnetic resonance imaging (MRI) lacks specificity. Furthermore, clinical stress fractures often present symptoms and radiographic findings that mimic multiple other disorders. As such, undiagnosed patients remain at risk for increased injury, including complete bone fracture (Buckwalter and Brandser, 1997).

1.4 Imaging Microdamage

Various methods have been developed and employed to observe microdamage in bone tissue in an attempt to better understand the role microdamage plays in bone fractures. Most have historically required the destructive and time intensive task of preparing two-dimensional (2D), histological sections. These histological methods have utilized different contrast agents to aid microdamage detection and differentiation from artifactual damage. Various methods and contrast agents have included: transmitted light or epifluorescence microscopy using basic fuchsin stain (Frost, 1960; Burr and Stafford, 1990; Burr and Hooser, 1995; Lee *et al.*, 1998); epifluorescence microscopy using chelating fluorochromes (Lee *et al.*, 2000; O'Brien *et al.*, 2002; Parkesh *et al.*, 2007;

Parkesh *et al.*, 2009); and backscattered electron microscopy using a lead-uranyl acetate stain (Schaffler *et al.*, 1994).

Variations on these methods have been employed to bridge the gap between 2D and 3-D imaging. Damaged tissue labeled with fluorochromes and imaged with laser scanning confocal microscopy showed enhanced depth of focus for limited 3-D imaging (Zioupos and Currey, 1994; O'Brien *et al.*, 2000). Other techniques, such as serial sectioning of damaged tissue labeled with fluorochromes, enabled the reconstruction of 3-D images from sequential 2D images (Mohsin *et al.*, 2006a; Bigley *et al.*, 2008). However, none of these methods are able to image microdamage nondestructively.

Therefore, 3-D, nondestructive imaging methods for microdamage have been investigated. *In vivo* positron emission tomography using a sodium fluoride tracer was used to detect fatigue microdamage in a rat forelimb (Li *et al.*, 2005; Silva *et al.*, 2006); however, the radionuclide tracer lacked specificity since fluoride uptake is also increased by any factor that increases blood flow or exposed bone mineral surface (Blau *et al.*, 1972; Genant *et al.*, 1974). Synchrotron radiation computed tomography (SRCT) using high energy, monochromatic X-rays has shown an impressive ability to directly image microcracks in bone tissue (Nalla *et al.*, 2005); however, SRCT has a number of limitations including availability, small specimen sizes, and long image acquisition times. Alternatively, micro-computed tomography (micro-CT) instruments are commercially available and currently provide sufficient resolution (approximately 10 μm) for the detection of contrast-enhanced microdamage using lower energy, polychromatic X-rays.

Contrast-enhanced micro-CT has enabled 3-D, non-destructive *in vitro* detection of microdamage smaller than the detection limits of most benchtop micro-CT systems.

The contrast agent must exhibit increased X-ray attenuation relative to the extracellular matrix of bone. Contrast agents have included: iodinated molecules (Lee *et al.*, 2003; Parkesh *et al.*, 2006), precipitated lead sulfide (Leng, 2006; Tang and Vashishth, 2007), precipitated barium sulfate ($BaSO_4$) (Wang *et al.*, 2007; Leng *et al.*, 2008; Landrigan *et al.*, 2010; Landrigan *et al.*, 2011; Turnbull *et al.*, 2011), and preliminary work with functionalized gold nanoparticles (Ross and Roeder, 2010; Zhang *et al.*, 2010; Ross and Roeder, 2011). Lead-based staining methods were adapted from previous use as a histological stain for electron microscopy (Schaffler *et al.*, 1994); however, these stains exhibited limited penetration into bulk specimens (4 mm thick) of cortical bone (Leng, 2006). Moreover, lead salts have no potential for use *in vivo* since they are highly toxic and are hazardous to the environment (Swanson *et al.*, 1997).

Barium sulfate ($BaSO_4$) has been utilized as a contrast agent for labeling microdamage based on current clinical use as a contrast agent for X-ray imaging of the gastrointestinal tract and as a radiopacifier in bone cement. Precipitated $BaSO_4$ has been shown to label microdamage in bulk specimens of both cortical (Leng *et al.*, 2008; Landrigan *et al.*, 2011; Turnbull *et al.*, 2011) and trabecular bone (Wang *et al.*, 2007), as well as dentin (Landrigan *et al.*, 2010). The main limitation of $BaSO_4$ labeling is that precipitation occurs within damaged tissue, cracks and vasculature. However, a recent study validated contrast-enhanced micro-CT with $BaSO_4$ against the current gold-standard, optical microscopy with basic fuchsin staining (Landrigan *et al.*, 2011).

1.5 Research Objectives

The overall objective of this research was to non-destructively investigate the 3-D spatial distribution of fatigue microdamage accumulation in cortical bone and its role in fracture susceptibility. Chapter 2 presents the first application of $BaSO_4$ labeling and contrast-enhanced micro-CT to a whole bone rather than machined tissue specimens. Contrast-enhanced micro-CT was able to detect increased microdamage in whole rat femora loaded in cyclic three-point bending relative to non-loaded controls, as well as the volumetric spatial distribution of microdamage relative to the whole bone morphology and non-uniform strain distribution resulting from bending.

In Chapter 3, the spatial correlation between intracortical porosity, mineralization levels, and fatigue microdamage was investigated by combining, for the first time, sequential, nondestructive, 3-D micro-CT measurements of each in cortical bone specimens subjected to cyclic loading followed by an overload to fracture. These novel methods allowed identification of the fracture initiation site in specimens and the calculation of spatial correlation between microstructural features. Fatigue microcracks that initiated fracture upon overload were found to be spatially correlated with elevated intracortical porosity but not elevated mineralization. In contrast, overall microdamage was randomly distributed within the extracellular matrix of cortical bone. These results suggested that human cortical bone is largely tolerant of microdamage which is generally compartmentalized within interstitial tissue, but a single microcrack of sufficient size located in spatial proximity to intracortical porosity can compromise fracture resistance.

Chapter 4 utilized the novel methods developed in Chapter 3 to investigate cortical bone fracture susceptibility differences due to factors including donor age and

fatigue loading mode. Fatigue loading mode exhibited minimal influence on the fracture susceptibility between fatigue loaded groups. Overall, spatial correlations revealed intracortical porosity was located in spatial proximity to all damage sites, including the damage that initiated fracture. This trend was exhibited in specimens from younger (50s) postmenopausal donors, but not older (80s) donors, suggesting intracortical porosity may have a greater effect on the fracture susceptibility of tissue from younger postmenopausal donors compared to older donors.

Chapter 5 applied the results from Chapters 3 and 4 to explore the feasibility of predicting cortical bone fracture susceptibility from global and spatial measurements of microstructural features, especially intracortical porosity. As a global measure, intracortical porosity exhibited a stronger correlation with compromised mechanical properties compared to high mineralization. On the other hand, spatial measurements of intracortical porosity (e.g., the pore size or area) were demonstrated to be feasible for statistical assessment of fracture susceptibility in cortical bone.

CHAPTER 2:

DETECTION OF FATIGUE MICRODAMAGE IN WHOLE RAT FEMORA USING CONTRAST-ENHANCED MICRO-COMPUTED TOMOGRAPHY[1]

2.1 Introduction

Microdamage can accumulate in cortical bone tissue with aging and/or repetitive mechanical loading (Schaffler *et al.*, 1995; Burr *et al.*, 1997; Norman and Wang, 1997; O'Brien *et al.*, 2003). The accumulation of microdamage in machined specimens *in vitro* has been shown to adversely affect mechanical properties, including the elastic modulus (Schaffler *et al.*, 1989; Pattin *et al.*, 1996) and fracture toughness (Norman *et al.*, 1998). Therefore, microdamage has been associated with increased fracture susceptibility, including stress fractures in active individuals, fragility fractures in the elderly, and the effects of long-term antiresorptive treatments for osteoporosis (Burr *et al.*, 1997; Chapurlat and Delmas, 2009). However, relatively few studies have investigated fatigue microdamage accumulation in whole bones, no matter whether loaded *in vitro* (Forwood and Parker, 1989; Burr *et al.*, 1998; Danova *et al.*, 2003) or *in vivo* (Silva *et al.*, 2006; Uthgenannt and Silva, 2007).

Microdamage in bone tissue is conventionally imaged and quantified using histological sections, which are inherently invasive, destructive, tedious and two-

[1] This chapter appeared in: Turnbull, T.L., *et al*., 2011. Journal of Biomechanics 44, 2395-2400.

dimensional (Lee *et al.*, 2003). A method for nondestructive, three-dimensional (3-D) imaging would enable spatial correlation of microdamage accumulation with variations in the mechanical loading (magnitude and stress state), bone mineral density, microarchitecture, and morphology of whole bones. Moreover, nondestructive, 3-D damage detection could also reduce the time and labor required by histological methods.

Contrast-enhanced micro-computed tomography (micro-CT) was recently demonstrated to enable nondestructive, 3-D detection of microdamage accumulation in cortical and trabecular bone specimens *in vitro* (Wang *et al.*, 2007; Leng *et al.*, 2008; Landrigan *et al.*, 2011). Measurements of damage accumulation by contrast-enhanced micro-CT were strongly correlated with histological measurements using basic fuchsin, validating the new methods (Landrigan *et al.*, 2011). However, previous studies using contrast-enhanced micro-CT only investigated geometric, machined specimens. Intra- and inter-specimen variation in whole bone morphology can lead to non-uniform variation in the tissue strain distribution (e.g., Kotha *et al.*, 2004), which would be expected to influence microdamage accumulation. Therefore, the objective of this study was to detect the presence, spatial location, and accumulation of fatigue microdamage in whole rat femora using micro-CT with a $BaSO_4$ contrast agent. Whole rat femora were loaded in cyclic three-point bending *in vitro* to predetermined levels of secant modulus degradation, stained with $BaSO_4$, and imaged by micro-CT.

2.2 Materials and Methods

2.2.1 Specimen Preparation

Thirty fresh-frozen hind limbs were obtained from mature male Wistar rats exhibiting no skeletal pathology. All protocols were approved by the Institutional Animal Care and Use Committee at the University of Notre Dame. Femora were excised from right and left hind limbs, cleaned of all soft tissue, and randomly divided into a non-loaded control group and two loaded groups (n=10/group). Two specimens were removed from the study due to experimental error in the measurement of the secant modulus degradation and $BaSO_4$ staining, but both were replaced by an additional hind limb. Specimens were stored at –20°C in airtight containers containing an equal parts mixture of phosphate buffered saline (PBS) and ethanol during interim periods.

2.2.2 Fatigue Loading

Whole rat femora were thawed and rehydrated at ambient temperature for 24 h prior to mechanical loading. Femora were loaded in cyclic three-point bending at 2 Hz under load control in a PBS bath at ambient temperature using an electromagnetic test instrument (Bose ElectroForce 3300, Bose Corp., Eden Prairie, MN), until achieving a 5 or 10% reduction in the secant modulus. The loading fixture employed cylindrical, 4 mm diameter, lower roller supports at a fixed span of 14.5 mm (Figure 2.1). The upper load support had a major and minor diameter of 9 mm and 4 mm, respectively, with a concave surface (R=2.5 mm) designed to approximate the curvature of the cranial diaphyseal surface (Figure 2.1). Specimens were preconditioned with a 27 N static compressive load for 5 min, followed by cyclic three-point bending with a sinusoidal waveform at 2 Hz between a minimum and maximum load of 18 N and 36 N, respectively. The secant

modulus measured from the final hysteresis loop during cyclic preconditioning was used to calculate the maximum fatigue load normalized to an initial maximum strain of 8,000 ± 825 microstrain. Initial flexural strains were approximated as $\varepsilon = 6d\delta/L^2$ (Turner and Burr, 1993; Moreno *et al.*, 2006), where d is the specimen diameter, δ is the vertical deflection at the midspan, and L is the support span. The secant modulus degradation during fatigue loading was calculated as the percent reduction in instantaneous secant modulus at a given number of loading cycles relative to the initial secant modulus. The initial secant modulus was defined as the maximum secant modulus measured in the first 1000 cycles. The total number of loading cycles was recorded upon reaching the predetermined secant modulus degradation for each specimen.

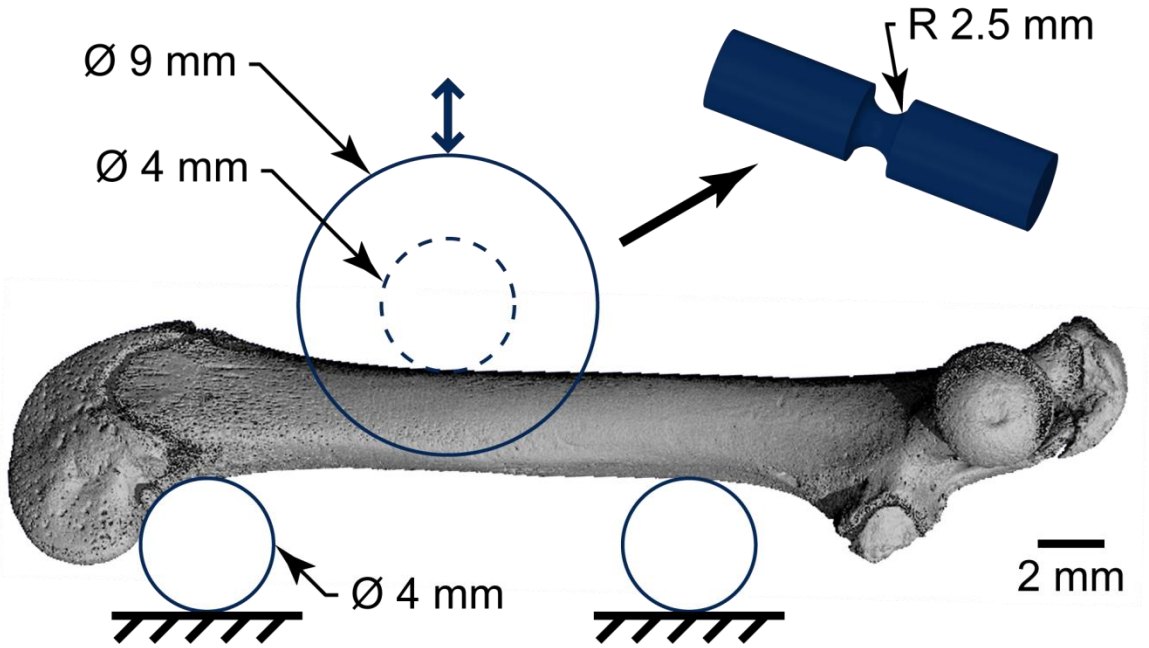

Figure 2.1: Schematic diagram showing a segmented micro-CT reconstruction of a whole rat femur loaded in cyclic three-point bending with cylindrical lower load supports on the relatively flat caudal surface and a concave upper load support on the cranial surface of the diaphysis.

2.2.3 Contrast-Enhanced Micro-Computed Tomography

Femora from both the non-loaded control and loaded groups were stained by $BaSO_4$ precipitation (Landrigan *et al.*, 2011). Specimens were soaked in a solution of equal parts acetone, PBS, and 0.5 M $BaCl_2$ (certified ACS crystal, Fisher Scientific, Fair Lawn, NJ) in DI water for 3 d, followed by a solution of equal parts acetone, PBS, and 0.5 M Na_2SO_4 (anhydrous powder, Fisher Scientific, Fair Lawn, NJ) in DI water for 3 d, both under vacuum (~50 mm Hg). Specimens were rinsed with DI water after each step to minimize particles or ions on specimen surfaces. The staining mechanism was a precipitation reaction where $BaCl_2(aq) + Na_2SO_4(aq) \rightarrow BaSO_4(s) + 2NaCl(aq)$. Barium and sulfate ions diffused and concentrated in void space—e.g., microcracks, damaged tissue, and vasculature—which provided an abundance of heterogeneous nucleation sites for precipitation on tissue surfaces (Leng *et al.*, 2008).

An 8.5 mm segment of the femoral diaphysis, centered about the midspan from three-point bending, was imaged using micro-CT (μCT-80, Scanco Medical AG, Brüttisellen, Switzerland) at 10 μm resolution, 70 kVp voltage, 114 μA current, and 400 ms integration time with slices oriented transverse to the diaphysis. Selected specimens were also imaged by micro-CT after fatigue loading but prior to staining to verify that microdamage was not able to be detected in the absence of the contrast agent. All micro-CT analyses were performed on the entire volume of the 8.5 mm segment scanned for each femur using the manufacturer's software (IPL v6.0, Scanco Medical). Grayscale images were smoothed by a Gaussian filter with sigma=1.5 and support=3. The total volume (TV) of cortical bone, inclusive of tissue porosity and exclusive of medullary volume, was measured after contouring the endosteal and periosteal surfaces (Figure 2.2). The ratio of the $BaSO_4$ stain volume (SV) to TV (SV/TV) was adopted as a

measure of damage. High intensity voxels representative of SV were segmented at a constant global threshold of 730, corresponding to a mean linear attenuation coefficient of 5.84 cm^{-1} or ~3340 mg hydroxyapatite per cubic centimeter (mg HA/cm^3) (Deuerling *et al.*, 2010). This threshold was well above the tissue mineral density of rat cortical bone, which was measured in this study to be ~1180 mg HA/cm^3 using micro-CT.

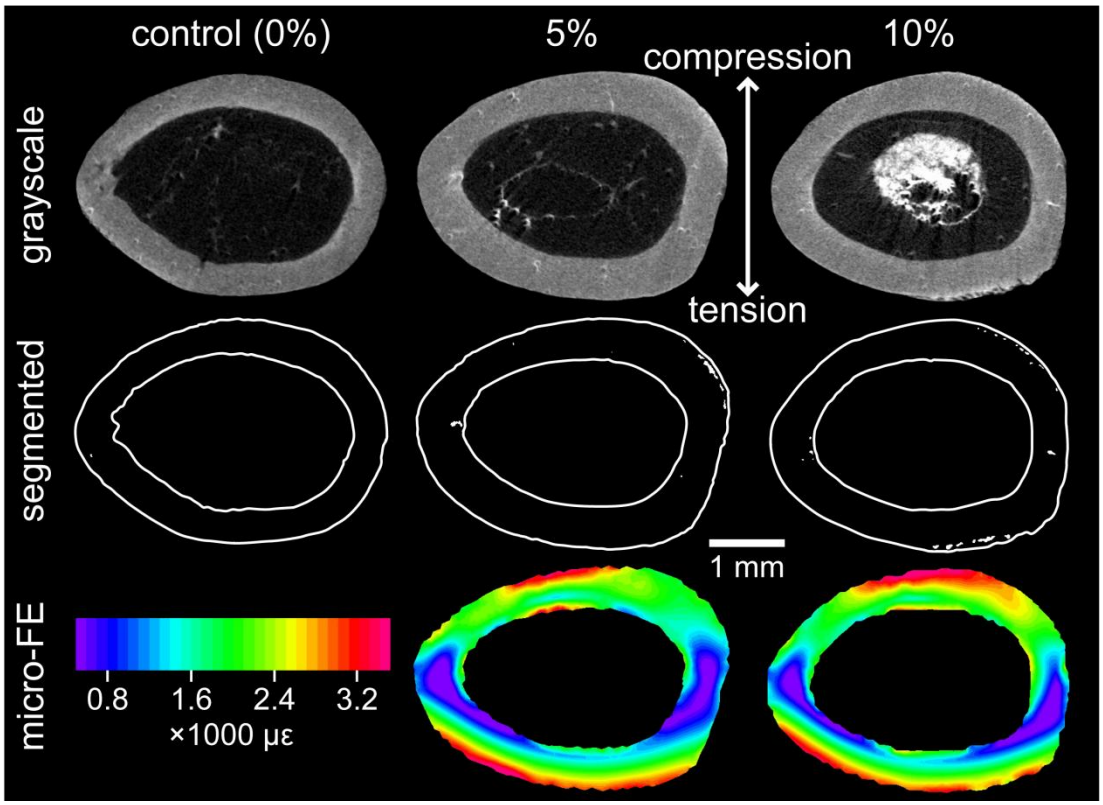

Figure 2.2: Grayscale and corresponding segmented micro-CT images for transverse cross-sections of a non-loaded control specimen and femora loaded in cyclic three-point bending to a 5 and 10% reduction in secant modulus, showing regions labeled by $BaSO_4$ (bright voxels). Note that the images shown correspond to the midspan of the median specimen (SV/TV) in each group. Specimen-specific finite element model predictions of the first principal strain are shown for static three-point bending to the maximum applied load.

2.2.4 Scanning Electron Microscopy

Specimens exhibiting the median SV/TV for each group were also imaged using scanning electron microscopy (SEM). Specimens were dehydrated in a graded series of alcohol solutions, embedded in poly(methyl methacrylate), sectioned sagittally with a diamond wire saw, polished with a series of diamond compounds to a 9 μm finish, washed with ethanol, and coated with iridium by sputter deposition. Specimens were imaged by SEM using backscattered electron imaging (BEI) at an accelerating voltage of 20 kV and a working distance of ~6 mm (Evo 50, LEO Electron Microscopy Ltd., Cambridge, UK). Note that image contrast from backscattered electrons is primarily due to compositional differences in atomic number, with an increasing atomic number resulting in increased intensity. The elemental composition of the stain was verified by electron probe microanalysis (EPMA) using energy dispersive spectroscopy (EDS) (INCA x-sight model 7636, Oxford Instruments America, Concord, MA).

2.2.5 Finite Element Model

Finite element models of specimens exhibiting the median SV/TV were used to examine strain distributions within transverse cross-sections of the femur. Micro-CT images were downsampled to 80 μm resolution by cubic interpolation and converted to tetrahedral meshes based on a constant threshold of 7,000 (Visualization Tool Kit, Kitware, Clifton Park, NY). Following Laplacian smoothing, the mesh was translated to a general-purpose finite element code (ADINA 8.6, Watertown, MA). Loads and boundary conditions were applied to simulate static three-point bending. In order to avoid stress concentrations at contact points, a uniformly distributed force was applied over a 4 mm length of the cranial diaphyseal surface at the location of the upper load

support. Uniform, isotropic elastic properties were assigned, with Young's modulus of 6.3 GPa, and Poisson's ratio of 0.3. The resulting displacement was approximately equal to the experimentally measured value in both cases. A second model using 60 μm resolution images was created for one sample to ensure sufficient mesh refinement.

2.2.6 Statistical Methods

All experimental groups exhibited non-normal distributions for SV/TV and the total number of loading cycles. Therefore, SV/TV and the number of loading cycles were separately compared between groups using Kruskal–Wallis non-parametric, one-way analysis of variance (ANOVA). *Post hoc* comparisons were performed using Mann–Whitney *U*-tests with a Bonferroni correction for multiple comparisons (JMP 8.0.2, SAS Institute Inc., Cary, NC). SV/TV was correlated with the number of loading cycles using linear least squares regression. The level of significance for all tests was $p < 0.05$.

2.3 Results

Microdamage was detected and observed to vary spatially in all femora loaded in cyclic three-point bending using contrast-enhanced micro-CT. Microdamage was labeled by concentrated regions of $BaSO_4$ stain, which appeared as bright voxels in grayscale micro-CT images, and was quantified in segmented images (Figure 2.2). Spatial variation in the accumulation of microdamage was observed in segmented, 3-D micro-CT reconstructions (Figure 2.3). At least one distinct region of microdamage, as indicated by the segmented SV, was visible in 85% of loaded specimens, whereas control specimens exhibited a lower segmented SV (Figure 2.3). Locations of segmented microdamage were consistently observed near cranial and caudal periosteal surfaces at the midspan, as

expected, but also included unanticipated observations near medial and lateral endosteal surfaces at the mid-coronal plane, especially moving away from the midspan (Figure 2.2 and Figure 2.3). A specimen-specific finite element model predicted elevated tensile principal strains localized in regions of tissue corresponding to locations of segmented microdamage (Figure 2.2).

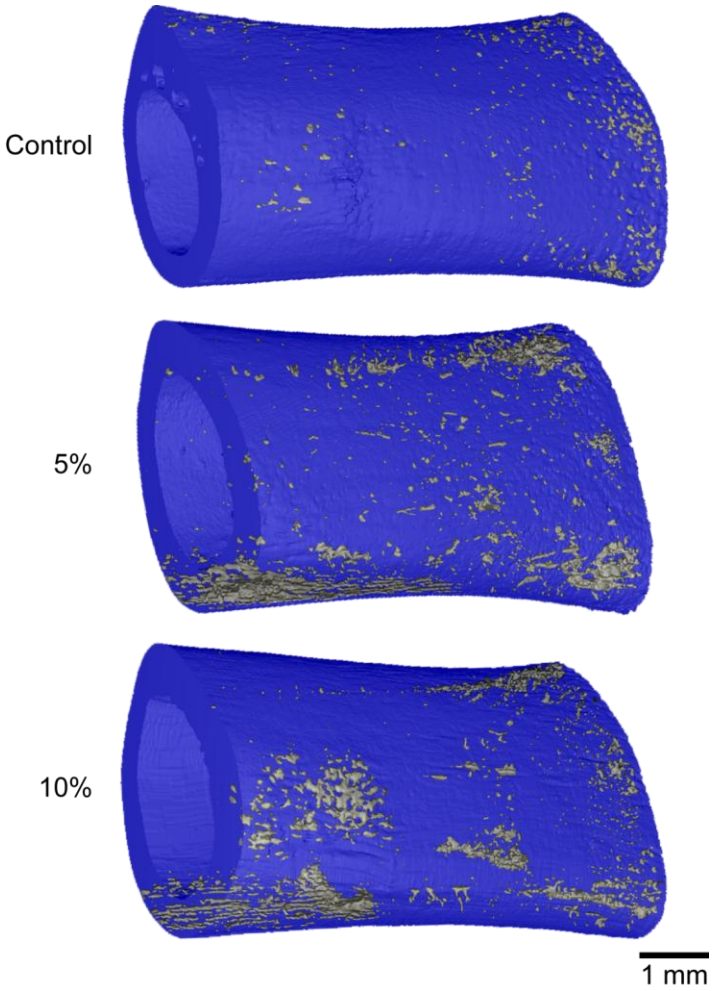

Figure 2.3: Segmented, 3-D micro-CT reconstructions of a non-loaded control specimen and specimens loaded to 5 and 10% degradation in secant modulus showing distinct regions of microdamage labeled by $BaSO_4$. Specimens are oriented to show the caudal surface under tension between the lower supports with lateral and medial surfaces above and below, respectively. Note that the specimens shown are the median specimen (SV/TV) from their respective experimental group.

Bright voxels detected by micro-CT were confirmed by backscattered electron imaging to be microcracks and/or diffuse damage labeled with $BaSO_4$ (Figure 2.4). EDS confirmed elevated levels of barium in labeled, damaged tissue relative to undamaged tissue. Histological observation of multiple sagittal sections from the median specimen (SV/TV) in both loaded groups revealed that microcracks located near the tensile (caudal) cortex were predominantly transversely oriented, while microcracks located near the compressive (cranial) cortex were predominantly oriented longitudinally (Figure 2.4).

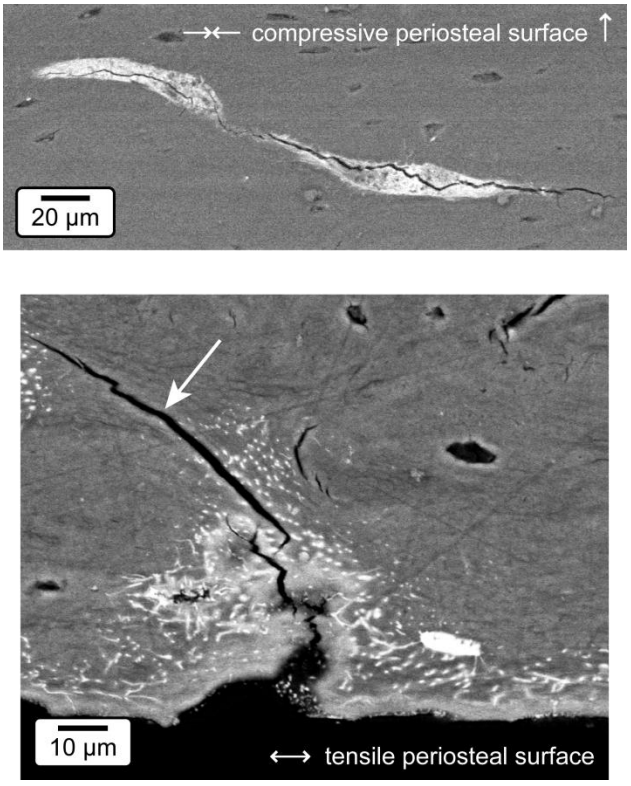

Figure 2.4: Backscattered scanning electron micrographs of sagittal sections of femora showing (a) a longitudinal (coronal) microcrack located near the compressive (cranial) periosteal surface and (b) a transverse microcrack (arrow) located on the tensile (caudal) periosteal surface. Note that the images correspond to the median (SV/TV) specimen loaded to a (a) 5 and (b) 10% reduction in secant modulus. The labeling of microcracks by $BaSO_4$ is evident by the brightness associated with atomic number contrast in backscattered electron imaging. Double arrows indicate the direction of normal bending stresses.

The amount of microdamage measured by SV/TV increased from the non-loaded control group to the loaded groups ($p < 0.05$, Kruskal-Wallis). The mean ratio of $BaSO_4$ stain volume to the total bone volume (SV/TV) was significantly greater for either loaded group compared to the control group ($p < 0.05$, Mann-Whitney *U*-test), but the difference between loaded groups was not statistically significant (Figure 2.5). The mean (± standard deviation) total number of loading cycles for groups loaded to a 5 and 10% reduction in secant modulus was 122,000 (74,000) and 81,000 (55,000), respectively, and the difference was not statistically significant ($p = 0.52$, Mann-Whitney *U*-test). SV/TV exhibited a weak positive correlation with the number of loading cycles for loaded specimens ($p = 0.08$, $R^2 = 0.16$).

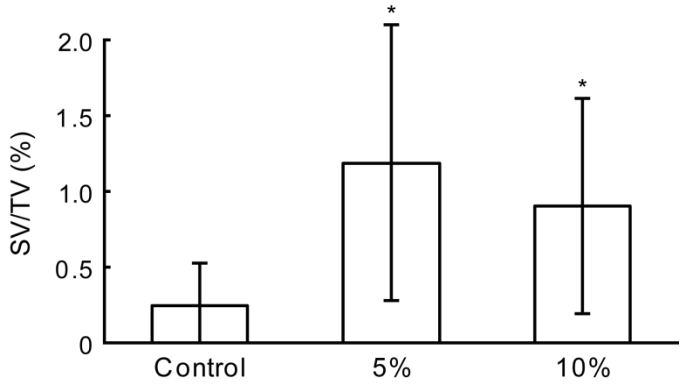

Figure 2.5: The ratio of $BaSO_4$ stain volume to total volume (SV/TV) measured in segmented micro-CT images was increased for loaded groups compared to the non-loaded control group. Error bars show one standard deviation. * $p < 0.05$, Mann-Whitney *U*-test versus control.

2.4 Discussion

Microdamage resulting from cyclic three-point bending of rat femora *in vitro* was detected and observed to accumulate at specific spatial locations within the cortex using contrast-enhanced micro-CT with a precipitated $BaSO_4$ stain. Previous studies employed similar staining and imaging techniques to investigate microdamage within machined cortical and trabecular bone specimens (Wang *et al.*, 2007; Leng *et al.*, 2008; Landrigan *et al.*, 2011). This study demonstrated the ability to detect microdamage in whole rat femora by adopting previously established methods. As such, this study constitutes the first nondestructive and 3-D assessment of microdamage in whole bones using contrast-enhanced micro-CT.

Whole bones pose greater challenges and opportunities for nondestructive detection of microdamage compared to geometric, machined specimens. For example, the bone morphology can lead to non-uniform variation in the tissue strain distribution (Figure 2.2). Therefore, whole bone morphology can influence tissue mechanical behavior in ways not anticipated by Euler-Bernoulli beam theory, e.g., which assumes a uniform cross-section and homogeneous tissue properties (van Lenthe *et al.*, 2008). Locations of segmented microdamage and elevated tensile principal strains were observed near cranial and caudal periosteal surfaces at the midspan, as expected (Figure 2.2 and Figure 2.3). However, locations of segmented microdamage also consistently included unanticipated observations near medial and lateral endosteal surfaces at the mid-coronal plane in 85% of loaded femora (Figure 2.2 and Figure 2.3). Interestingly, the finite element model also predicted elevated tensile principal strains in these locations with increasing prominence moving away from the upper load support

(midspan). A detailed investigation into the spatial correlation between segmented microdamage and finite element model predictions was subsequently performed (Gargac *et al.*, 2013).

The bright voxels observed in micro-CT images were verified by backscattered electron imaging and EDS to be due to the presence of $BaSO_4$ stain (Figure 2.4), similar to previous studies (Wang *et al.*, 2007; Leng *et al.*, 2008; Landrigan *et al.*, 2011). Note that backscattered electron imaging is destructive and was performed only to verify staining and image individual microcracks. Specimens were sectioned after nondestructive characterization using micro-CT. Individual microcracks located near the tensile (caudal) cortex were predominantly transversely oriented, while microcracks located near the compressive (cranial) cortex were predominantly oriented longitudinally (Figure 2.4). These crack orientations, combined with the direction of tensile principal strains predicted by the finite element model, suggest mode I crack opening in either region of the cortex. Microcracks were also observed in backscattered electron imaging to be 100-500 μm in length and approximately 1 μm thick, similar to previous studies (Frost, 1960; Schaffler *et al.*, 1994; O'Brien *et al.*, 2000; Mohsin *et al.*, 2006a). A limitation of contrast-enhanced micro-CT using current, commercially available instruments with a resolution of 10 μm is that individual microcracks are not typically able to be resolved, though larger fatigue cracks have been resolved when the stain penetrated tissue adjacent to the crack by at least one voxel length (Landrigan *et al.*, 2010; Landrigan *et al.*, 2011).

Variability in SV/TV (Figure 2.5) was attributed to a combination of non-specific staining of free surfaces and porosity, especially near endosteal surfaces, and variability

in whole bone morphology. The threshold utilized to segment SV was selected to minimize variability in SV/TV, as measured by the coefficient of variation across all experimental groups. Lower threshold values increased differences between the group means but also increased variability for SV/TV (cf., Figure 2.5). Interestingly, there was relatively little non-specific staining observed on periosteal surfaces in this study, most likely due to the periosteum. This observation contrasted previous studies where machined specimens were prone to non-specific staining on exterior surfaces (Leng *et al.*, 2008; Landrigan *et al.*, 2011). Finite element model predictions confirmed non-uniform spatial variation of strains within cross-sections (Figure 2.2) and along the length of the diaphysis. As described above, the strain distribution varied between specimens and maxima were not always located where one might expect *a priori* based upon Euler-Bernoulli beam theory. This suggests that intra- and inter-specimen variability in whole bone morphology may have contributed significantly to variability in microdamage accumulation.

The lack of an increase in SV/TV between specimens loaded to a 5 and 10% degradation in secant modulus has more than one possible interpretation. The staining methods were adopted from previous studies on machined specimens (Wang *et al.*, 2007; Leng *et al.*, 2008; Landrigan *et al.*, 2011) and were verified in a pilot study investigating stain penetration into whole rat femora using multiple levels of concentration and time. Nonetheless, as the technique has begun to be applied in multiple studies, we are learning that the optimal stain concentration and time appears to vary with the specimen size and tissue type, and may require further refinement. In particular, SEM observations suggested some specimens from this study may have been over-stained relative to

specimens from our previous studies. On the other hand, the apparent microcrack density may not have increased with continued reduction in the secant modulus. Histological measurements of microcrack density within cyclically loaded rat ulnae (Danova *et al.*, 2003) and canine femora (Burr *et al.*, 1998) were similarly able to differentiate control and loaded specimens, but unable to differentiate between specimens loaded to increasing levels of stiffness degradation. Moreover, contrast-enhanced micro-CT was previously able to detect damage accumulation between specimens loaded to two levels of secant modulus degradation in machined cortical bone specimens (Landrigan *et al.*, 2011).

Another possible reason for the lack of an increase in SV/TV between loaded groups lies in the use of cyclic three-point bending. Three-point bending subjects only a small volume of tissue near the midspan and periosteal surfaces to the maximum stress, which may have resulted in damage accumulation within a small localized region of tissue that appeared as the same SV in micro-CT. Other limitations associated with cyclic bending tests are well-known (Landrigan and Roeder, 2009); however, the complex morphology of whole rat femora necessitated a simple, reproducible test setup which was afforded by three-point bending. During preliminary testing, the original upper load support—a 4 mm diameter cylinder, identical to the lower supports—was observed to indent the specimen surface; therefore, a new upper load support was designed to more closely approximate the curvature of the diaphysis and minimize contact stresses (Figure 2.1). The modified upper load support alleviated the problem of indention, but was unable to perfectly match the variable curvature of every femur leading to variable contact which may have changed with an increased number of loading cycles. Note that the lower supports did not cause indention and were located outside the

region of interest imaged by micro-CT. Finally, the use of a three-point bending support span of sufficient length was prevented by the length of rat femora (Turner and Burr, 1993) and resulted in elevated shear stresses near the midspan. This was the most likely cause for the elevated tensile principal strains and segmented microdamage observed in the medial and lateral anatomic quadrants near the mid-coronal plane, but requires further investigation on the entire cohort of specimens.

2.5 Conclusions

Fatigue microdamage in whole rat femora loaded in cyclic three-point bending *in vitro* was detected and observed to accumulate at specific spatial locations within the cortex using contrast-enhanced micro-CT. The amount of microdamage measured by micro-CT was significantly greater for groups loaded to a 5 or 10% reduction in secant modulus compared to the control group, but the difference between loaded groups was not statistically significant. At least one distinct region of microdamage, as indicated by the segmented SV, was visible after segmentation in 85% of loaded specimens. A specimen-specific finite element model confirmed elevated tensile principal strains in regions of tissue corresponding to the accumulated microdamage. These regions were not always located where one might expect *a priori* based upon Euler-Bernoulli beam theory, demonstrating the utility of contrast-enhanced micro-CT for nondestructive, 3-D detection of fatigue microdamage in whole bones *in vitro*.

CHAPTER 3:

FATIGUE MICROCRACKS THAT INITIATE FRACTURE ARE LOCATED NEAR ELEVATED INTRACORTICAL POROSITY BUT NOT ELEVATED MINERALIZATION

3.1 Introduction

Microcracks in cortical bone are typically observed to readily initiate upon repetitive mechanical loading within more highly mineralized interstitial tissue (Schaffler *et al.*, 1995; Norman *et al.*, 2008), but arrest at microstructural barriers such as osteons (O'Brien *et al.*, 2003; Mohsin *et al.*, 2006b; Kennedy *et al.*, 2008). However, the microarchitectural conditions which allow arrested microcracks to break free of osteons upon continued fatigue loading and/or cause catastrophic fracture upon a single loading event (e.g., fall) are not well understood. The well-established observation that *in vivo* microcracks are predominantly located within more highly mineralized interstitial tissue, and subsequent attention to these microcracks, may be unintentionally misleading with respect to understanding of fracture mechanisms and fracture risk. Postmortem investigations of these microcracks are inherently limited to cracks that did not lead to a fracture. However, fracture mechanics teaches that only one critical flaw, or stress concentration, is necessary for fracture. In other words, identification of the one microcrack that ultimately leads to fracture may be obscured by attention to hundreds of microcracks that do not lead to fracture.

Intracortical porosity is well-known to compromise the mechanical properties of cortical bone (Currey, 1988; Schaffler and Burr, 1988; Yeni *et al.*, 1997; Ural and Vashishth, 2007; Kennedy *et al.*, 2009), as would be expected with any engineering material. However, little attention has been given to the interaction of intracortical porosity and fatigue microdamage. The hypothesis that intracortical porosity provides stress concentrations for primary and/or secondary crack initiation ahead of a propagating microcrack has been largely overlooked with the possible exception of a couple studies (Fleck and Eifler, 2003; Soicher *et al.*, 2011), perhaps because *in vivo* microcrack density is only weakly correlated with intracortical porosity (Norman *et al.*, 2008). However, as discussed above, the *in vivo* microcrack density is inherently biased and dominated by microcracks that do not lead to fracture.

We hypothesized that fatigue microcracks which initiate fracture are located spatially adjacent to elevated intracortical porosity but not elevated mineralization. Therefore, the objective of this study was to investigate the spatial correlation between intracortical porosity, elevated mineralization, and fatigue microdamage by combining, for the first time, sequential, nondestructive, three-dimensional (3-D) micro-computed tomography (micro-CT) measurements of each in cortical bone specimens subjected to cyclic loading followed by an overload to fracture *in vitro*. Fatigue microdamage was imaged using contrast-enhanced micro-CT with a barium sulfate stain as previously described and validated (Landrigan *et al.*, 2011; Turnbull *et al.*, 2011).

3.2 Materials and Methods

3.2.1 Specimen Preparation

Sixteen femoral cortical bone specimens were prepared from the proximal and mid-diaphysis (Figure 3.1) of an 85 year-old male tissue donor presenting no medical history of skeletal pathology or trauma. All tissues were obtained with donor consent (National Disease Research Interchange, Philadelphia, PA) and all protocols were approved by the Notre Dame Human Subjects Institutional Review Board. Two 4.5 cm segments of the diaphysis, centered at 50 and 75% of the total femur length, were removed while frozen. Paired specimen blanks were removed from each section using a low-speed diamond wafer saw (Isomet, Buehler, Lake Bluff, IL). Each specimen blank was kept hydrated with deionized (DI) water while machining into cylindrical "dog bone" specimens with a 10 mm gauge length and 3 mm gauge diameter (Figure 3.1) using a computer numerical controlled mill and lathe. Paired specimens were randomly divided into a non-loaded control group and a cyclically loaded group according to the study design (Table 3.1). Specimens were kept hydrated in phosphate buffered saline (PBS) at all times and stored at −20°C wrapped in gauze in airtight containers during interim periods. One specimen pair was removed from the study after one specimen fractured during handling.

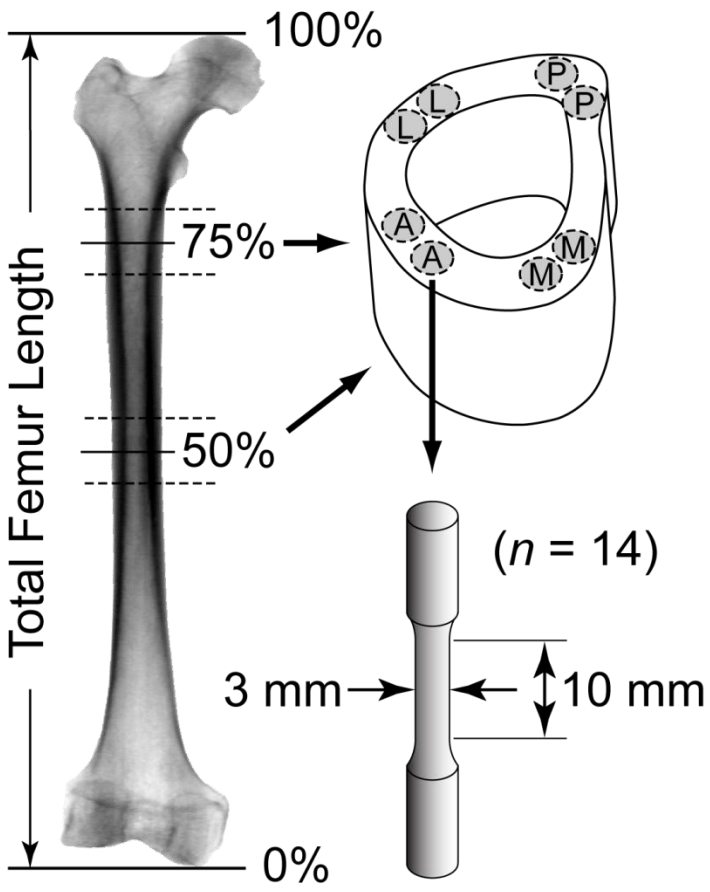

Figure 3.1: Schematic diagram showing a human femur and the locations from which paired specimens were machined. Note that in each anatomic quadrant (A=anterior, P=posterior, M=medial, and L=lateral) a pair of specimens was systematically assigned to the non-loaded control and fatigue loaded group.

TABLE 3.1

GROUP ASSIGNMENTS AND STUDY DESIGN

Group	**Step 1**		**Step 2**			**Step 3**		
A	→ micro-CT	→	fatigue	→ stain	→ micro-CT	→	load to failure	→ micro-CT
B	→ micro-CT	→	no loading	→ stain	→ micro-CT	→	load to failure	→ micro-CT

3.2.2 Micro-CT Imaging (Step 1)

The entire gauge section of each specimen was imaged by micro-CT (μCT-80, Scanco Medical AG, Brüttisellen, Switzerland) at each of three sequential steps: (1) as-prepared, (2) after cyclic loading and labeling fatigue microdamage, and (3) after fracture due to an overload. Micro-CT images were acquired at 10 μm resolution, 70 kVp voltage, and 114 μA current with 1000 projections at a 600 ms integration time with slices oriented perpendicular to the longitudinal specimen axis. A custom fixture ensured consistent specimen positioning during the multiple micro-CT scans required for each specimen and expedited subsequent image registration. Noise in grayscale images of as-prepared specimens was reduced using a Gaussian filter (sigma = 0.8, support = 1). The bone volume (BV) was segmented (Figure 3.2) at a constant global threshold of 270 to reveal the pore volume (PV). This threshold value corresponded to ~840 mg hydroxyapatite per cubic centimeter (mg HA/cm^3) using a custom calibration phantom (Deuerling *et al.*, 2010). The BV was further segmented (Figure 3.2) into a low mineral level volume (LMV) and a high mineral level volume (HMV) corresponding to the lowest 20% and highest 20%, respectively, of voxels within the BV averaged for all specimens. Gaussian filter parameters (sigma = 1.5, support = 3) and the bone volume threshold (290, 2.32 cm^{-1}, or ~920 mg HA/cm^3) were altered for micro-CT measurements at steps (2) and (3) to account for the overall shift in image intensity resulting from barium sulfate stain attenuation and thus segment the same volume of intracortical porosity as in step (1) (Landrigan *et al.*, 2011). High intensity voxels representative of damaged tissue volume (DV) were segmented at a constant global threshold of 490, corresponding to a mean linear attenuation coefficient of 3.92 cm^{-1} or ~1890 mg HA/cm^3,

which was well above the tissue mineral density of human cortical bone (Deuerling *et al.*, 2010).

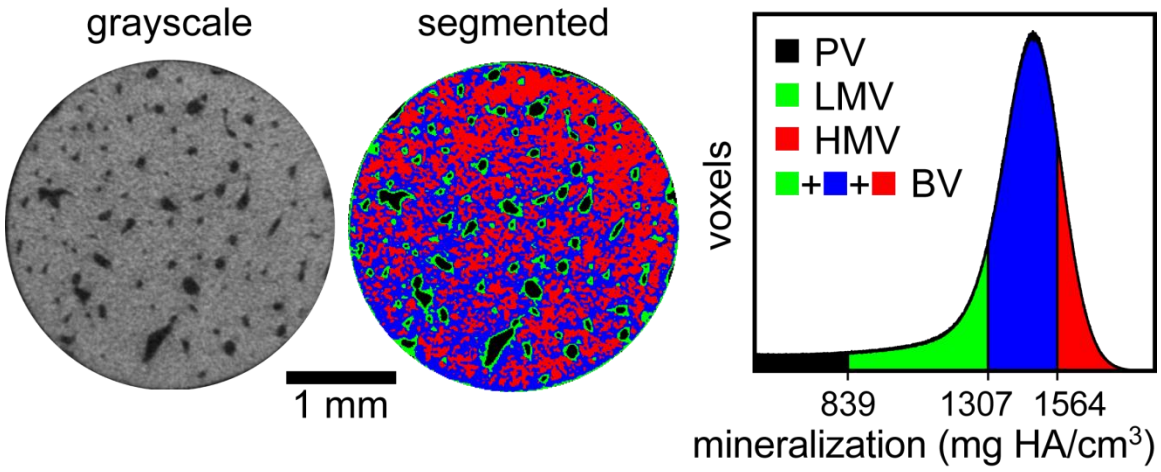

Figure 3.2: Grayscale and corresponding segmented micro-CT image and histogram for a transverse cross-section of a loaded group specimen prior to damage showing the segmentation and distribution of intracortical porosity (PV), and low (LMV) and high (HMV) mineral level volumes.

3.2.3 Fatigue Loading and Microdamage Labeling (Step 2)

Paired specimens were either not loaded (control) or subjected to cyclic uniaxial compression at 2 Hz with a sinusoidal waveform in an ambient PBS bath under load control using an electromagnetic test instrument (Bose ElectroForce 3300, Bose Corp., Eden Prairie, MN). Loaded specimens were first preconditioned with a maximum compressive stress of 40 MPa for 240 cycles. Following preconditioning, specimens were subjected to a maximum cyclic compressive stress of 75 MPa (R = 0.1) in the gauge section until achieving a 10% reduction in secant modulus. The secant modulus degradation during fatigue loading was calculated as the percent reduction in instantaneous secant modulus at a given number of loading cycles relative to the initial secant modulus. The initial secant modulus was defined as the average secant modulus

of the first 20 cycles during fatigue loading. The total number of loading cycles was recorded upon reaching the predetermined secant modulus degradation for each specimen.

All specimens were stained by barium sulfate ($BaSO_4$) precipitation to label preexisting microdamage and/or microdamage resulting from fatigue loading using methods previously described and validated (Landrigan *et al.*, 2011; Turnbull *et al.*, 2011). Specimens were imaged again by micro-CT, as described above. The ratio of damage volume to bone volume (DV/BV) was adopted as a measure of microdamage (Landrigan *et al.*, 2011; Turnbull *et al.*, 2011). The gauge section was segmented to reveal labeled microdamage (DV), which was overlaid on micro-CT images of the as-prepared specimens using image registration (Analyze 10.0, Mayo Foundation for Medical Education and Research) (Figure 3.3). Non-specific staining of tissue porosity and exterior specimen surfaces was minimized in a series of three steps. First, the segmented BV of each as-prepared specimen was applied as an inclusion mask to the corresponding segmented DV after registration such that the resulting image volume contained only stain within the bone matrix or BV, not stain within the PV. Second, a MATLAB script was written to eliminate clusters of DV at the specimen free surface which did not penetrate into the specimen interior. At least 25% of the voxels in each DV cluster were required to penetrate the specimen more than 100 μm (10 voxels) from the free surface in order to be included. Last, a 100 μm (10 voxels) peel was applied to the DV to remove non-specific $BaSO_4$ staining on the exterior specimen surface (Landrigan *et al.*, 2011).

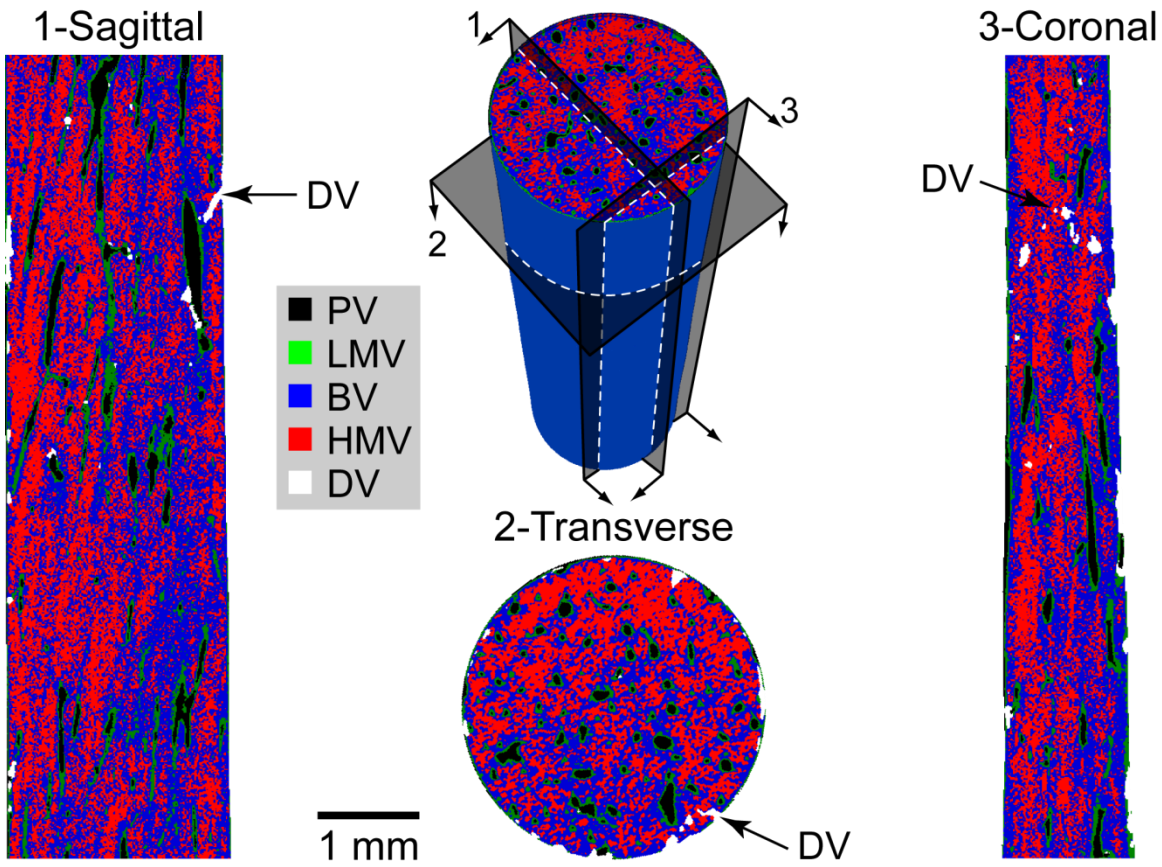

Figure 3.3: Segmented, orthogonal micro-CT cross-sections of a loaded group specimen after fatigue damage and $BaSO_4$ staining showing the stained DV (white, arrows) that was later confirmed to be the site of fracture initiation in close proximity to a large pore.

3.2.4 Tensile Overload (Step 3)

All specimens were hydrated in PBS for one hour prior to overload, loaded to failure in uniaxial tension at 25 mm/s, and imaged again by micro-CT as described above. Micro-CT images of fractured specimens were registered with micro-CT images of the as-prepared specimens to identify the fracture initiation site by the presence of DV on the fracture surface of loaded specimens (Figure 3.4). The elastic modulus (E), ultimate tensile strength (UTS), strain-to-failure (ε_f), and work of fracture (w_f) were calculated from measured force-displacement data and dimensions of the specimen gauge section

(Roeder, 2013). The ultimate tensile strength (UTS) was measured as the maximum stress. Strain-to-failure was calculated as the percent strain at fracture. The work of fracture was measured by the area under the load-displacement curve at fracture.

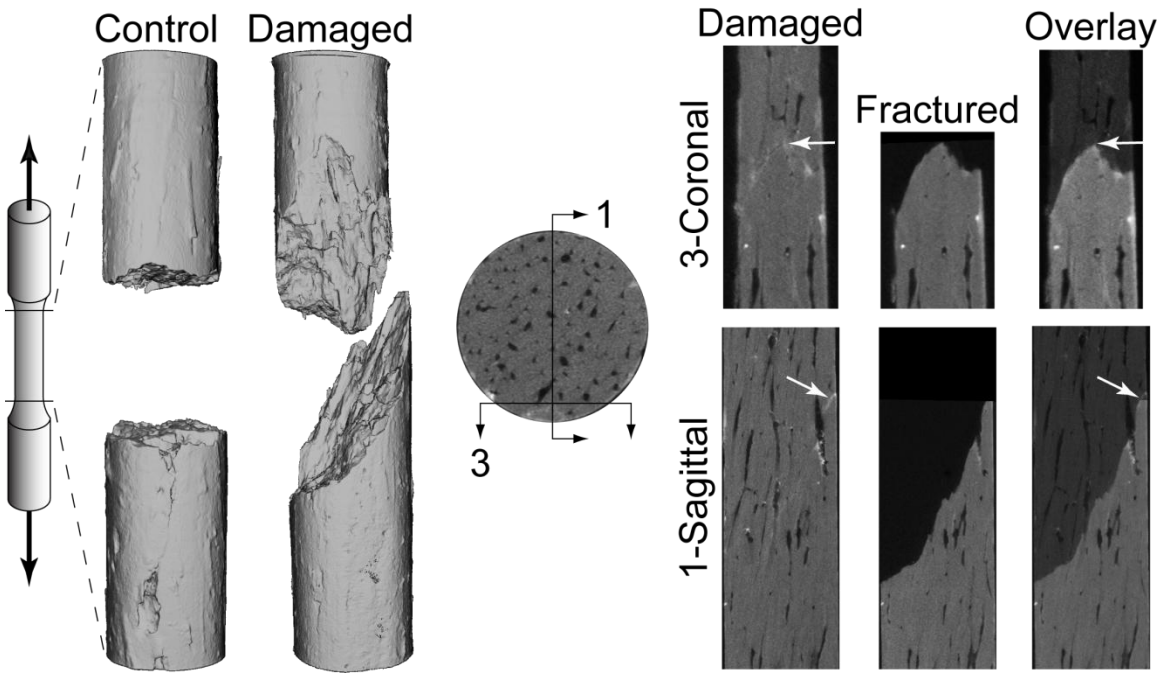

Figure 3.4: Segmented micro-CT reconstructions for representative control and loaded group specimen and corresponding orthogonal grayscale micro-CT images for the loaded group specimen. The fracture surfaces of loaded group specimens were tortuous and oblique, corresponding to the labeled fatigue microdamage (DV, bright voxels, arrows), whereas the fracture surfaces of control group specimens were transverse and relatively smooth.

3.2.5 Analytical and Statistical Methods

The normalized two-point correlation function, or probability density function (PDF), for encountering PV, HMV, or LMV as a function of the three-dimensional (3-D) radial distance from either the DV that initiated fracture, or all damage sites (DVs), was computed using a custom MATLAB script (Appendix A.1). Briefly, PDFs were calculated for each specimen by computing the radial distribution function (RDF)

(Torquato, 2002) and then normalizing to account for differences in the volume sampled at each radial distance, *r*, and the total volume of each feature of interest, such that PDF = 1 for random probability. In other words, the local volume fraction of the feature of interest (e.g., PV, HMV, or LMV) located at each radial distance from the voxel(s) of origin (DVs) was normalized by the overall volume fraction of the feature of interest (Appendix A.2). Multiple RDFs, one for each unique voxel of origin (DV), were computed and aggregated to form a two-point correlation function (Torquato, 2002) and then normalized to provide the specimen-specific PDF for each feature of interest. The PDFs for each feature of interest for multiple specimens were averaged and plotted for voxel(s) of origin corresponding to either the DV that initiated fracture or all damage sites (DVs). The PDF methods outlined above included 5% of DV voxels (evenly spaced, e.g., every twentieth voxel) in the gauge section based on the results of a sensitivity analysis conducted to determine the minimum sampling rate of DV voxels of origin. Computations were performed on 8 processors utilizing 12 GB of memory and required a maximum wall clock computation time of ~15 h per specimen to compute the PDF for all features of interest.

The mean value of the PDF was calculated for encountering PV, HMV, and LMV within the first 440 μm from either the DV that initiated fracture or all damage sites (DVs). Note that the distance of 440 μm corresponds to a threshold length for cracks to break free of microstructural barriers (Mohsin *et al.*, 2006b).

All experimental groups were limited in the number of samples and some variables exhibited non-normal distributions; therefore, non-parametric tests were utilized for all statistical analyses (JMP 10.0, SAS Institute, Cary, NC). DV/BV and mechanical

properties of fatigue loaded specimens were compared to those of non-loaded control specimens using Wilcoxon Signed Rank tests for matched pairs. Mean PDF values for PV, HMV, and LMV were compared to random probability (PDF = 1) using a Mann-Whitney *U*-test with a hypothesized mean of 1. Mean PDF values for the fracture initiation site versus all damage sites (DVs) were compared for each feature of interest (PV, HMV, and LMV) using Wilcoxon Signed Rank tests for matched pairs. DV/BV was correlated with the number of loading cycles using linear least squares regression. The level of significance for all tests was set at $p < 0.05$.

3.3 Results

Segmented, 3-D micro-CT reconstructions of as-prepared (Figure 3.2) and fatigue loaded (Figure 3.3) specimens revealed the spatial distribution of intracortical porosity (PV), low and high levels of mineralization (LMV and HMV, respectively), and damage (DV). The mean ± standard deviation intracortical porosity volume fraction for all specimens in this study was 19.2 ± 11.9%. HMV was observed to be heterogeneously distributed within the BV in between PV, presumably corresponding to interstitial tissue (Figure 3.2 and Figure 3.3). The mean PDF for HMV from PV voxels of origin was 0.75 which was significantly less than random probability ($p < 0.05$, Mann-Whitney). LMV appeared to be located in close spatial proximity to PV, as expected of tissue surrounding Haversian canals. However, the mean PDF for LMV within the first 440 μm from PV voxels of origin was 1.03 which was not statistically different from random probability ($p = 0.38$, Mann-Whitney), but was reduced as a consequence of the relatively large 440 μm distance compared to the scale of LMV surrounding PV. As a whole, fatigue

microdamage (DV) was observed to initiate stochastically within the entire gauge section (Figure 3.3). Larger regions of DV initiated near the specimen perimeter and/or in proximity to locally elevated intracortical porosity (PV).

Fatigue loaded specimens exhibited significantly increased microdamage accumulation (DV/BV) compared to non-loaded control specimens ($p < 0.05$, Wilcoxon Signed Rank) (Table 3.2) and DV/BV was not correlated with the number of fatigue loading cycles ($p > 0.25$). This microdamage accumulation was sufficient to significantly compromise the mechanical properties of fatigue loaded specimens compared to control specimens upon the tensile overload (Table 3.2). Fatigue loaded specimens exhibited an approximately 30% reduction in elastic modulus ($p < 0.05$, Wilcoxon Signed Rank), three-fold decrease in ultimate tensile stress ($p < 0.05$, Wilcoxon Signed Rank), two-fold decrease in strain-to-failure ($p < 0.05$, Wilcoxon Signed Rank), and six-fold decrease in work of fracture ($p < 0.05$, Wilcoxon Signed Rank), compared to non-loaded control specimens.

TABLE 3.2

FATIGUE CYCLES, MICRODAMAGE ACCUMULATION, AND TENSILE OVERLOAD MECHANICAL PROPERTIES FOR NON-LOADED CONTROL AND FATIGUE LOADED SPECIMENS SHOWING THE MEAN (± STANDARD DEVIATION)

			Tensile Overload Mechanical Properties			
Group	Fatigue Cycles	DV/BV (%)	E (GPa)	UTS (MPa)	ε_f (% strain)	w_f (mN-m)
Control	n/a	0.30 (0.17)	7 (0.7)	90 (26)	1.9 (0.6)	74 (37)
Fatigue	24,000 (39,000)	1.38 (1.06)*	5 (2.1)*	33 (17)*	0.9 (0.4)*	12 (9)*

* $p < 0.05$ vs. Control, Wilcoxon Signed Rank. n/a = not applicable.

The final fracture upon overload of all fatigue loaded specimens exhibited a tortuous oblique surface due to the presence of longitudinal microcracks (DV) previously initiated in cyclic compression, often noticeably adjacent to intracortical porosity (PV) (Figure 3.4). In contrast, control specimen fracture surfaces exhibited a relatively smooth transverse fracture plane (Figure 3.4). The DV that initiated fracture was able to be clearly identified by the presence of stained DV on the fracture surface of all 7 fatigue loaded specimens (Figure 3.4, arrows). In contrast, the fracture surface of all 7 non-loaded control specimens contained no stained DV.

PDFs averaged for all fatigue loaded specimens revealed a greater than random probability for PV located spatially adjacent to the DV that initiated fracture and a less than random probability for HMV located spatially adjacent to the DV that initiated fracture (Figure 3.5a). This difference was unique to the DV that initiated fracture (Figure 3.5a) as both PV and HMV exhibited near random probability of being located adjacent to all damage sites (DVs) (Figure 3.5b).

The mean PDF for PV and HMV within 440 μm of the fracture initiation site was significantly greater than random probability ($p < 0.05$, Mann-Whitney) and less than random probability ($p < 0.05$, Mann-Whitney), respectively (Figure 3.6). In contrast, the mean PDF for either PV ($p = 0.08$, Mann-Whitney) or HMV ($p = 0.38$, Mann-Whitney) within 440 μm of all damage sites (DVs) was not statistically different from random probability. The mean PDF for PV near the fracture initiation site was significantly greater than that for all damage sites (DVs) ($p < 0.05$, Wilcoxon Signed Rank). In contrast, the mean PDF for HMV near the fracture initiation site was significantly less than that for all damage sites (DVs) ($p < 0.05$, Wilcoxon Signed Rank). The mean PDF for LMV located spatially adjacent to either the DV that initiated fracture or all damage sites was not statistically different from random probability ($p = 0.47$ and 0.81, respectively, Mann-Whitney).

In control specimens, the mean PDF for LMV within 440 μm of all damage sites was not significantly different from random probability ($p = 0.81$, Mann-Whitney), while the mean PDF for both PV and HMV was significantly greater than random probability ($p < 0.05$, Mann-Whitney).

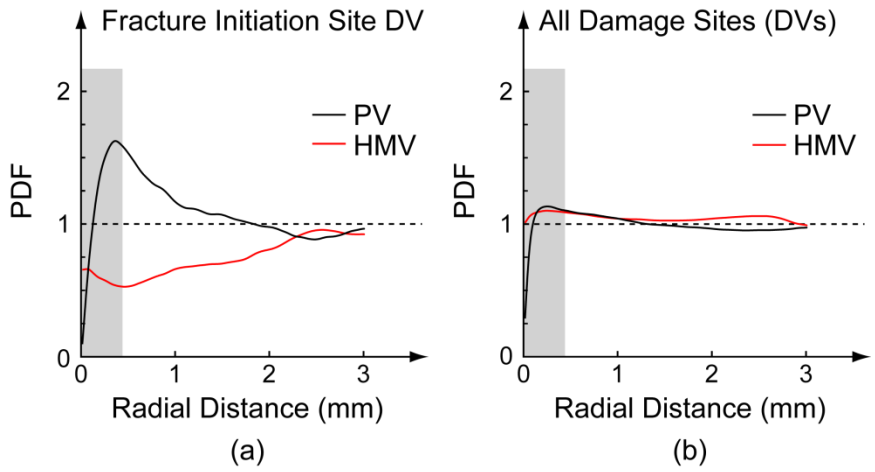

Figure 3.5: The normalized two-point correlation function, or probability density function (PDF), for intracortical porosity (PV) and high mineral level volume (HMV) located near (a) the fracture initiation site or (b) all damage sites (DVs) and averaged for all fatigue loaded specimens. Note that PDF = 1 corresponds to random probability. Appendix A.3 shows inter-specimen variability in the measured PDFs.

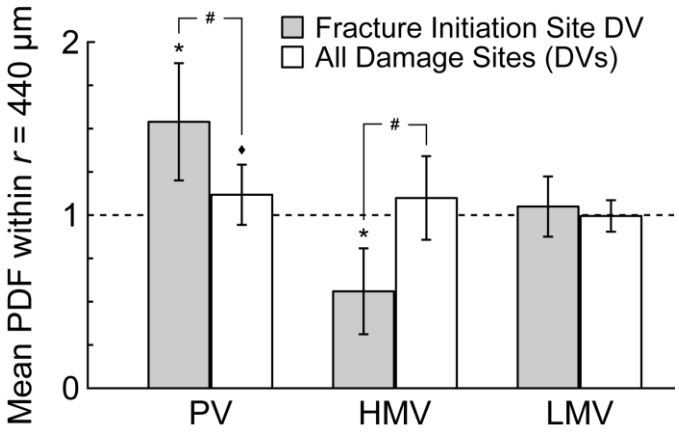

Figure 3.6: The mean value of the normalized two-point correlation function, or probability density function (PDF), for intracortical porosity (PV) and high mineral level volume (HMV) located within r = 440 µm from the fracture initiation site or all damage sites (DVs) of fatigue loaded specimens. Error bars show one standard deviation of the mean. Note that PDF = 1 corresponds to random probability. * $p < 0.05$ vs. 1, Mann-Whitney U-test. ♦ $p = 0.08$ vs. 1, Mann-Whitney U-test. # $p < 0.05$, Wilcoxon Signed Rank for matched pairs.

3.4 Discussion

Microdamage (DV) at the fracture initiation site was found to be spatially correlated with intracortical porosity (PV), but not highly mineralized tissue (HMV) (Figure 3.5a and Figure 3.6). This suggests that cortical bone fractures initiated at fatigue microcracks located near elevated intracortical porosity but not elevated mineralization. In contrast, there was no spatial correlation between both PV and HMV and all damage sites (DVs) (Figure 3.5b and Figure 3.6). This result demonstrates that fatigue microcracks readily and stochastically initiate and accumulate within the extracellular matrix (ECM) of cortical bone as has been previously suggested (Norman and Wang, 1997). Taken together, these results suggest that human cortical bone is largely tolerant of microdamage, which is generally compartmentalized within the interstitial tissue (Martin and Burr, 1982; Norman and Wang, 1997) and serves to dissipate strain energy (Reilly and Currey, 2000). However, a single microcrack of sufficient size located in spatial proximity to intracortical porosity can compromise fracture resistance. In fracture mechanics, a microcrack in close spatial proximity to a pore leads to a greater stress intensity factor resulting from a summation of the individual component stress intensity factors by the principle of superposition (Anderson, 2005) (e.g., $K_{I,\,total} = K_{I,\,microcrack} + K_{I,\,pore}$). Therefore, an increase in the fraction or size of intracortical pores (e.g., resulting from metabolic bone disease or transient remodeling to repair microdamage) leads to an increased probability of proximity between a pore and a stochastically generated microcrack. The prediction of fracture risk could thus be improved by clinical assessment of intracortical porosity, which may, in turn, influence pharmacological treatment strategies.

Recent advances in high-resolution peripheral quantitative computed-tomography (HR-pQCT) have enabled 3-D, non-invasive *in vivo* imaging of intracortical porosity at appendicular skeletal sites (MacNeil and Boyd, 2008; Burghardt *et al.*, 2010a; Liu *et al.*, 2010). Intracortical porosity in the distal radius and tibia was measured by HR-pQCT and correlated with age for both men and women, and micro-finite element analysis revealed a significantly greater biomechanical deficit due to intracortical porosity for postmenopausal women relative to premenopausal women (Burghardt *et al.*, 2010b). Therefore, new strategies for fracture risk assessment could be based on directly measured characteristics of intracortical porosity.

The net benefit of bisphosphonate treatment for osteoporosis has been a subject of debate in the literature (Seeman, 2009; Allen and Burr, 2011). The suppression of bone remodeling by bisphosphonates preserves cortical bone mass, or limits further increases in intracortical porosity, in order to maintain the mechanical integrity of cortical bone (Burghardt *et al.*, 2010c; Allen and Burr, 2011). On the other hand, long term suppression of bone remodeling by bisphosphonates may increase mineralization levels resulting in more brittle tissue and an increased risk of "atypical" fractures (Lenart *et al.*, 2008). The results of this study suggest that the net benefit of limiting increases in intracortical porosity should outweigh the net deficit due to increased mineralization since fracture initiation sites were spatially associated with intracortical porosity but not elevated mineralization. The methods of analysis in this study provide a means to decouple and quantitatively compare the net effects of pharmacological treatments on fracture susceptibility.

Interestingly, the spatial proximity of PV to the fracture initiation site consistently reached maximum probability at approximately 400 μm (390 ± 60 μm) (Figure 3.5a). This result adds further support to the concept of a critical length of microcracks, which was previously suggested to be 440 μm (Mohsin *et al.*, 2006b). Bone permits microcrack initiation but resists crack propagation (Reilly and Currey, 2000). However, there is a limit to the ability of any material to resist crack propagation which coincides with a critical crack length above which a crack possesses enough surface free energy to undergo unstable propagation to failure, in spite of microstructural barriers to crack growth (e.g., osteons and cement lines). Therefore, the mean PDF for PV and HMV within r = 440 μm of microdamage (DV) was computed for all loaded specimens.

The computational demand required to calculate the PDF for a single voxel of origin was only ~90 s on a standard laptop, but increased in proportion with the number of possible microdamage (DV) voxels of origin. For example, a typical fatigue loaded specimen containing ~1 million DV voxels required ~11 d to compute the PDF for all DVs. Therefore, measures were taken to improve the computational efficiency. First, since specimens were 3 mm in diameter the sample volume was restricted to a 3 mm radius from each individual voxel of origin, such that objects of interest located more than 3 mm away from each active voxel of origin were excluded from the analysis. Next, a pilot study assessed the feasibility of sampling a subset (100%, 50%, 5%, 0.1%, or 0.01%) of voxels in the DV. There was no qualitative difference in PDFs calculated by sampling every (100%), every other (50%), or every twentieth (5%) voxel in the DV and no difference observed in the mean value of the PDF at 440 μm (Wilcoxon Signed Rank). However, sampling less than 5% of the voxels in the DV altered the PDF and was

therefore concluded to be an insufficient sampling volume. Sampling every twentieth voxel in the DV (5%) required a maximum computation time of approximately 15 h per specimen to compute the PDF. A sensitivity analysis was conducted to determine the effect of adjusting the highly mineralized tissue (HMV) threshold to include fewer voxels (e.g., the highest 5% of voxels in the BV, compared to the highest 20% of voxels). Restricting the HMV voxels to include only the highest 5% within the BV increased the noise of the PDF corresponding to the reduced sampling rate, but did not have an effect on the mean value of the PDF for HMV at 440 μm (Wilcoxon Signed Rank). Therefore, this result provided confidence in the normalization techniques employed in the calculation of the PDF.

Several limitations of this study are worth noting. First, this study was limited to a small number of specimens from one donor, and the testing was performed *in vitro*. Second, fatigue loading to a 10% reduction in secant modulus produced relatively large microcracks. Moreover, the 30% reduction in modulus upon the tensile overload for loaded group specimens compared to non-loaded controls was a static measure of modulus, and should not be directly compared to the dynamic modulus loss of 10% reached during cyclic loading. Third, selection of the cluster(s) of damage (DV) that resulted in fracture required manual inspection of registered micro-CT images from loaded and fractured specimens to correctly identify the fracture initiation site. Last, a tensile overload was used to ensure preservation of an intact fracture surface since a compressive overload would damage the fracture surface and hinder any attempt to locate the site of fracture initiation. Nonetheless, the methods utilized in this study facilitated

important new insights into our understanding of cortical bone fracture mechanisms and are well-suited for use in future studies investigating fracture susceptibility.

3.5 Conclusions

The spatial correlation between intracortical porosity, mineralization levels, and fatigue microdamage was investigated by combining, for the first time, sequential, nondestructive, 3-D micro-CT measurements of each in cortical bone specimens subjected to cyclic loading followed by an overload to fracture. Fatigue loading to a 10% reduction in secant modulus induced significant microdamage accumulation which significantly compromised the mechanical properties of fatigue loaded specimens compared to paired non-loaded control specimens. These novel methods allowed identification of the fracture initiation site in specimens and the calculation of spatial correlation between microstructural features. Fatigue microcracks that initiated fracture upon overload were found to be spatially correlated with elevated intracortical porosity but not elevated mineralization. This difference was unique to the fatigue microcracks that initiated fracture as both intracortical porosity and highly mineralized tissue exhibited near random probability of being located adjacent to all damage sites (DVs). These results suggested that human cortical bone is largely tolerant of microdamage which is generally compartmentalized within interstitial tissue, but a single microcrack of sufficient size located in spatial proximity to intracortical porosity can compromise fracture resistance. The prediction of fracture risk could thus be improved by clinical assessment of intracortical porosity, which may, in turn, influence pharmacological treatment strategies.

CHAPTER 4:

SPATIAL CORRELATIONS OF INTRACORTICAL POROSITY, MINERALIZATION LEVELS, AND FATIGUE MICRODAMAGE IN HUMAN CORTICAL BONE SPECIMENS OF VARYING AGE AND FATIGUE LOADING MODE

4.1 Introduction

Chapter 3 introduced new methods for identification of the fracture initiation site in cortical bone specimens and measuring the spatial correlation between microstructural features. Fatigue microcracks that initiated fracture upon overload were found to be spatially correlated with elevated intracortical porosity but not elevated mineralization.

Fracture risk is known to increase with increasing age (Albrand *et al.*, 2003; Sornay-Rendu *et al.*, 2005; Sanders *et al.*, 2006; Sornay-Rendu *et al.*, 2007) and intracortical porosity also increases with age, especially in postmenopausal women (Stein *et al.*, 1999; Thomas *et al.*, 2005; Norman *et al.*, 2008; Burghardt *et al.*, 2010b; Zebaze *et al.*, 2010; Macdonald *et al.*, 2011). As such, characterization of intracortical porosity may be able to improve current fracture prediction deficiencies (Sornay-Rendu *et al.*, 2007) especially since intracortical porosity is poorly correlated with BMD (Zebaze *et al.*, 2010; Kazakia *et al.*, 2011).

Loading mode has also been shown to influence the fracture susceptibility of cortical bone. Although direct *in vivo* measurements of strain were not available for the

human femur, compressive principal strains were shown to be dominant during *in vivo* loading of human tibiae (Lanyon *et al.*, 1975; Burr *et al.*, 1996; Milgrom *et al.*, 2000). Studies have shown a clear biomechanical deficit when bones are loaded opposite to habitual loading (Reilly and Currey, 1999; Nyman *et al.*, 2009). Therefore, the human femoral specimens of this study were anticipated to have experienced predominantly compressive strains *in vivo*, and were hypothesized to be correspondingly weaker after being subjected to *in vitro* cyclic tension compared to cyclic compression. Furthermore, the tensile overload was hypothesized to cause longitudinal microcracks generated in cyclic compression to be redirected along a perpendicular (transverse) path which would act as a toughening mechanism; conversely, transverse microcracks generated in cyclic tension were hypothesized to continue transverse propagation.

The factors that may influence fracture susceptibility are numerous; therefore, an approach aimed at identifying and fully characterizing the critical event that ultimately leads to fracture could lead to improved understanding of fracture etiology and new strategies for clinical fracture risk assessment. The new methods in Chapter 3 may be suited to elucidate the microstructural mechanisms leading to changes in fracture susceptibility with increasing age and different modes of loading.

Therefore, the overall objective of this study was to provide a preliminary assessment for the utility of the new methods developed in Chapter 3 to investigate the effects of age and loading mode on the fracture susceptibility of human cortical bone specimens. Therefore, this study also expanded upon the methods and work performed in Chapter 3 by including specimens from four human female donors divided between two age groups (50-64, i.e., post-menopausal and 80-94) and three loading groups including

compressive fatigue, tensile fatigue, and a non-loaded control group. The specific aims were to (1) measure the spatial distribution of intracortical porosity and mineralization levels in segmented micro-CT images of human cortical bone specimens prior to mechanical loading, (2) measure the accumulated microdamage in the same specimens after loading in cyclic uniaxial compression or tension to a prescribed level of damage using contrast-enhanced micro-CT, (3) measure the spatial correlation between intracortical porosity, mineralization, and damaged tissue at the fracture initiation site using registered images, and (4) assess differences in the degradation of mechanical properties and the spatial correlations due to differences in fatigue loading mode and tissue age group.

4.2 Materials and Methods

4.2.1 Specimen Preparation

Thirty-four femoral cortical bone specimens were prepared from the proximal diaphysis (Figure 4.1) of 58, 59, 81, and 83 year-old female tissue donors presenting no medical history of skeletal pathology or trauma. Based on the donors available for this study, specimens from each donor were pooled into two age groups for donors in their 50s and 80s. These groups were chosen to be consistent with age ranges (50-64 and 80-94 y/o) used in recent studies investigating fracture risk, BMD, and intracortical porosity (Shi *et al.*, 2009, Zebaze *et al.*, 2010). All tissues were obtained with donor consent (National Disease Research Interchange, Philadelphia, PA) and all protocols were approved by the Notre Dame Human Subjects Institutional Review Board. A 4.5 cm segment of the diaphysis, centered at 75% of the total femur length, was removed while

frozen. Paired specimen blanks were removed from each section using a low-speed diamond wafer saw (Isomet, Buehler, Lake Bluff, IL). Each specimen blank was kept hydrated with deionized (DI) water while machining into cylindrical "dog bone" specimens with a 10 mm gauge length and 3 mm gauge diameter (Figure 4.1) using a computer numerical controlled mill and lathe. Paired specimens were randomly divided into three loading groups: a non-loaded control group and cyclic uniaxial compression and tension groups. Specimens were kept hydrated in phosphate buffered saline (PBS) at all times and stored at −20°C wrapped in gauze in airtight containers during interim periods. Note that the cortical bone tissue from the four donors could have yielded a maximum of forty-eight specimens; however, fourteen specimens were not included in the study for various reasons. Nine specimens, typically the tensile fatigue specimens from the anterior and posterior quadrants, were unable to be machined due to high levels of porosity and/or a lack of sufficient cortical thickness, but most often, due to a lack of sufficient cortical thickness. The group assignment methodology was designed such that the primary anatomic quadrant halves were assigned to the non-loaded control and compression fatigue groups, and the remaining adjacent tissue, which often lacked sufficient cortical thickness and/or volume for machining, was assigned to the tensile fatigue group. Three specimens were excluded after fracturing prematurely during set-up for the fatigue loading phase. Two tensile fatigue specimens were excluded from the study because the fracture initiated outside the specimen gauge section. The resulting number of specimens assigned to each group is summarized in Table 4.1. Finally, note that the number of donors and specimens was limited in this study to provide a preliminary assessment of the utility of relatively time-consuming methods.

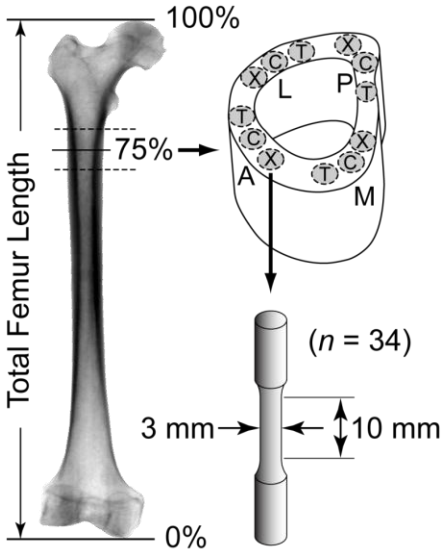

Figure 4.1: Schematic diagram showing a human femur and the locations from which paired specimens were machined. Note that in each anatomic quadrant (A=anterior, P=posterior, M=medial, and L=lateral) three paired specimens were systematically assigned to the non-loaded control (X), compressive fatigue (C), or tensile fatigue (T) loaded groups.

TABLE 4.1

GROUP SIZES BY AGE GROUP AND ANATOMIC QUADRANT

		Age and Quadrant							
		50's				80's			
Group	Total	A	P	M	L	A	P	M	L
Control	15	2	2	2	2	2	1	2	2
Compression	13	2	2	2	2	2	1	1	1
Tension	6	0	2	1	1	0	0	1	1

4.2.2 Micro-CT Imaging (Step 1)

The entire gauge section of each specimen was imaged by micro-CT (μCT-80, Scanco Medical AG, Brüttisellen, Switzerland) at each of three sequential steps: (1) as-prepared (Figure 4.2), (2) after cyclic loading and labeling fatigue microdamage, and (3) after fracture due to an overload. The micro-CT setup, scanning parameters, Gaussian filter settings, and segmentation details were identical to those described previously in Chapter 3.

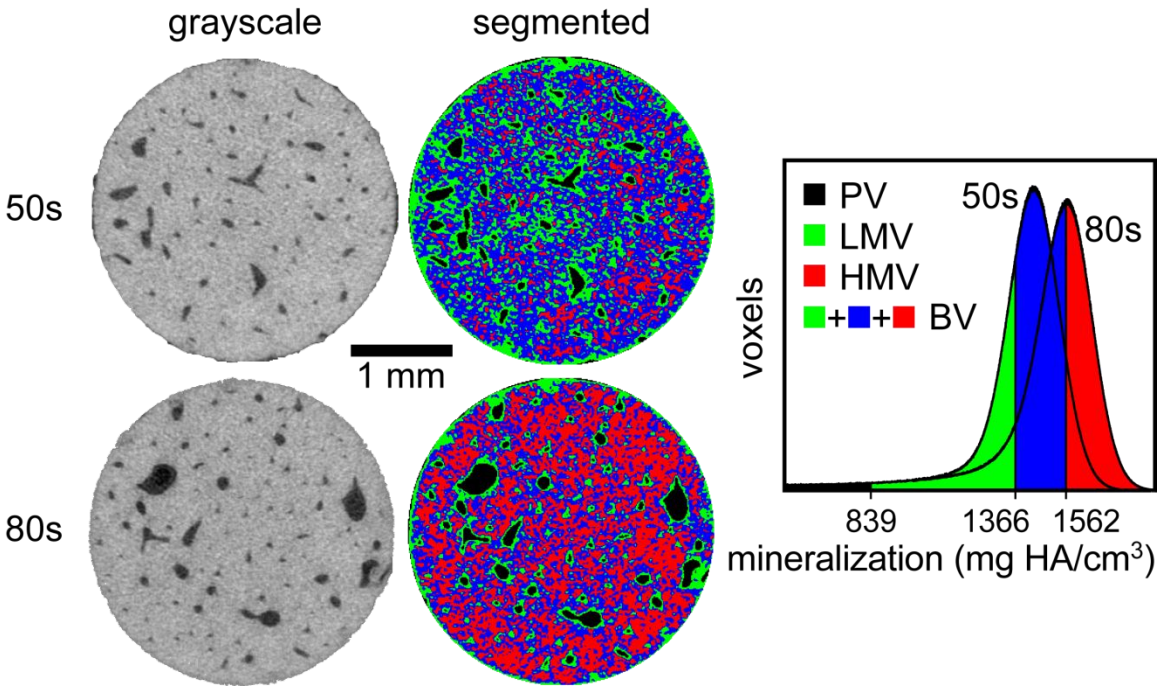

Figure 4.2: Grayscale and corresponding segmented micro-CT images for transverse cross-sections at mid gauge length and histograms for the entire gauge section of the median (PV/TV) specimen in each age group showing the segmentation and distribution of intracortical porosity (PV), and low (LMV) and high (HMV) mineral level volumes.

4.2.3 Fatigue Loading and Microdamage Labeling (Step 2)

Paired specimens were either not loaded (control) or subjected to cyclic uniaxial compression or tension at 2 Hz with a sinusoidal waveform in an ambient PBS bath under load control using an electromagnetic test instrument (Bose ElectroForce 3300, Bose Corp., Eden Prairie, MN). Loaded specimens were first preconditioned with a maximum compressive or tensile stress of 40 MPa for 240 cycles. Following preconditioning, specimens were subjected to a maximum cyclic compressive stress of 75 MPa ($R = 0.1$) or a maximum cyclic tensile stress of 50 MPa ($R = 0.1$) in the gauge section until achieving a 5% reduction in secant modulus. The secant modulus degradation during fatigue loading was calculated as the percent reduction in instantaneous secant modulus relative to the initial secant modulus. The initial secant modulus was defined as the average secant modulus of the first 20 cycles during fatigue loading. The total number of loading cycles was recorded upon reaching the predetermined secant modulus degradation for each specimen.

Note that the lower stress level used for tensile compared to compressive fatigue was determined by a pilot study investigating maximum cyclic tensile stresses ranging from 45 to 75 MPa. Five of five initial trial specimens either reached the 5% stiffness loss or fractured in less than 350 cycles when loaded in cyclic tension to the same stress level (75 MPa) as compressive fatigue specimens. Therefore, a second set of six specimens was used to systematically determine an appropriate tensile fatigue stress with the goal of reaching the stiffness loss at approximately the same number of cycles as compression fatigue specimens. Despite relatively little variation in the amount of porosity of the six specimens (9.08 ± 1.52%), the number of cycles required to reach the 5% stiffness loss was highly variable and found to be very sensitive to the applied tensile

stress magnitude. Differences of only 5 MPa in tensile stress magnitude resulted in substantial differences in the required number of cycles to reach 5% stiffness loss. For example, a 5 MPa change in the stress level resulted in a change in the required number of cycles of 10^5. A maximum tensile fatigue stress of 50 MPa was selected based on the required number of cycles to reach 5% stiffness loss for the six pilot specimens. This stress level enabled the 5% stiffness loss to be reliably achieved without premature fracture.

All specimens were stained by barium sulfate precipitation to label preexisting microdamage and/or microdamage resulting from fatigue loading using methods previously described and validated (Landrigan *et al.*, 2011; Turnbull *et al.*, 2011). Specimens were imaged again by micro-CT, as described previously in Chapter 3. The ratio of damage volume to bone volume (DV/BV) was adopted as a measure of microdamage (Landrigan *et al.*, 2011; Turnbull *et al.*, 2011). The gauge section was segmented to reveal labeled microdamage (DV), which was overlaid on micro-CT images of the as-prepared specimens using image registration (Analyze 10.0, Mayo Foundation for Medical Education and Research) (Figure 4.3). Non-specific staining of tissue porosity and exterior specimen surfaces was minimized in a series of two steps. First, the segmented BV of each as-prepared specimen was applied as an inclusion mask to the corresponding segmented DV after registration such that the resulting image volume contained only stain within the bone matrix or BV, not stain within the PV. Second, a 100 μm (10 voxels) peel was applied to the DV to remove non-specific $BaSO_4$ staining on the exterior specimen surface (Landrigan *et al.*, 2011).

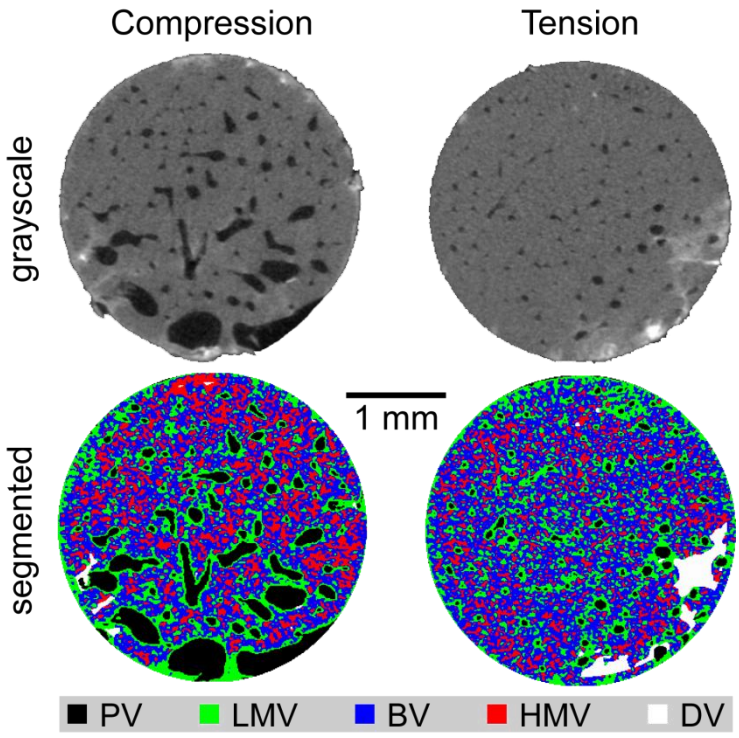

Figure 4.3: Grayscale and segmented transverse micro-CT images of a representative compressive and tensile fatigue specimen after fatigue damage and $BaSO_4$ staining showing stained DV (white overlay) in close proximity to intracortical porosity.

4.2.4 Tensile Overload (Step 3)

All specimens were hydrated in PBS for 5 h prior to overload, loaded to failure in uniaxial tension at 25 mm/s, and imaged again by micro-CT as described previously in Chapter 3. Micro-CT images of fractured specimens (Figure 4.4) were registered with micro-CT images of the as-prepared specimens to identify the fracture initiation site by the presence of DV on the fracture surface of loaded specimens. The elastic modulus (E), ultimate tensile strength (UTS), strain-to-failure (ε_f), and work of fracture (w_f) were calculated from measured force-displacement data and dimensions of the specimen gauge section (Roeder, 2013). The ultimate tensile strength (UTS) was measured as the

maximum stress. Strain-to-failure was calculated as the percent strain at fracture. The work of fracture was measured by the area under the load-displacement curve at fracture.

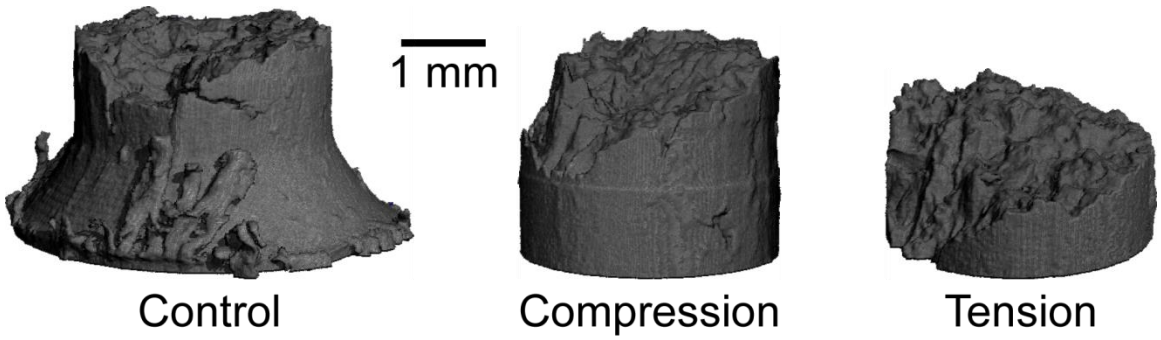

Figure 4.4: Segmented micro-CT reconstructions showing representative fracture surfaces for a non-loaded control, and compressive and tensile fatigue group specimens. The fracture surfaces of compressive and tensile fatigue group specimens were typically tortuous and oblique, whereas the fracture surfaces of control group specimens were transverse and relatively smooth.

4.2.5 Analytical and Statistical Methods

The normalized two-point correlation function, or probability density function (PDF), for encountering PV, HMV, LMV, or DV as a function of the three-dimensional (3-D) radial distance from either the DV that initiated fracture (fatigue loaded groups only), or all damage sites (DVs) (control and loaded groups), was computed using a custom MATLAB script (Appendix A.1) as described previously in Chapter 3. Note that the PDF computation for DV excluded DV voxels in each DV cluster of origin, such that the DV PDF result for any given cluster of DV was exclusive of itself. For example, the PDF for DV from the fracture initiation site cluster of DV is exclusive of the DV voxels in the fracture initiation site DV.

Mean PDF values for PV, HMV, LMV, and DV were compared to random probability (PDF = 1) using a Mann-Whitney *U*-test for nonparametric data with a

hypothesized mean of 1 (JMP 10.0, SAS Institute, Cary, NC). Mean PDF values for the fracture initiation site versus all damage sites (DVs) were compared for each feature of interest (PV, HMV, LMV, and DV) using a Wilcoxon Signed Rank test for paired, nonparametric data. These and all other continuous variables were tested for normality using a Shapiro-Wilk W test (JMP). For normally distributed variables, differences between groups were investigated using one-way analysis of variance (ANOVA) and *post hoc* comparisons were made using a *t*-test or, for more than two groups, a Tukey's HSD test. For non-normally distributed variables, differences between groups were investigated using Kruskal-Wallis non-parametric ANOVA and *post hoc* comparisons were made using a Steel-Dwass test. DV/BV was correlated with the number of loading cycles using linear least squares regression. The level of significance for all tests was $p < 0.05$.

4.3 Results

4.3.1 The Spatial Distribution of Microarchitectural Features

Segmented, 3-D micro-CT reconstructions of as-prepared (Figure 4.2) and fatigue loaded (Figure 4.3) specimens revealed the spatial distribution of intracortical porosity (PV), low and high levels of mineralization (LMV and HMV, respectively), and damage (DV). The mean ± standard deviation intracortical porosity volume fraction for all specimens in this study was 5.1 ± 2.1%. Visual inspection of segmented micro-CT images revealed LMV was in close spatial proximity to PV, as expected of tissue surrounding Haversian canals, while HMV was observed to be heterogeneously

distributed within the BV in between PVs, presumably corresponding to interstitial tissue (Figure 4.2 and Figure 4.3).

4.3.2 Intracortical Porosity was Higher in the Older Age Group

Intracortical porosity (PV) measured by micro-CT was observed to increase significantly ($p < 0.05$, Tukey's HSD) in pooled specimens from the younger (50s) to older (80s) age group (Figure 4.5). Note that this trend was influenced by a significant increase in PV with age observed in the anterior anatomic quadrant ($p < 0.05$, *t*-test). The posterior quadrant of the older age group was comprised of only two specimens preventing statistical analysis. In contrast, the difference between age groups was not statistically significant for either the medial or lateral quadrants. Overall, the posterior quadrant exhibited the greatest porosity, followed by the anterior, then medial, and lateral quadrants, and the difference between the posterior and lateral quadrants was statistically significant in pooled specimens from both age groups ($p < 0.05$, Tukey's HSD) (Figure 4.5). A two-way ANOVA model for non-pooled specimens indicated age group ($p < 0.0005$, ANOVA) and anatomic quadrant ($p < 0.0005$, ANOVA) were significant predictors of PV/TV, but the age and quadrant interaction term was not statistically significant ($p = 0.06$, ANOVA).

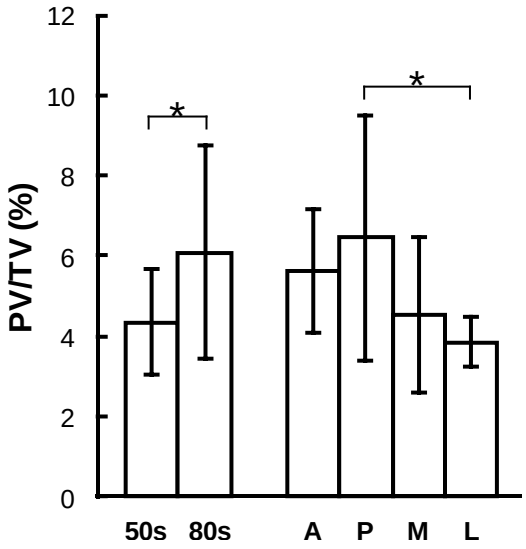

Figure 4.5: Intracortical porosity measured in segmented micro-CT images increased significantly in pooled specimens from the younger (50s) to older (80s) age group. The intracortical porosity in the anterior (A) and posterior (P) anatomic quadrants was greater than that of the medial (M) and lateral (L) quadrants for pooled specimens from both age groups, but only the difference between the P and L quadrants was statistically significant. * $p < 0.05$, Tukey's HSD.

4.3.3 Microdamage was Increased in Fatigue Loaded Specimens

DV/BV was not correlated with the number of fatigue loading cycles for either compression ($p > 0.2$) or tension ($p > 0.5$). Microdamage accumulation (DV/BV) was increased in both compressive ($p < 0.01$, Steel-Dwass) and tensile ($p = 0.07$, Steel-Dwass) fatigue loaded specimens compared to non-loaded control specimens (Figure 4.6), but the increase for tensile fatigue specimens was not statistically significant due to an underpowered sample size. Microdamage accumulation was increased for specimens from the younger donors compared to the older donors for the compression fatigue group (Figure 4.7), but this difference was also not statistically significant ($p = 0.06$, *t*-test) due to an underpowered sample size. A retrospective power analysis concluded that ten additional specimens in each group would be expected to provide a

significant difference ($\alpha = 0.05$) with a power of 0.8 (JMP). In the pooled age groups, the amount of microdamage in the compression fatigue group was significantly increased compared to the control group ($p < 0.05$, *t*-test). The tensile fatigue group included only two specimens in the older (80s) age group, which prevented statistical analysis.

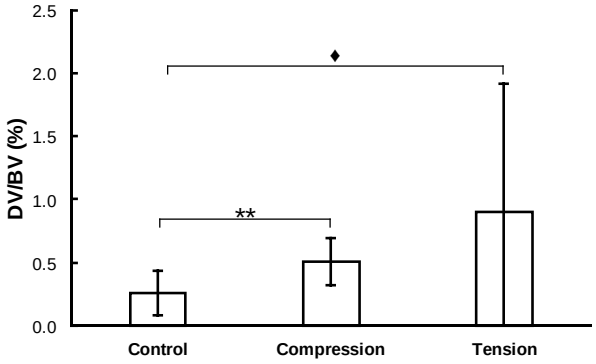

Figure 4.6: The ratio of $BaSO_4$ stain volume to bone volume (DV/BV) measured in segmented micro-CT images was increased for loaded groups compared to the non-loaded control group. ** $p < 0.01$, Steel-Dwass. ♦ $p = 0.07$, Steel-Dwass.

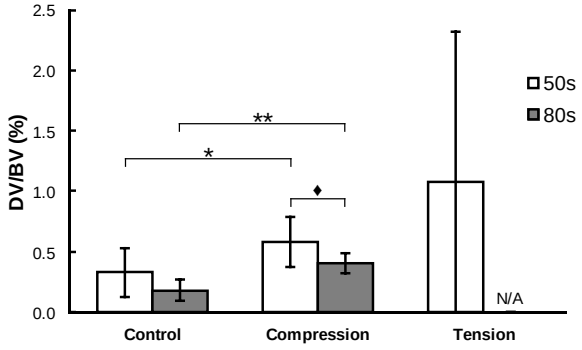

Figure 4.7: The ratio of $BaSO_4$ stain volume to bone volume (DV/BV) measured in segmented micro-CT images was increased for the younger (50s) compared to older (80s) age group among the compression fatigue specimens ($p = 0.06$, *t*-test) and for both age groups of the compression fatigue loaded group compared to the respective non-loaded control group. The tension fatigue group included only two specimens in the older (80s) age group, which prevented statistical analysis. * $p < 0.05$, *t*-test. ** $p < 0.01$, *t*-test. ♦ $p = 0.06$, *t*-test.

4.3.4 Tensile Overload Mechanical Properties Decreased for Fatigue Loaded Specimens

The accumulated microdamage was sufficient to significantly compromise the mechanical properties of fatigue loaded specimens compared to control specimens upon the tensile overload (Figure 4.8) (Table 4.2). Compression fatigue specimens exhibited an approximately 8% reduction in elastic modulus ($p < 0.001$, Tukey's HSD), 50% decrease in ultimate tensile stress ($p < 0.0001$, Steel-Dwass), 60% decrease in strain-to-failure ($p < 0.0001$, Steel-Dwass), and 80% decrease in work of fracture ($p < 0.0001$, Steel-Dwass), compared to non-loaded control specimens. Tension fatigue specimens exhibited an approximately 5% reduction in elastic modulus, but this difference was not statistically significant ($p = 0.12$, Tukey's HSD), 40% decrease in ultimate tensile stress ($p < 0.01$, Steel-Dwass), 50% decrease in strain-to-failure ($p < 0.01$, Steel-Dwass), and 75% decrease in work of fracture ($p < 0.01$, Steel-Dwass), compared to non-loaded control specimens.

Tensile and compressive fatigue loading protocols resulted in similar mechanical property degradation compared to the non-loaded control group (Figure 4.8). The ultimate tensile strength (UTS) ($p < 0.05$, Steel-Dwass) for tensile fatigue specimens was less compromised compared to compression fatigue specimens upon the tensile overload. However, the difference between loaded groups was a fraction of the difference between the pooled loaded groups and non-loaded control group for the UTS (~25%), and a smaller fraction for all other mechanical properties.

All differences in mechanical properties were not statistically significant between age groups within the non-loaded control or compression fatigue group (Table 4.2). Elastic modulus was increased for the older compared to younger specimens within the non-loaded control and compression fatigue groups, but these differences were not

significant ($p < 0.1$, *t*-test). The tension fatigue group included only two specimens in the older (80s) age group, which prevented statistical analysis.

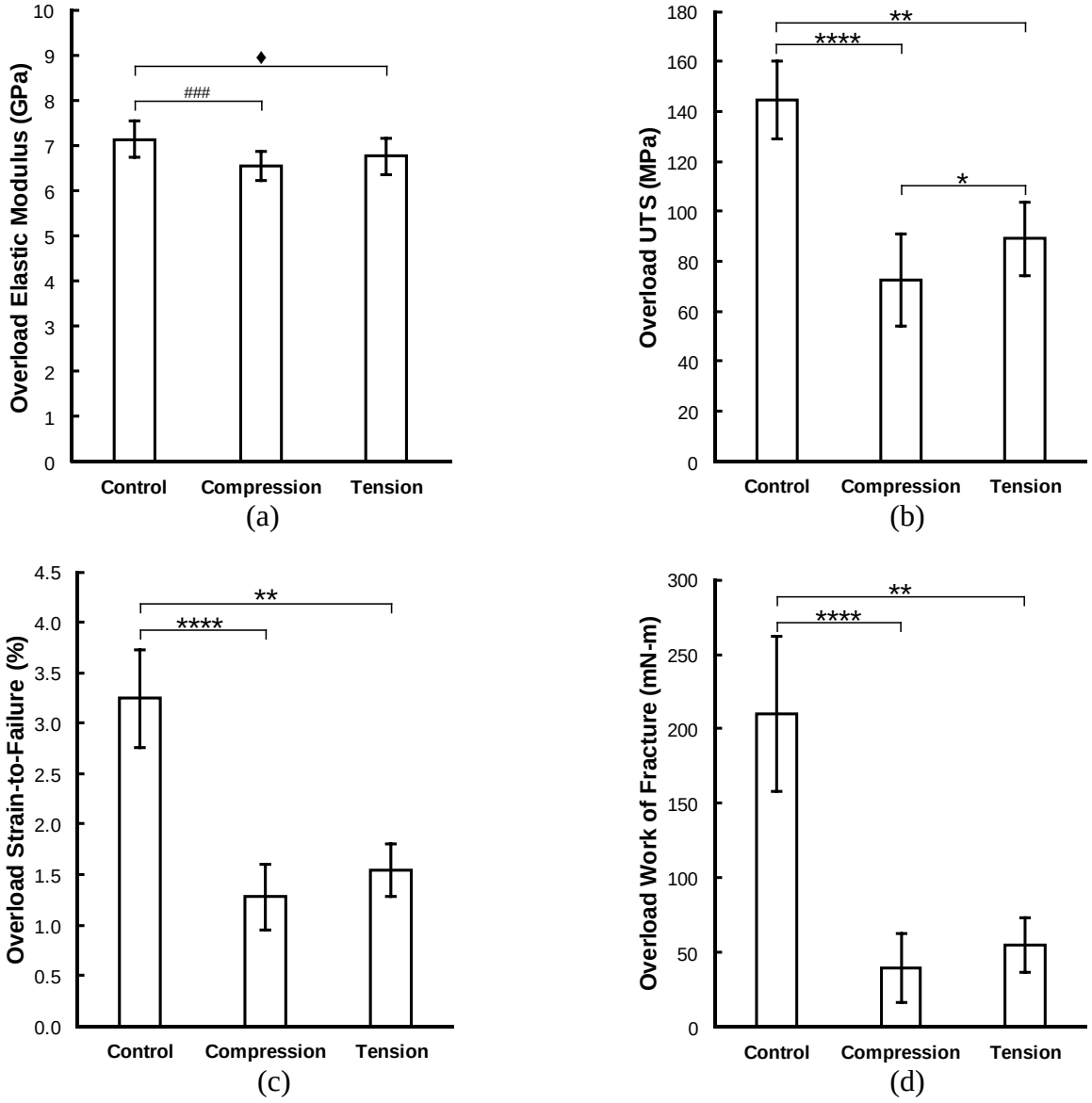

Figure 4.8: The (a) elastic modulus, (b) ultimate tensile strength, (c) strain-to-failure, and (d) work of fracture were compromised in compression and tension fatigue groups compared to the non-loaded control group. ### $p < 0.001$, Tukey's HSD. ♦ $p = 0.12$, Tukey's HSD. * $p < 0.05$, Steel-Dwass. ** $p < 0.01$, Steel-Dwass. **** $p < 0.0001$, Steel-Dwass.

TABLE 4.2

MEAN (± STANDARD DEVIATION) TENSILE OVERLOAD MECHANICAL PROPERTIES BY GROUP AND DONOR AGE

		Tensile Overload Mechanical Properties			
Group	Age	*E* (GPa)	*UTS* (MPa)	ε_f (%)	w_f (mN-m)
Control	All	7.1 (0.4)	145 (16)	3.3 (0.5)	210 (52)
	50s	7.0 (0.4)	139 (6)	3.2 (0.4)	200 (35)
	80s	7.3 (0.2)	152 (21)	3.3 (0.6)	220 (70)
Compression	All	6.6 (0.3)	73 (18)	1.3 (0.3)	39 (23)
	50s	6.4 (0.3)	68 (14)	1.2 (0.3)	33 (17)
	80s	6.8 (0.3)	80 (23)	1.4 (0.4)	49 (30)
Tension	All	6.8 (0.4)	89 (15)	1.5 (0.3)	55 (18)
	50s	6.6 (0.3)	90 (16)	1.6 (0.3)	57 (21)
	80s	n/a	n/a	n/a	n/a

n/a = not applicable.

4.3.5 Qualitative Comparison of Specimen Fracture Surfaces

The final fracture upon overload of compression fatigue loaded specimens exhibited a tortuous oblique surface (Figure 4.4) due to the presence of longitudinal microcracks (DV) previously initiated in cyclic compression, often noticeably adjacent to intracortical porosity (PV). In contrast, control specimen fracture surfaces exhibited a relatively smooth transverse fracture plane (Figure 4.4). The fracture surfaces of tension fatigue loaded specimens were more varied; four of six specimens exhibited a tortuous fracture surface (Figure 4.4), while the other two specimens exhibited a relatively smooth, transverse fracture plane. The DV that initiated fracture was able to be clearly identified by the presence of stained DV on the fracture surface of all 13 compression and

6 tension fatigue specimens. In contrast, no stained DV was apparent on the fracture surface of all 15 control specimens.

4.3.6 Spatial Correlations for Compression Fatigue Specimens

PDFs averaged for all compression fatigue specimens revealed a greater than random probability for PV located spatially adjacent to the DV that initiated fracture and a random probability for HMV located spatially adjacent to the DV that initiated fracture (Figure 4.9a). This difference was similar for all damage sites as PV and HMV exhibited a greater, and near random probability, respectively, of being located adjacent to all damage sites (DVs) (Figure 4.9b). Interestingly, DV exhibited a greater than random probability of being located adjacent to both the DV that initiated fracture and all DVs, with increasing probability moving away from the DVs of origin and reaching a maximum at approximately 400-500 μm (Figure 4.9).

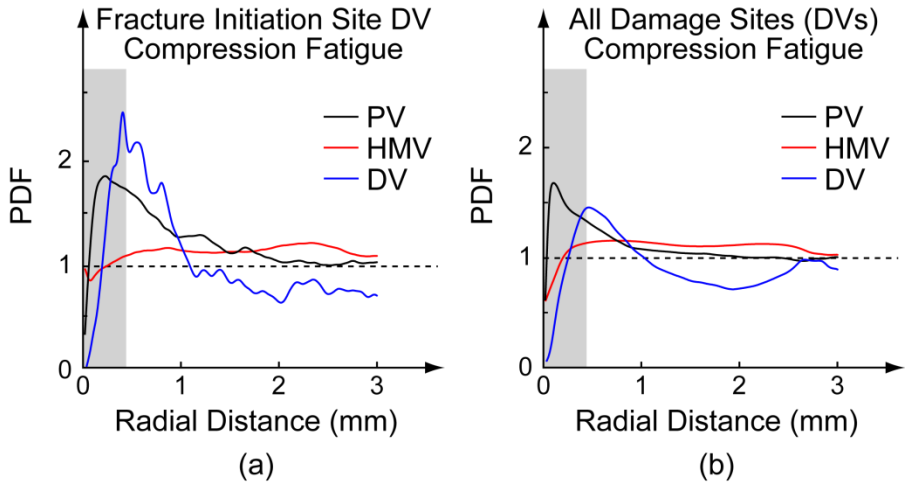

Figure 4.9: The probability density function (PDF) for intracortical porosity (PV), high mineral level volume (HMV), and damage (DV) near (a) the fracture initiation site or (b) all damage sites (DVs) and averaged for all specimens in the compression fatigue group. Note that PDF = 1 corresponds to random probability.

For compression fatigue specimens (Figure 4.10), the mean PDF for PV within 440 μm of the fracture initiation site or all damage sites was significantly greater than random probability ($p < 0.01$, Mann-Whitney). In contrast, the mean PDF for HMV within 440 μm of the fracture initiation site or all damage sites was not statistically different from random probability. The mean PDF for LMV was not statistically different from random probability near the fracture initiation site and minimally greater than random probability near all damage sites ($p < 0.05$, Mann-Whitney). The mean PDF revealed DV exhibited random probability of being located spatially adjacent to either the DV that initiated fracture or all damage sites, but was highly variable for the DV that initiated fracture. No differences were observed between the mean PDF measured from the fracture initiation site and all damage sites for any feature of interest.

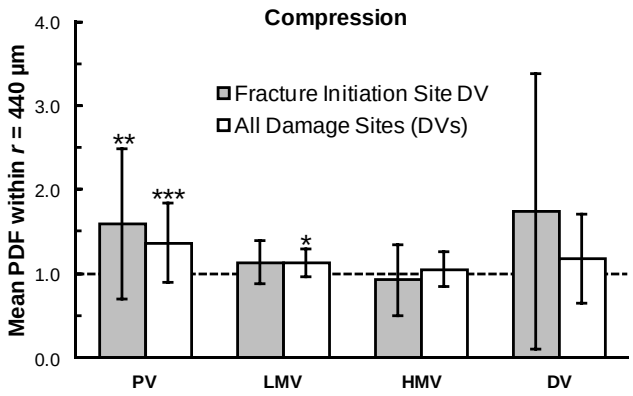

Figure 4.10: The mean value of the probability density function (PDF), for intracortical porosity (PV), low (LMV) and high (HMV) mineral level volume, and damage (DV) within $r = 440$ μm from the fracture initiation site or all damage sites (DVs) of the compression fatigue group. Error bars show one standard deviation of the mean. Note that PDF = 1 corresponds to random probability. * $p < 0.05$, Mann-Whitney vs. 1. ** $p < 0.01$, Mann-Whitney vs. 1. *** $p < 0.001$, Mann-Whitney vs. 1.

4.3.7 Spatial Correlations for Tension Fatigue and Control Specimens

For tensile fatigue specimens, all features of interest exhibited random probability of being located spatially adjacent to either the DV that initiated fracture or all damage sites (Figure 4.11 and Figure 4.12). No differences were observed between the mean PDF measured for the fracture initiation site and all damage sites of the tension fatigue group for any feature of interest. For control specimens (Figure 4.12), PV, LMV, and DV exhibited significantly greater than random probability ($p < 0.01$, Mann-Whitney vs. 1), while HMV exhibited random probability, of being located spatially adjacent to all damage sites.

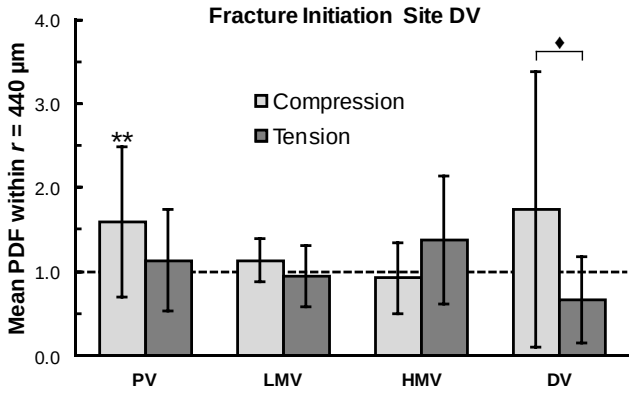

Figure 4.11: The mean value of the probability density function (PDF), for intracortical porosity (PV), low (LMV) and high (HMV) mineral level volume, and damage (DV) within $r = 440$ µm from the fracture initiation site of the compression and tension fatigue groups. Error bars show one standard deviation of the mean. Note that PDF = 1 corresponds to random probability. ** $p < 0.01$, Mann-Whitney vs. 1. ♦ $p < 0.1$, Mann-Whitney.

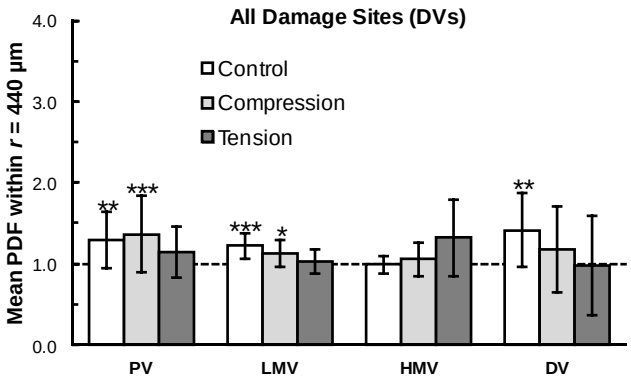

Figure 4.12: The mean value of the probability density function (PDF), for intracortical porosity (PV), low (LMV) and high (HMV) mineral level volume, and damage (DV) within r = 440 µm from all damage sites (DVs) of the non-loaded control and fatigue loaded groups. Error bars show one standard deviation of the mean. Note that PDF = 1 corresponds to random probability. * $p < 0.05$, Mann-Whitney vs. 1. ** $p < 0.01$, Mann-Whitney vs. 1. *** $p < 0.001$, Mann-Whitney vs. 1.

4.3.8 Effect of Loading Mode on Spatial Correlations

The mean PDF for DV within the first 440 µm from the fracture initiation site DV generated by cyclic compression was greater than that for cyclic tension (Figure 4.11), but the difference was not statistically significant ($p < 0.1$, Mann-Whitney) due to high variability among both loaded groups and an underpowered sample size. No other differences were observed between the mean PDF values within each feature of interest as a function of loading group, whether for the fracture initiation site or all damage sites.

4.3.9 Effect of Age on Spatial Correlations within the Compressive Fatigue Group

The average PDF plots and mean PDF values were observed to follow different trends between specimens from donors in their 50s (Figure 4.13a and Figure 4.14) versus 80s (Figure 4.13b and Figure 4.15) for compression fatigue specimens. Among specimens from younger (50s) donors, PV exhibited greater than random probability ($p < 0.01$, Mann-Whitney) of being located spatially adjacent to the DV that initiated

fracture or all damage sites (DVs), while all other features of interest were not, or only minimally, different from random probability. In contrast, all features of interest among specimens from the older (80s) donors exhibited random probability of being located spatially adjacent to the DV that initiated fracture or all damage sites (DVs). Furthermore, the mean PDF for PV near the fracture initiation site was greater for specimens from younger (50s) donors compared to older (80s) donors, but this result was not statistically significant (p = 0.09, Mann-Whitney) due to an underpowered sample size (Figure 4.16).

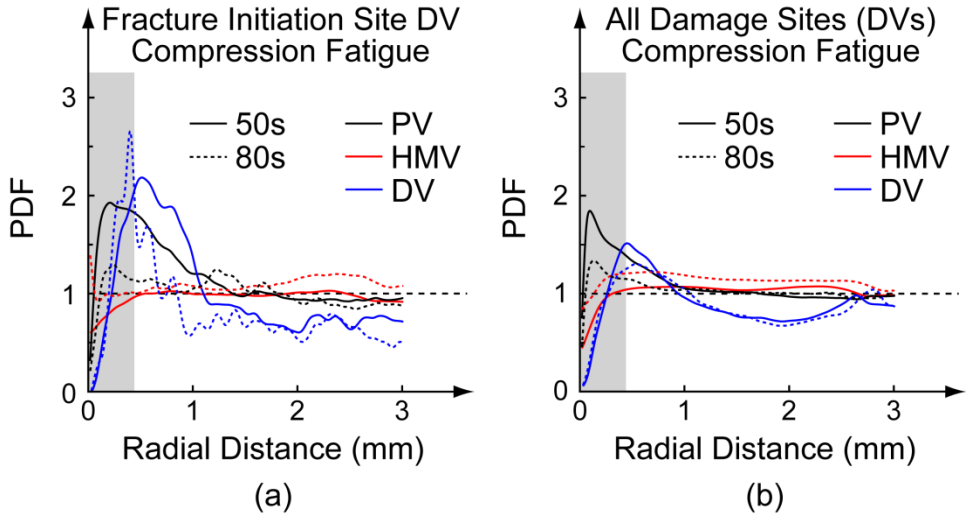

Figure 4.13: The probability density function (PDF), for intracortical porosity (PV), low (LMV) and high (HMV) mineral level volume, and damage (DV) split by age group and averaged for all specimens near (a) the fracture initiation site or (b) all damage sites (DVs) of the compression fatigue loaded group. Note that PDF = 1 corresponds to random probability.

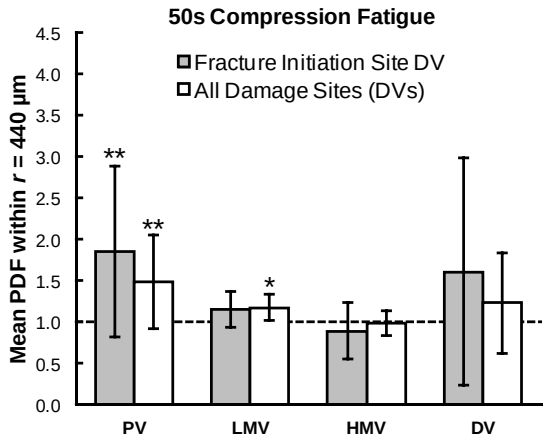

Figure 4.14: The mean value of the probability density function (PDF), for intracortical porosity (PV), low (LMV) and high (HMV) mineral level volume, and damage (DV) within r = 440 µm from the fracture initiation site or all damage sites (DVs) of specimens from younger (50s) donors in the compression fatigue loaded group. Error bars show one standard deviation of the mean. Note that PDF = 1 corresponds to random probability. * $p < 0.05$, Mann-Whitney vs. 1. ** $p < 0.01$, Mann-Whitney vs. 1.

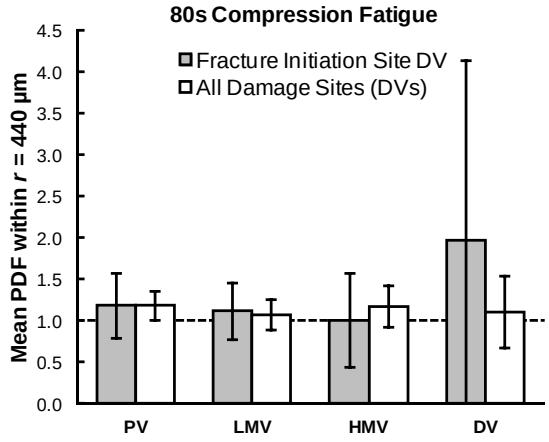

Figure 4.15: The mean value of the probability density function (PDF), for intracortical porosity (PV), low (LMV) and high (HMV) mineral level volume, and damage (DV) within r = 440 µm from the fracture initiation site or all damage sites (DVs) of specimens from older (80s) donors in the compression fatigue loaded group. All features of interest exhibited random probability of being located spatially adjacent to the DV that initiated fracture or all damage sites (DVs). Error bars show one standard deviation of the mean. Note that PDF = 1 corresponds to random probability.

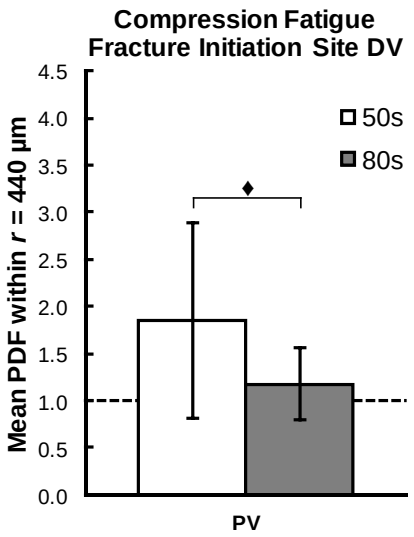

Figure 4.16: The mean value of the probability density function (PDF), for intracortical porosity (PV) within r = 440 µm from the fracture initiation site DV of specimens from younger and older donors in the compression fatigue loaded group. Error bars show one standard deviation of the mean. Note that PDF = 1 corresponds to random probability. ♦ p = 0.09, Mann-Whitney.

4.4 Discussion

The overall objective of this study was to determine whether the new methods developed in Chapter 3 could be utilized to investigate the effects of age and loading mode on fracture susceptibility in human cortical bone specimens. Intracortical porosity increased with age (Figure 4.5) but was less than mean values reported in literature for both age groups. Microdamage accumulation was increased for tensile and compressive fatigue groups compared to the non-loaded control group (Figure 4.6) and for specimens from younger (50s) donors compared to older (80s) donors in the compression fatigue group (Figure 4.7). Tensile overload mechanical properties decreased for tensile and compressive fatigue groups compared to the non-loaded control group (Figure 4.8), but differences were not statistically significant between age groups within the non-loaded

control or compression fatigue group (Table 4.2). Spatial correlations revealed intracortical porosity (PV) was located spatially adjacent to both the DV that initiated fracture and all damage sites in specimens from younger (50s) donors at greater than random probability (Figure 4.14). However, increased age diminished the spatial association of PV, and all other features of interest, to random probability for the fracture initiation site and all damage sites (Figure 4.15). Taken together, these results suggested the methods developed in Chapter 3 are well-suited for investigations of fracture susceptibility in human cortical bone specimens of varying age and fatigue loading mode.

4.4.1 Intracortical Porosity Increased with Age

The volume fraction of intracortical porosity increased from the younger to older age group (Figure 4.5) and, consistent with previous studies (Feik *et al.*, 1997; Bousson *et al.*, 2000; Bousson *et al.*, 2001; Thomas *et al.*, 2005), the volume fraction of intracortical porosity was greatest in the posterior and anterior anatomic quadrants compared to the medial and lateral quadrants. Intracortical porosity exhibited the expected trends with age and anatomic quadrant; however, the mean levels of intracortical porosity, 4% (50s) and 6% (80s), were lower than the mean values reported previously as ~9% (50s) and ~14% (80s) (Feik *et al.*, 1997; Bousson *et al.*, 2000). Interestingly, mean levels of intracortical porosity have also been reported as ~4% (50s) and ~6% (80s) (Thomas *et al.*, 2005), consistent with this study. The sample sizes of each of these three previous studies were consistent with approximately 170 donors. The lower intracortical porosity values were observed in an Anglo-Celtic Australian cohort of specimens harvested during 1990-1993 and 1998, compared to the Bousson study in which specimens were harvested from Caucasian Portuguese donors who died between 1910-1935. These other studies

also commented on the large variability, especially with increasing age, in the volume fraction of intracortical porosity between specimens, which implied the requirement of large sample sizes.

4.4.2 Microdamage Increased for Fatigue Loaded Specimens

The level of microdamage, measured by micro-CT as a ratio of the segmented, contrast-enhanced damage volume to bone volume (DV/BV), increased for compressive and tensile fatigue loaded groups compared to non-loaded control specimens, but the increase measured in tensile fatigue specimens was not statistically significant (Figure 4.6). This result, as well as the extent of measured microdamage accumulation (compression: 0.5 ± 0.2% and tension: 0.9 ± 1.0%), was consistent with Chapter 3 and previous studies which utilized similar methods and stopping criteria for generating damage by fatigue loading and imaging (Landrigan *et al.*, 2011). Interestingly, microdamage accumulation was found to be increased for specimens from younger donors compared to specimens from older donors from the compression fatigue group (Figure 4.7), but this difference was not statistically significant. Nevertheless, the loading protocol successfully generated microdamage, as the amount of microdamage in the compression fatigue group was significantly increased compared to the non-loaded control group in both age groups (Figure 4.7). The tension fatigue group included only two specimens from the older (80s) age group, which prevented statistical analysis.

4.4.3 Tensile Overload Mechanical Properties Decreased for Fatigue Loaded Specimens

The accumulated microdamage was sufficient to significantly compromise the mechanical properties of fatigue loaded specimens compared to control specimens upon the tensile overload (Figure 4.8) (Table 4.2). The overload mechanical properties for

compression fatigue specimens were similar but less compromised than those from Chapter 3 (Table 3.2) as a result of fatigue loading to a lower stiffness loss (5% secant modulus loss), compared to that from Chapter 3 (10%).

Overall, in spite of the lower stress level used for tensile compared to compressive fatigue, the loading protocols resulted in a similar level of microdamage accumulation and a similar mechanical property degradation compared to the non-loaded control group (Figure 4.8). Microdamage accumulation was expected to be similar among fatigue loaded groups, since both were loaded to a constant (5%) secant modulus degradation. In contrast, mechanical properties were hypothesized to exhibit differences between fatigue loaded groups, but the results indicated the differences were not statistically significant or only minimally different. Furthermore, tensile fatigue specimens exhibited a greater mean ultimate tensile strength (UTS) (Figure 4.8) compared to compressive fatigue specimens.

The lack of differences in mechanical properties between fatigue loaded groups was unexpected for a few reasons. Longitudinal compressive fatigue microcracks were expected to be redirected along a perpendicular (transverse) path (i.e., a toughening mechanism) upon the tensile overload. In contrast, transverse tensile fatigue microcracks were expected to continue transverse propagation upon the tensile overload, thus not benefitting from redirection strengthening mechanisms. Further, previous studies have shown a clear biomechanical deficit for bone tissue loaded opposite to habitual loading (Reilly and Currey, 1999; Nyman *et al.*, 2009). Although direct *in vivo* measurements of strain were not available for the human femur, *in vivo* principal compressive strains in human tibiae dominated during most activities (Lanyon *et al.*, 1975; Burr *et al.*, 1996;

Milgrom *et al.*, 2000). Therefore, the human femoral specimens of this study were anticipated to have experienced compressive strains *in vivo*, and were expected to be correspondingly weaker after being subjected to *in vitro* cyclic tension compared to cyclic compression. One possible explanation for the lack of differences in mechanical properties between fatigue loaded groups could be that tensile fatigue microcracks propagated more tortuously than originally hypothesized, and could have been deflected from purely transverse propagation by the presence of Haversian canals, as shown previously (Koester *et al.*, 2008).

All differences in mechanical properties were not statistically significant between age groups within the non-loaded control or compression fatigue group (Table 4.2). Elastic modulus was increased for the older compared to younger specimens within the non-loaded control and compression fatigue groups, but these differences were not statistically significant ($p < 0.1$, *t*-test). This result was unexpected given the higher overall porosity in specimens from older donors compared to younger donors (Figure 4.5). However, this result, and those for all mechanical properties as a function of age, may be explained by the fact that the differences in the volume fractions of porosity were not statistically significant ($p > 0.2$, *t*-test) between the two age groups for either the control or compression fatigue specimens. The lack of differences in intracortical porosity volume fractions was attributed to the underpowered sample size. The tension fatigue group included only two specimens in the older (80s) age group, which prevented statistical analysis.

4.4.4 Effect of Fatigue Loading Mode on Specimen Fracture Surfaces

Consistent with the results of Chapter 3 (Figure 3.4), compression fatigue specimens exhibited a tortuous oblique fracture surface upon the tensile overload, and non-loaded control fracture surfaces were transverse and smooth (Figure 4.4). The fracture surfaces of tensile fatigue specimens exhibited an inconsistent morphology that was predominantly tortuous but occasionally smooth (Figure 4.4). This observation suggests that propagating tensile microcracks were typically deflected due to crack growth inhibitors (e.g., osteons and cement lines of Haversian porosity) consistent with prior studies (Mohsin *et al.*, 2006b; Koester *et al.*, 2008) and not allowed to propagate linearly on the otherwise more energetically favorable transverse plane (i.e., the plane normal to the application of the tensile load).

4.4.5 Spatial Correlations for Compression Fatigue Specimens

Individual specimen PDFs for all microstructural features of interest revealed inter-specimen variability, which was consistent with the results of Chapter 3 (Figure A.2). Therefore, the mean PDF was utilized as a consistent metric for assessing the probability of spatial proximity (i.e., within 440 μm) to either the damage that initiated fracture or all damage sites for objects of interest. Consistent with the results of Chapter 3 (Figure 3.6), the mean PDF for PV was greater than random probability near the fracture initiation site (Figure 4.10). Contrary to previous results (Figure 3.6), the mean PDF for PV was also greater than random probability near all damage sites (Figure 4.10). This finding suggests PV was an important feature and consistently influenced the initiation and/or propagation of all damage, including the damage confirmed to lead to fracture. The mean PDF for HMV within 440 μm of the fracture

initiation site or all damage sites was not statistically different from random probability (Figure 4.10). This result is similar to the result in Chapter 3 (Figure 3.6) and suggests HMV may be less critical to both the initiation and propagation of damage compared to PV.

4.4.6 Spatial Correlations for Tension Fatigue and Control Specimens

For tension fatigue specimens, all features of interest exhibited random probability of being located spatially adjacent to either the DV that initiated fracture or all damage sites (Figure 4.11 and Figure 4.12). Furthermore, no differences were observed between the mean PDF measured for the fracture initiation site and all damage sites of the tension fatigue group for any feature of interest. These results could be due to an underpowered sample size ($n = 6$) within the tensile fatigue group. Interestingly, HMV appeared to exhibit greater than random probability of being located spatially adjacent to either the DV that initiated fracture or all damage sites (Figure 4.11 and Figure 4.12), but a retrospective power analysis concluded 30 additional specimens in the tensile fatigue group would be necessary to provide a significant difference ($\alpha = 0.05$) with a power of 0.8 (JMP).

For control specimens, the mean PDF revealed that PV, LMV, and DV exhibited significantly greater than random probability of being located spatially adjacent to all damage sites, while HMV exhibited random probability (Figure 4.12). This result is similar to that of Chapter 3 for PV; however, the random spatial proximity of HMV to all damage sites within non-loaded control specimens is not consistent with Chapter 3 but is consistent with compression fatigue specimens within this study.

4.4.7 Effect of Loading Mode on Spatial Correlations

All differences in the values of the mean PDF were not statistically significant between loading modes for any given feature of interest, whether in spatial proximity to the fracture initiation site or all damage sites (Figure 4.11 and Figure 4.12). Interestingly, the mean PDF for DV within the first 440 μm from the fracture initiation site DV generated by cyclic compression was greater than that for cyclic tension (Figure 4.11), but the difference was not statistically significant. This result was influenced by the high variability exhibited in the mean PDF for DV within the first 440 μm from the fracture initiation site DV in both loaded groups. Upon closer inspection, the pooled mean PDF for DV within the first 440 μm from the fracture initiation site DV exhibited a statistically significant inverse correlation with the volume of the fracture initiation site DV ($p < 0.05$, $R^2 = 0.21$). This result may be influenced by a limitation of the methods for selecting the cluster of connected DVs at the fracture initiation site. Specifically, there could be multiple DVs in the vicinity of the selected fracture initiation site DV that appear connected to the observer, but are not discretely connected. Note that 3-D connectivity was defined within the custom MATLAB code (Appendix A.1) as face, edge, or corner connections between the discrete cubic voxels of micro-CT images segmented for DV. As such, the actual DVs contained in the discretely-connected fracture initiation site DV may be a smaller volume than intended. Consequently, the other DVs that appeared connected, but were not discretely connected, become classified with all damage sites, thus increasing the probability of spatial proximity between the fracture initiation site DV and all damage sites. Nonetheless, this limitation was not expected to affect the mean PDF results for other features of interest, as the

normalizations inherent to the PDF calculations account for differences in the number of voxels of origin (e.g., the number of voxels in fracture initiation site DV).

4.4.8 Effect of Age on Spatial Correlations within the Compressive Fatigue Group

Among specimens from the younger (50s) donors, intracortical porosity (PV) was found to be spatially correlated with the fracture initiation site microdamage and all damage sites (DVs), while highly mineralized tissue (HMV) was not spatially correlated with either damage site (Figure 4.13 and Figure 4.14). This suggests that elevated intracortical porosity, but not elevated mineralization, influenced the initiation and/or propagation of microdamage, including the microdamage responsible for fracture initiation. In contrast, among specimens from the older (80s) donors, both PV and HMV were randomly distributed near either damage site (Figure 4.13 and Figure 4.15). This suggests the initiation and/or propagation of microdamage among specimens from older donors was not influenced by elevated PV or HMV. Moreover, specimens from younger donors exhibited an increased probability of PV located near the fracture initiation site DV compared to older specimens (Figure 4.16). Taken together, these results suggest porosity may have a greater effect on the fracture susceptibility of specimens from younger donors compared to specimens from older donors in this study.

4.4.9 Other Considerations

The procedure outlined in Chapter 3 for the removal of non-specific surface stain was modified in this study such that only a 10-voxel peel (radius reduction) of the outer specimen surface was performed, as recommended in a previous study (Landrigan *et al.*, 2011), and was not followed by a 25 volume percent penetration criterion as in Chapter 3. This modification was not anticipated to affect the results of PDF calculations, but was

necessary because the penetration exclusion criterion inappropriately removed interior stain voxels. Therefore, the 10-voxel peel of the outer specimen surface is recommended as a more robust, semi-automated method of non-specific surface stain removal.

A pilot study was conducted to test the hypothesis that the $BaSO_4$ staining protocol (utilized in this study and Chapter 3) did not alter the overload mechanical properties of machined cortical bone specimens. Eleven cortical bone specimens were machined according to the methods outlined in this study and randomly assigned to two treatment groups: a non-$BaSO_4$ control ($n = 5$) and a $BaSO_4$ ($n = 6$) group. All specimens were kept hydrated in phosphate buffered saline (PBS) at all times and stored at −20°C wrapped in gauze in airtight containers during interim periods. The $BaSO_4$ specimens were stained according to the methods outlined in this study and control specimens were kept frozen. Following staining, the $BaSO_4$ specimens were frozen. All specimens were thawed and rehydrated in PBS for 4 h prior to a tensile overload according to the methods outlined in this study. Overload mechanical properties (elastic modulus, ultimate tensile strength, strain-to-failure, and work of fracture) were individually compared between the groups and found to be independent of $BaSO_4$ treatment ($p > 0.85$, *t*-test).

4.5 Conclusions

The effects of age and loading mode on the fracture susceptibility of human cortical bone specimens were investigated using the new methods developed in Chapter 3. Intracortical porosity increased with age, but only by a relatively small magnitude. Microdamage resulting from compressive and tensile fatigue loading was increased compared to the non-loaded control group. Mechanical properties were

compromised in the compressive and tensile fatigue groups compared to the non-loaded control group, but differences between loaded groups were not statistically significant, or only minimal. Overall, spatial correlations revealed intracortical porosity was located in spatial proximity to all damage sites, including the damage that initiated fracture. This trend was exhibited in specimens from younger (50s) donors, but not in specimens from older (80s) donors, suggesting intracortical porosity may have a greater effect on the fracture risk of younger compared to older specimens in this study.

CHAPTER 5:

FUTURE WORK: STATISTICAL PREDICTION OF FRACTURE SUSCEPTIBILITY BY MEASUREMENTS OF INTRACORTICAL POROSITY IN HUMAN CORTICAL BONE

5.1 Introduction

The new methods described in Chapters 3 and 4 could be used to predict the fracture susceptibility of cortical bone. The importance of the interaction between fatigue microdamage and intracortical porosity was highlighted in Chapter 3. Fatigue microcracks that initiated fracture upon overload were found to be spatially correlated with elevated intracortical porosity but not elevated mineralization. The effects of loading mode and age on fracture susceptibility in cortical bone specimens were investigated in Chapter 4. Fatigue loading was observed to significantly compromise mechanical properties upon a subsequent tensile overload. However, differences in the mechanical properties between age groups of the compression fatigue specimens were not statistically significant. This result was attributed to the small distribution in the volume fraction of intracortical porosity among specimens included in Chapter 4. On the other hand, the volume fraction of intracortical porosity among specimens included in Chapter 3 spanned a much wider range. Nonetheless, intracortical porosity was found to be spatially correlated at greater than random probability with the fracture initiation site in Chapter 4.

Intracortical porosity increases with age, especially in postmenopausal women (Stein *et al.*, 1999; Thomas *et al.*, 2005; Norman *et al.*, 2008; Burghardt *et al.*, 2010b; Zebaze *et al.*, 2010; Macdonald *et al.*, 2011). Moreover, 70-90% of all fractures in old age occur at non-vertebral sites (Miller *et al.*, 2002; Sornay-Rendu *et al.*, 2005; Sanders *et al.*, 2006; Shi *et al.*, 2009), which are 70-80% cortical bone. Similar to many engineering materials, increased intracortical porosity has been shown to reduce important biomechanical properties of bone such as elastic modulus, strength, and fracture toughness under static loading conditions (Currey, 1962; Currey, 1988; Schaffler and Burr, 1988; Yeni *et al.*, 1997; Kennedy *et al.*, 2009). Interestingly, intracortical porosity is poorly correlated with BMD (Zebaze *et al.*, 2010; Kazakia *et al.*, 2011), suggesting the shortcomings of fracture risk measured by BMD alone may be improved if used in conjunction with 3-D measurements of the spatial distribution and characteristics of intracortical porosity. Therefore, a hypothesis was proposed: fracture susceptibility and the fracture initiation site can be predicted by spatial measurements of pore size or pore area (Po.Ar).

The overall goal of this study was to apply the results from Chapters 3 and 4 to explore the feasibility of predicting cortical bone fracture susceptibility from spatial measurements of microstructural features including intracortical porosity. The specific objectives were to correlate the overload mechanical properties of compression fatigue specimens from (1) Chapter 3, (2) Chapter 4, and (3) pooled specimens from Chapters 3 and 4 with global measurements for damage accumulation (DV/BV), intracortical porosity (PV/TV), mineralization (HMV), and spatial measurements for the transverse area of the pore associated with the fracture initiation site (Po.Ar).

5.2 Materials and Methods

All compression fatigue loaded specimens and associated data from Chapters 3 and 4 were used for the statistical analyses of this study. The pore nearest the fracture initiation site was identified and the transverse pore area (Po.Ar) was measured using a custom MATLAB script. In all cases, the distance from the site of fracture initiation to the closest pore was less than 250 μm.

For each grouping of data, (1) Chapter 3, (2) Chapter 4, and (3) Chapters 3 and 4 pooled, the tensile overload mechanical properties were correlated with measurements for compression fatigue damage accumulation (DV/BV), intracortical porosity (PV/TV), high mineralization (HMV), and the transverse area of the pore associated with the fracture initiation site (Po.Ar) using linear least squares regression. The level of significance for all tests was $p < 0.05$.

5.3 Results and Discussion

5.3.1 Mechanical Property Correlations to Global Measurements

Linear regression correlations between tensile overload mechanical properties and global measurements for features of interest using Chapter 3 data (Table 5.1) revealed mechanical properties were inversely correlated with intracortical porosity (PV/TV) and microdamage accumulation (DV/BV) but were not positively correlated with high mineralization (HMV/BV).

In contrast, linear regression correlations between tensile overload mechanical properties and global measurements for features of interest using Chapter 4 data

(Table 5.2) revealed mechanical properties were inversely correlated with DV/BV but were not correlated with PV/TV or HMV/BV.

Upon pooling data for Chapters 3 and 4 (Table 5.3), linear regression correlations between tensile overload mechanical properties and global measurements for features of interest revealed mechanical properties were inversely correlated (PV/TV and DV/BV) or positively correlated (HMV) with global measurements for features of interest. However, PV/TV exhibited greater statistical significance and coefficient of determination (R^2) compared to that for HMV.

DV/BV exhibited a strong predictive power for decreased mechanical properties, but is currently unable to be measured clinically and therefore does not provide utility for fracture risk assessments. HMV exhibited a weak predictive power, even for pooled specimens. PV/TV also exhibited a strong predictive power; however, as a global measure, PV/TV cannot predict a specific fracture location.

TABLE 5.1

P-VALUES AND (R^2) FOR THE LINEAR REGRESSION CORRELATIONS BETWEEN TENSILE OVERLOAD MECHANICAL PROPERTIES AND GLOBAL MEASUREMENTS FOR FEATURES OF INTEREST USING CHAPTER 3 DATA

	Tensile Overload Mechanical Properties			
Measurement	*E* (GPa)	*UTS* (MPa)	ε_f (μstrain)	w_f (mN-m)
PV/TV	<0.05 (0.72)	0.1 (0.43)	0.06 (0.55)	<0.005 (0.85)
HMV	NS	NS	NS	NS
DV/BV	<0.005 (0.89)	0.07 (0.52)	NS	0.08 (0.50)

NS = $p > 0.1$.

TABLE 5.2

P-VALUES AND (R^2) FOR THE LINEAR REGRESSION CORRELATIONS BETWEEN TENSILE OVERLOAD MECHANICAL PROPERTIES AND GLOBAL MEASUREMENTS FOR FEATURES OF INTEREST USING CHAPTER 4 DATA

	Tensile Overload Mechanical Properties			
Measurement	*E* (GPa)	*UTS* (MPa)	ε_f (μstrain)	w_f (mN-m)
PV/TV	NS	NS	NS	NS
HMV	NS	NS	NS	NS
DV/BV	0.07 (0.27)	NS	0.09 (0.23)	NS

NS = $p > 0.1$.

TABLE 5.3

P-VALUES AND (R^2) FOR THE LINEAR REGRESSION CORRELATIONS BETWEEN TENSILE OVERLOAD MECHANICAL PROPERTIES AND GLOBAL MEASUREMENTS FOR FEATURES OF INTEREST USING CHAPTER 3 AND 4 POOLED DATA

	Tensile Overload Mechanical Properties			
Measurement	*E* (GPa)	*UTS* (MPa)	ε_f (μstrain)	w_f (mN-m)
PV/TV	<.0001 (0.74)	<0.001 (0.49)	<0.005 (0.42)	<0.01 (0.31)
HMV	<0.05 (0.26)	<0.05 (0.23)	<0.01 (0.30)	<0.05 (0.27)
DV/BV	<.0001 (0.89)	<0.001 (0.47)	<0.01 (0.33)	<0.05 (0.26)

The lack of statistical significance in the linear regression correlations for Chapter 4 specimens (Table 5.2) was attributed to the limited range of intracortical porosity (5.1 ± 2.1%). For comparison, the mean ± standard deviation porosity volume fraction for all specimens from Chapter 3 was 19.2 ± 11.9%.

5.3.2 Mechanical Property Correlations to Spatial Measurements

Correlations measured by linear least squares regressions were not statistically significant between mechanical properties and the transverse area of the pore associated with the fracture initiation site (Po.Ar) for either Chapter 3 or 4 data, individually (Table 5.4). However, the pooled data exhibited statistically significant inverse correlations for elastic modulus, ultimate tensile strength, and strain-to-failure, but the positive correlation for work of fracture was not statistically significant due to an underpowered sample size (Table 5.4) (Figure 5.1). Interestingly, only work of fracture (Figure 5.1d) exhibited an improved fit using a nonlinear exponential decay model (R^2 = 0.24) compared to the linear least squares regression (R^2 = 0.18).

TABLE 5.4

P-VALUES AND (R^2) FOR THE LINEAR REGRESSION CORRELATIONS BETWEEN TENSILE OVERLOAD MECHANICAL PROPERTIES AND PORE AREA USING ALL DATA FROM CHAPTERS 3 AND 4

	Tensile Overload Mechanical Properties			
Data Source	*E* (GPa)	*UTS* (MPa)	ε_f (μstrain)	w_f (mN-m)
Chapter 3	NS	NS	NS	NS
Chapter 4	NS	NS	NS	NS
Pooled 3 and 4	<0.01 (0.35)	<0.05 (0.24)	<0.01 (0.30)	0.06 (0.18)

NS = $p > 0.1$.

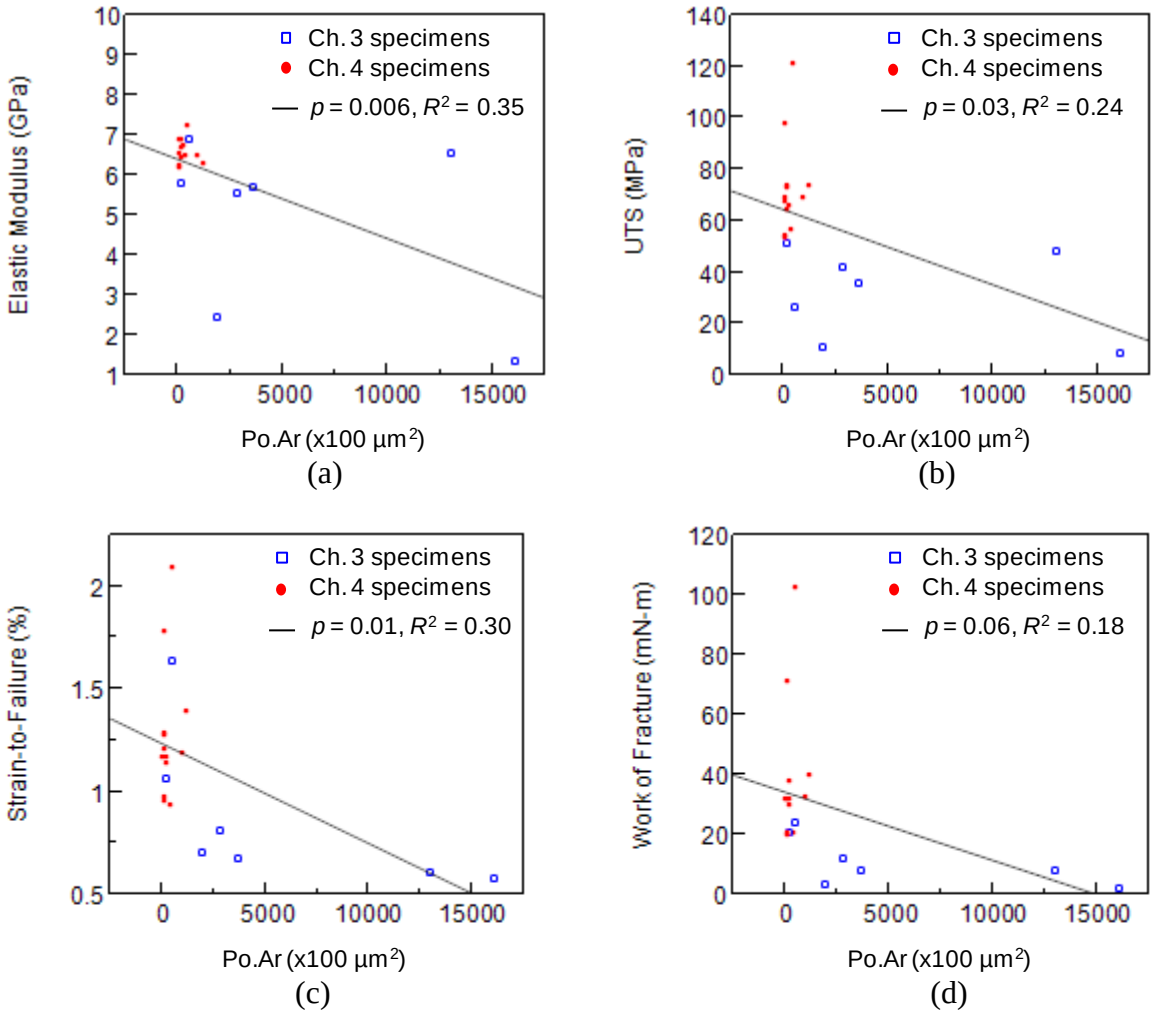

Figure 5.1: Mechanical properties, (a) elastic modulus, (b) ultimate tensile strength (UTS), (c) strain-to-failure, and (d) work of fracture, were inversely correlated with the transverse area of the pore associated with the fracture initiation site (Po.Ar) for compressive fatigue specimens pooled from Chapters 3 and 4.

As a consequence of differences in the porosity volume fraction, the mean ± standard deviation fracture initiation site Po.Ar for Chapter 4 specimens was 0.03 ± 0.04 mm^2, compared to 0.54 ± 0.64 mm^2 for Chapter 3 specimens. This result suggests that the intracortical pores of the specimens from Chapter 4 were uniform and consistent with the morphology of normal Haversian porosity, in contrast to the specimens from Chapter 3 which exhibited a larger and more irregular pore morphology,

indicative of intracortical resorption occurring with age and/or metabolic bone diseases. Po.Ar and PV/TV were not correlated for specimens in Chapters 3 or 4 (Figure 5.2), due to an underpowered sample size. However, the pooled data set exhibited a statistically significant correlation measured by linear regression between Po.Ar and PV/TV ($p < 0.0001$, $R^2 = 0.6$) (Figure 5.2).

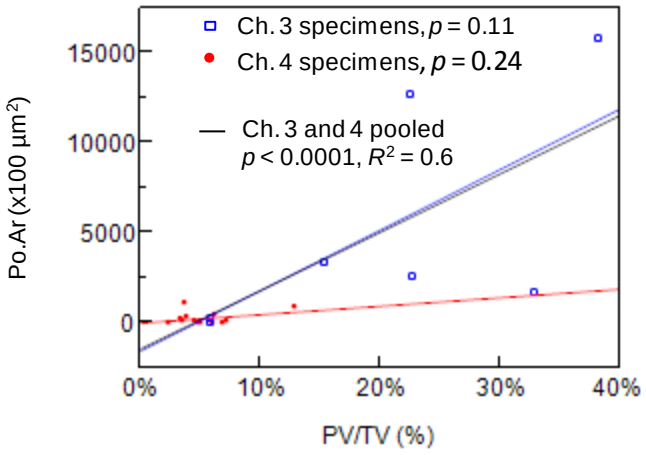

Figure 5.2: Correlations between the fracture initiation site pore area (Po.Ar) and intracortical porosity volume fraction (PV/TV) for Chapter 3 and 4 specimens were individually not statistically significant. However, a significant correlation was observed between Po.Ar and PV/TV for the Chapter 3 and 4 pooled data set ($p < 0.0001$, $R^2 = 0.6$).

The main limitation and possible source of error in pooling the data from both studies was that specimens from Chapter 3 were subjected to 10% modulus loss, compared to 5% loss for Chapter 4 specimens. Nonetheless, the results of this study suggest there is promise for specific, detailed spatial measurements of intracortical porosity (e.g., Po.Ar) to improve fracture risk predictions by highlighting the importance of critical spatial characteristics from global measurements (e.g., PV/TV) otherwise assumed to be homogeneous. Moreover, measurements of specific characteristics (e.g., Po.Ar) could provide a test statistic against a patient population. For example, fracture

risk could be predicted by pore characteristics associated with the fracture initiation site that are repeatedly observed to be in the 95^{th} percentile, e.g., of the distribution of pore characteristics. In this way, patient-specific spatial measurements of intracortical porosity could be used to improve fracture risk prediction.

5.4 Conclusions

Mechanical properties were more correlated with intracortical porosity (PV/TV) than high mineralization (HMV). However, PV/TV is a global measure that cannot predict the location of fracture. Therefore, spatial characteristics of intracortical porosity, such as pore area (Po.Ar), may also improve fracture risk assessments by establishing the unique aspects of porosity most susceptible to interaction with fatigue microdamage resulting in fracture. Therefore, this study motivated future work exploring statistical predictions of fracture susceptibility based on spatial measurements of intracortical porosity.

APPENDIX A:

CHAPTER 3 SUPPLEMENTARY MATERIAL

A.1 Custom MATLAB Code for 3-D Spatial Correlations Utilizing Probability Density Functions (PDFs)

A.1.1 MATLAB Code for Computation of 3-D Distance Histograms

```
%{
Prior to the code below, the following commands were executed:
  1) the segmented DV of a single specimen was loaded as a 3-D logical
     matrix.
  2) individual clusters of stain were identified using "bwconncomp",
     then labeled using "labelmatrix".
  3) the locations of each pixel in each cluster
     ('ConnStainInfo.PixelList') were output by "regionprops" with a
     "PixelList" request applied to the output of "labelmatrix".
  4) the failure site cluster of DV ('FailSiteConnComp') was identified
     by matching a previously-definded, user-selected voxel coordinate
     with the clusters of DV given by "labelmatrix".
  5) the current feature of interest was loaded and the row and column
     indices ('RowCol.Rows' and 'RowCol.Cols') of segmented voxels were
     stored for later use on a transverse slice-by-slice basis.
  6) the maximum distance ('MAXdist') was computed relative to the
     transverse dimensions of the 3-D feature of interest matrix and the
     user-selected number of longitudinal slices to evaluate from each DV
     ('NumSlicesEval').

After the code below, the following commands were executed:
  1) If the feature of interest was all voxels in the gauge section, the
     'ALL_DistObj' and 'FailSite_DistObj' variables were saved with a
     prefix denoting these vectors represented the maximum count of
     distances possible. For all other features of interest, the
     'ALL_DistObj' and 'FailSite_DistObj' variables were saved with a
     prefix denoting these vectors represented the actual count of
     distances to the current segmented object voxels.
%}
```

```
%initialize ALL_DistObj cell array
%  stores count of distances from All DVs
ALL_DistObj_DistObj=zeros(MAXdist,length(ConnStainInfo(:,1)));
ALL_DistObj_NumConnComp=zeros(length(ConnStainInfo(:,1)),1);
ALL_DistObj=cell(length(ConnStainInfo(:,1)),2);
ALL_DistObj(:,1)=num2cell(ALL_DistObj_DistObj,1)';
ALL_DistObj(:,2)=num2cell(ALL_DistObj_NumConnComp,2);
clear('ALL_DistObj_DistObj','ALL_DistObj_NumConnComp');

%initialize FailSite_DistObj cell array
%  stores count of distances from FailSite DV
FailSite_DistObj_DistObj=zeros(MAXdist,1);
FailSite_DistObj_NumConnComp=zeros(1,1);
FailSite_DistObj_ConnComp=zeros(1,1);
FailSite_DistObj=cell(1,3);
FailSite_DistObj{1,1}=FailSite_DistObj_DistObj;
FailSite_DistObj{1,2}=FailSite_DistObj_NumConnComp;
FailSite_DistObj{1,3}=FailSite_DistObj_ConnComp;
clear('FailSite_DistObj_DistObj','FailSite_DistObj_NumConnComp','FailSite_Di
  stObj_ConnComp');

matlabpool open 8 % open 8 cpu workers for parallel computation
for c=1:length(ConnStainInfo(:,1)) %loop over each stain cluster
   fprintf('clust:%d Y:%d M:%d D:%d H:%d M:%d S:%d\n',c,fix(clock))

   DistObj=zeros(MAXdist,1);%initialize count of distances

   PxlListLength=length(ConnStainInfo(c,1).PixelList(:,1)); %number of voxels
     of current DV cluster

   COLtemp=ConnStainInfo(c,1).PixelList(round(1:VoxSkip:PxlListLength),1);
     %extract "PcentEvalNum" percentage of all voxels, starting with first, e.g.,
     PcentEvalNum=5pcent, then every 20th voxel
   ROWtemp=ConnStainInfo(c,1).PixelList(round(1:VoxSkip:PxlListLength),2);
   SLICEtemp=ConnStainInfo(c,1).PixelList(round(1:VoxSkip:PxlListLength),3);

   parfor slice=RowCol_LOWslice:RowCol_HIGHslice

      rows=single(RowCol(slice).Rows);
      cols=single(RowCol(slice).Cols);

      if (isempty(rows) == 0) %if no data, then skip this slice instance

         VxlIdxs=find(bitand(SLICEtemp>=(slice-
           NumSlicesEval),SLICEtemp<=(slice+NumSlicesEval))); %these stain
           voxels fit within the NumSlicesEval criteria
```

```
if (isempty(VxlIdxs) == 0) %this confirms that there were voxels from the
 current stain cluster that fit the NumSlicesEval criteria... if none, then do
 nothing for this slice instance

   %calculate #columns each iteration based on fixed #rows of
       DistanceObjectNOW and 'int16' data type, i.e., 2-bytes per entry
  NumDistObjCols =
   floor((20e6)/(2*length(rows)));%MaxMemory[bytes]/(2BytesPerEntry
   *#rows)
   MemLoopIters=length(VxlIdxs)/NumDistObjCols; %number of
    iterations to go through all of necessary VxlIdxs
   if ((MemLoopIters-floor(MemLoopIters))==0) %no remainder, even
    number of column increments to reach length(VxlIdxs)
      MemLoopCols=NumDistObjCols.*ones(MemLoopIters,1);
   else %a remainder exists, so tack it on to the end of the MemLoopCols
    vector
      MemLoopCols =
       vertcat(NumDistObjCols.*ones(floor(MemLoopIters),1),length(VxlI
       dxs)-NumDistObjCols*floor(MemLoopIters));
   end

   StartVxl=1;
   for MemLoop=1:length(MemLoopCols)
      DistanceObjectNOW =
        zeros(length(rows),MemLoopCols(MemLoop),'int16');
      FinishVxl=(StartVxl-1)+MemLoopCols(MemLoop);
      for vxl=StartVxl:FinishVxl
         COL=COLtemp(VxlIdxs(vxl),1);
         ROW=ROWtemp(VxlIdxs(vxl),1);
         SLICE=SLICEtemp(VxlIdxs(vxl),1);

         DistanceObjectNOW(:,vxl-StartVxl+1)=sqrt((rows-ROW).^2 +
           (cols-COL).^2 + (slice-SLICE)^2);

         COL=[]; ROW=[]; SLICE=[];
      end %end of loop over voxels of current stain cluster that satisfy
        NumSlicesEval criteria

      NumDistObj=regionprops(DistanceObjectNOW,'Area');%this finds
        the number of voxels ("Area") at any distance, the result is in a
        structure array
      [~,Distances,NumVoxAtDist]=find([NumDistObj.Area]); %NOTE:
        the ~ character means I want to ignore this returned value since
        find([NumDistObj.Area]) produces a row vector, not a matrix
      DistObjTemp=zeros(MAXdist,1);
      DistObjTemp(Distances,1)=NumVoxAtDist;
```

```
                DistObj=DistObj+DistObjTemp;
                %NOTE: with the method above for calculating and then compiling
                %distances, there is NO NEED to worry about the single position
                %where distance can be calculated as "0"... this is because
                %regionprops() disregards 0's anyway!

                StartVxl=FinishVxl+1;

                NumDistObj=[]; Distances=[]; NumVoxAtDist=[];
              end %end of loop over columns for optimal memory usage

              NumDistObjCols=[]; MemLoopIters=[]; MemLoopCols=[];
            end %end of 'if empty VxlIdxs' check
          end %end of 'if empty rows' check

          rows=[]; cols=[]; VxlIdxs=[]; DistanceObjectNOW=[]; DistObjTemp=[];
        end %end of parallel computation loop over slices

        ALL_DistObj{c,1}=DistObj; %DistObj (i.e., the number of voxels of the
          current object at the given distances (given by the rows) from all the RDF
          origins analyzed for the current cluster
        ALL_DistObj{c,2}=length(COLtemp); %NumConnCompVxls (i.e., the
          number of individual RDF origins, that will be combined to form the TPCF)


        if (c==FailSiteConnComp)
          FailSite_DistObj{1,1}=DistObj; %DistObj (i.e., the number of voxels of the
            current object at the given distances (given by the rows) from all the RDF
            origins analyzed for the current cluster
          FailSite_DistObj{1,2}=length(COLtemp); %NumConnCompVxls (i.e., the
            number of individual RDF origins, that will be combined to form the
            TPCF)
          FailSite_DistObj{1,3}=c; %the Fail Site Conn Comp
        end

        clear('COLtemp','ROWtemp','SLICEtemp','DistObj')
      end %end of loop over stain clusters
      matlabpool close
```

A.1.2 MATLAB Code for Computation of PDFs from 3-D Distance Histograms

```
      %compute the max distance from all specimens
      MAXdistSpecimen=zeros(length(SpecimenList),1);
      for LoopSpecimen=1:length(SpecimenList)
        SpecimenNum=SpecimenList{LoopSpecimen};
        Directory=strcat(SpecimenNum,'/');
```

```
    PosAndDimsXYZ =
      open(strcat(Directory,'Images/',SpecimenNum,'_AIM_PositionAndDimension
      .mat'));
    Dim_XYZ=cell2mat(PosAndDimsXYZ.AIM_PositionAndDimension(2,1:3));
    clear('PosAndDimsXYZ');

    MAXdistSpecimen(LoopSpecimen,1)=ceil(sqrt(sum(Dim_XYZ(:).^2)));
end
MAXdist=max(MAXdistSpecimen);%used to initialize the size of the
  "PDF_{X,Y}vals" matrices (below)

%initialize variables
CrackDistDnorm=zeros(length(SpecimenList),length(ObjInterestList),2);%2 for
  number of "vox of interest", but in this case it's FailSite and AllDamage voxels
  as the second
CrackDistPDF=zeros(length(SpecimenList),length(ObjInterestList),2);
PDF_Xvals=zeros(MAXdist,length(SpecimenList),length(ObjInterestList),2);
PDF_Yvals=zeros(MAXdist,length(SpecimenList),length(ObjInterestList),2);
clear('MAXdistSpecimen','MAXdist');

for o=1:length(ObjInterestList)

    Object=ObjInterestList{o};

    if (strcmp(ObjInterestList{o},'STAIN')==1) %catch STAIN object case
        ObjectLoad='STAIN_ArtfctRemvd_Peel10';
    elseif (strcmp(ObjInterestList{o},'NOfsDV')==1) %catch NOfsDV object case
        ObjectLoad='STAIN_ArtfctRemvd_Peel10_NOfsDV';
    else
        ObjectLoad=Object;
    end

    fprintf('\tObject = GOBJ and %s\n',Object)

    LoopCount=0;
    for s=1:length(SpecimenList)
        ObjTime=tic;

        LoopCount=LoopCount+1;
        SpecimenNum=SpecimenList{s};
        Directory=strcat(SpecimenNum,'/');
        fprintf('\t\tSpecimen Number = %s ...',SpecimenList{s})

        %load the object TPCF distance and counts data (actual occurences
        %at each distance)
```

```
file1a =
  strcat('DistObjBinned_',SpecimenNum,'_',ObjectLoad,'_ALLConnComp_',
  VersionNumNOW);
file1b =
  strcat('DistObjBinned_',SpecimenNum,'_',ObjectLoad,'_FailSiteConnComp
  _',VersionNumNOW);
load(strcat(Directory,file1a,'.mat'))
load(strcat(Directory,file1b,'.mat'))
eval(['DistObjBinned_ALL = ' file1a ';']);
eval(['DistObjBinned_FailSiteStruct = ' file1b ';']);
clearvars DistObjBinned* -except DistObjBinned_ALL
  DistObjBinned_FailSiteStruct

%load the gobj TPCF distance and counts data (max possible
%occurences at each distance)
if (strcmp(ObjInterestList{o},'NOfsDV')==1) %catch NOfsDV object case
    file2a =
     strcat('DistAvailBinned_GOBJ_NOfsDV_',SpecimenNum,'_ALLConnC
     omp_',VersionNumNOW);
    file2b =
     strcat('DistAvailBinned_GOBJ_NOfsDV_',SpecimenNum,'_FailSiteCon
     nComp_',VersionNumNOW);
else
    file2a =
     strcat('DistAvailBinned_GOBJvoxels_',SpecimenNum,'_ALLConnComp
     _',VersionNumNOW);
    file2b =
     strcat('DistAvailBinned_GOBJvoxels_',SpecimenNum,'_FailSiteConnCo
     mp_',VersionNumNOW);
end
load(strcat(Directory,file2a,'.mat'))
load(strcat(Directory,file2b,'.mat'))
eval(['DistAvailBinned_GOBJvoxels_ALL = ' file2a ';']);
eval(['DistAvailBinned_GOBJvoxels_FailSiteStruct = ' file2b ';']);
clearvars DistAvailBinned* -except DistAvailBinned_GOBJvoxels_ALL
  DistAvailBinned_GOBJvoxels_FailSiteStruct

%sum together the contributions of each cluster into the ALL damage
%TPCF data (as imported, the data is still on a per stain cluster
%basis)
NumConnComp=length(DistAvailBinned_GOBJvoxels_ALL(:,1));%This
  calculates the number of connected components for the current specimen
DistObjBinned_ALLsummed =
  zeros(length(DistObjBinned_ALL{1,1}),1);%initialize
  DistObjBinned_ALLsummed
```

```
DistAvailBinned_GOBJvoxels_ALLsummed =
  zeros(length(DistAvailBinned_GOBJvoxels_ALL{1,1}),1);%initialize
  Avail_ALLsummed
for ConnCompNow=1:NumConnComp %1:NumConnComp INCLUDES
  the FailSiteConnComp
    DistObjBinned_ALLsummed = DistObjBinned_ALLsummed +
      DistObjBinned_ALL{ConnCompNow,1};
    DistAvailBinned_GOBJvoxels_ALLsummed =
      DistAvailBinned_GOBJvoxels_ALLsummed +
      DistAvailBinned_GOBJvoxels_ALL{ConnCompNow,1};
end
clear('NumConnComp',
 'DistObjBinned_ALL','DistAvailBinned_GOBJvoxels_ALL');


DistObjBinned_FailSite=DistObjBinned_FailSiteStruct{1,1};%distance and
  counts data
NumConnCompVxls_FailSite=DistObjBinned_FailSiteStruct{1,2};%the
  number of individual RDF origins, from which the results were combined
  to form the TPCF

DistAvailBinned_GOBJvoxels_FailSite =
  DistAvailBinned_GOBJvoxels_FailSiteStruct{1,1};%distance and counts
  data
NumConnCompVxls_GOBJvoxels_FailSite =
  DistAvailBinned_GOBJvoxels_FailSiteStruct{1,2};%the number of
  individual RDF origins, from which the results were combined to form the
  TPCF

if (NumConnCompVxls_FailSite ~=
 NumConnCompVxls_GOBJvoxels_FailSite)
    error('Number of ConnComp voxels should be the same for Object and
      GOBJ!');
end

clear('DistObjBinned_FailSiteStruct',
  'DistAvailBinned_GOBJvoxels_FailSiteStruct');


%the most basic, purely local distance normalization... what was there over
    what could have been there
DistanceNorm1 =
  DistObjBinned_FailSite./DistAvailBinned_GOBJvoxels_FailSite;%for
  FailSite
```

```
DistanceNorm2 =
  DistObjBinned_ALLsummed./DistAvailBinned_GOBJvoxels_ALLsumme
  d;%for ALLdamage

[RowsDnorm1]=find(~(isnan(DistanceNorm1)));%this omits NaN's
[RowsDnorm2]=find(~(isnan(DistanceNorm2)));%this omits NaN's

ValDistNormNoNAN1=DistanceNorm1(RowsDnorm1);%collect the non-
  NaN's
ValDistNormNoNAN2=DistanceNorm2(RowsDnorm2);%collect the non-
  NaN's


%FIGURE 1A: Most basic distance normalization figure (Dnorm) (FailSite)
FIGoneA=figure(1);
if (LoopCount==1); FIGoneAxes1=axes(); end
Xvalues1=(RowsDnorm1./100);%divide RowsDnorm by 100 to convert
  from voxels (10 um side) to mm
plot(FIGoneAxes1,Xvalues1,ValDistNormNoNAN1);
hold(FIGoneAxes1,'all')
ylim(FIGoneAxes1,[0 1])%0 and 1 are the absolute lower and upper bound,
  respectfully... either there's nothing of what could have been or there's
  everything...
xlim(FIGoneAxes1,[0 (NumSlicesEval/100)])
box off

%FIGURE 1B: Most basic distance normalization figure (Dnorm)
  (ALLsummed)
FIGoneB=figure(2);
if (LoopCount==1); FIGoneAxes2=axes(); end
Xvalues2=(RowsDnorm2./100);%divide RowsDnorm by 100 to convert
  from voxels (10 um side) to mm
plot(FIGoneAxes2,Xvalues2,ValDistNormNoNAN2);
hold(FIGoneAxes2,'all')
ylim(FIGoneAxes2,[0 1])%0 and 1 are the absolute lower and upper bound,
  respectfully... either there's nothing of what could have been or there's
  everything...
xlim(FIGoneAxes2,[0 (NumSlicesEval/100)])
box off


%Read in voxel count data for volume fraction normalizations
file3a=strcat('ObjectVoxelCountTotal_',SpecimenNum,'_GOBJ');
if (strcmp(ObjInterestList{o},'NOfsDV')==1) %catch NOfsDV object case
    file3b =
      strcat('ObjectVoxelCountTotal_',SpecimenNum,'_','STAIN_ArtfctRemv
```

```
    d_Peel10'); %switch back to regular STAIN for this volume fraction
    calculation...
else
   file3b=strcat('ObjectVoxelCountTotal_',SpecimenNum,'_',ObjectLoad);
end
load(strcat(Directory,file3a,'.mat'))
load(strcat(Directory,file3b,'.mat'))
eval(['TotalNumAvailVoxels = ' file3a ';']); %the total number of GOBJ
  voxels in the gauge section
eval(['TotalNumObjVoxels = ' file3b ';']); %the total number of object voxels
  in the gauge section
clearvars ObjectVoxelCountTotal*

%FIGURE 2A: Distance normalization further normalized by volume
  fraction
%of object of interest (PDF) (FailSite)
FIGtwoA=figure(3);
Yvalues1 =
  (ValDistNormNoNAN1.*(TotalNumAvailVoxels/TotalNumObjVoxels));
  %this is the full PDF value (Dnorm further normalized by the volume
  fraction of the feature of interest)
if (LoopCount==1); FIGtwoAxes1=axes(); end
plot(FIGtwoAxes1,Xvalues1,Yvalues1);%Xvalues were already converted
  from voxels to mm (above)
hold(FIGtwoAxes1,'all')
ylim(FIGtwoAxes1,[0 2])%may need to adjust the upper y range... lower
  can't be less than 0
xlim(FIGtwoAxes1,[0 (NumSlicesEval/100)])
box off

%FIGURE 2B: Distance normalization further normalized by volume
  fraction
%of object of interest (PDF) (ALLsummed)
FIGtwoB=figure(4);
Yvalues2 =
  (ValDistNormNoNAN2.*(TotalNumAvailVoxels/TotalNumObjVoxels));
  %this is the full PDF value (Dnorm further normalized by the volume
  fraction of the feature of interest)
if (LoopCount==1); FIGtwoAxes2=axes(); end
plot(FIGtwoAxes2,Xvalues2,Yvalues2);%Xvalues were already converted
  from voxels to mm (above)
hold(FIGtwoAxes2,'all')
ylim(FIGtwoAxes2,[0 2])%may need to adjust the upper y range... lower
  can't be less than 0
xlim(FIGtwoAxes2,[0 (NumSlicesEval/100)])
box off
```

```
%save all plot values
PDF_Xvals(1:length(Xvalues1),s,o,1)=Xvalues1;%FailSite
PDF_Xvals(1:length(Xvalues2),s,o,2)=Xvalues2;%ALLdamage

PDF_Yvals(1:length(Yvalues1),s,o,1)=Yvalues1;%FailSite
PDF_Yvals(1:length(Yvalues2),s,o,2)=Yvalues2;%ALLdamage


CrackDist=[44];%this the number of VOXELS distance at which length a
  crack becomes unstable (Mohsin2006/O'Brien2005) (10 um voxel,
  therefore 44 voxels = 440 µm)

for cd=1:length(CrackDist)
   CrackDistObj1=sum(DistObjBinned_FailSite(1:CrackDist(cd)));%FailSite
   CrackDistObj2 =
    sum(DistObjBinned_ALLsummed(1:CrackDist(cd)));%ALLdamage

   CrackDistAvail1 =
    sum(DistAvailBinned_GOBJvoxels_FailSite(1:CrackDist(cd)));%FailSit
    e
   CrackDistAvail2 =
    sum(DistAvailBinned_GOBJvoxels_ALLsummed(1:CrackDist(cd)));%A
    LLdamage

   CrackDistDnorm(s,o,1,cd)=CrackDistObj1/CrackDistAvail1;%FailSite
   CrackDistDnorm(s,o,2,cd) =
    CrackDistObj2/CrackDistAvail2;%ALLdamage

   CrackDistPDF(s,o,1,cd) =
    CrackDistDnorm(s,o,1,cd)*(TotalNumAvailVoxels/TotalNumObjVoxels
    );%FailSite
   CrackDistPDF(s,o,2,cd) =
    CrackDistDnorm(s,o,2,cd)*(TotalNumAvailVoxels/TotalNumObjVoxels
    );%ALLdamage
end

clear('SpecimenNum','Directory',...
   'file1a','file1b','file2a','file2b',...
   'DistObjBinned_ALLsummed',
     'DistAvailBinned_GOBJvoxels_ALLsummed',...
   'DistObjBinned_FailSite','DistAvailBinned_GOBJvoxels_FailSite',...
   'DistAvailGOBJvoxels_BigBins2','DistObj_BigBins2',...
   'DistAvailGOBJvoxels_BigBins1','DistObj_BigBins1',...
   'DistanceNormBigBins2','DistanceNormBigBins1',...
   'RowsDnormBigBin2','RowsDnormBigBin1',...
```

```
        'ValDistNormNoNANBigBin2','ValDistNormNoNANBigBin1',...
        'Xvalues2','Xvalues1',...
        'TotalNumAvailVoxels','TotalNumObjVoxels','Yvalues2','Yvalues1',...
        'cd')
    clearvars CrackDist* -except CrackDist CrackDistDnorm CrackDistPDF

    Duration=toc(ObjTime);
    DurationMin=floor(Duration/60);
    DurationSec=round(((Duration/60)-DurationMin)*60);
    fprintf(' Complete!  Duration = %d min %d sec\n',DurationMin,DurationSec)
    clear('ObjTime','Duration','DurationMin','DurationSec')
end

site1='FailSite';
site2='AllDamage';

% Fig1A and 1B:  Dnorm figs for 1A: for FailSite cluster, and 1B: All clusters
  summed
FigTitle1A =
  strcat('3D_DnormTPCF_',site1,'_',Object,'_AllSpecimens',SpecficVersionNO
  W);
title(FIGoneAxes1,FigTitle1A,'Interpreter','none')
legend(FIGoneAxes1,SpecimenList)
xlabel(FIGoneAxes1,'Radial Distance from Voxel of Interest [mm]')
ylabel(FIGoneAxes1,'Distance Volume Fraction')
saveas(FIGoneA,strcat('ALL_Dnorm_Plots/',FigTitle1A),'tif')
print(FIGoneA,'-depsc',strcat('ALL_Dnorm_Plots/',FigTitle1A,'.eps'))%saves to
  a color eps file!
hold(FIGoneAxes1,'off')
close(FIGoneA)

FigTitle1B =
  strcat('3D_DnormTPCF_',site2,'_',Object,'_AllSpecimens',SpecficVersionNO
  W);
title(FIGoneAxes2,FigTitle1B,'Interpreter','none')
legend(FIGoneAxes2,SpecimenList)
xlabel(FIGoneAxes2,'Radial Distance from Voxel of Interest [mm]')
ylabel(FIGoneAxes2,'Distance Volume Fraction')
saveas(FIGoneB,strcat('ALL_Dnorm_Plots/',FigTitle1B),'tif')
print(FIGoneB,'-depsc',strcat('ALL_Dnorm_Plots/',FigTitle1B,'.eps'))%saves to
  a color eps file!
hold(FIGoneAxes2,'off')
close(FIGoneB)
```

```
    % Fig2A and 2B:  PDF figs for 2A: for FailSite cluster, and 2B: All clusters
       summed
    FigTitle2A =
      strcat('3D_PDF_',site1,'_',Object,'_AllSpecimens',SpecficVersionNOW);
    title(FIGtwoAxes1,FigTitle2A,'Interpreter','none')
    legend(FIGtwoAxes1,SpecimenList)
    xlabel(FIGtwoAxes1,'Radial Distance from Voxel of Interest [mm]')
    ylabel(FIGtwoAxes1,'PDF (Volume Fraction)/(Total Volume Fraction)')
    saveas(FIGtwoA,strcat('ALL_PDF_Plots/',FigTitle2A),'tif')
    print(FIGtwoA,'-depsc',strcat('ALL_PDF_Plots/',FigTitle2A,'.eps'))%saves to a
      color eps file!
    hold(FIGtwoAxes1,'off')
    close(FIGtwoA)

    FigTitle2B =
      strcat('3D_PDF_',site2,'_',Object,'_AllSpecimens',SpecficVersionNOW);
    title(FIGtwoAxes2,FigTitle2B,'Interpreter','none')
    legend(FIGtwoAxes2,SpecimenList)
    xlabel(FIGtwoAxes2,'Radial Distance from Voxel of Interest [mm]')
    ylabel(FIGtwoAxes2,'PDF (Distance Volume Fraction)/(Total Volume
      Fraction)')
    saveas(FIGtwoB,strcat('ALL_PDF_Plots/',FigTitle2B),'tif')
    print(FIGtwoB,'-depsc',strcat('ALL_PDF_Plots/',FigTitle2B,'.eps'))%saves to a
      color eps file!
    hold(FIGtwoAxes2,'off')
    close(FIGtwoB)

    clear('FigTitle1B','FigTitle1A','FigTitle2B','FigTitle2A',...
       'FIGoneB','FIGoneA','FIGtwoB','FIGtwoA',...
       'FIGoneAxes2','FIGoneAxes1','FIGtwoAxes2','FIGtwoAxes1')

    clear('Object','LoopCount')
end
```

A.2 Probability Density Function (PDF) Calculation Example and Details

A two-dimensional (2-D) schematic example (Figure A.1) is helpful to explain PDF methods employed in this study. In concept, computation of the PDF involves calculating the ratio of the local to overall feature of interest volume fraction at each discrete distance from the voxel of origin. In this way, the PDF value should be

compared to 1 (random probability). PDF values greater than 1 indicate greater than random probability, while PDF values less than 1 indicate less than random probability. Following the example, there are 28 total voxels located at distance *r* from the current voxel of origin. Of those 28 voxels, 5 are PV and 2 are HMV. In this example, the local and overall volume fraction for porosity is 5/28 and 36/400, respectively. Therefore, PV is ~2 times greater than random probability at distance *r*. In contrast, HMV has a local and overall volume fraction of 2/28 and 80/400, respectively, and therefore is approximately half as likely as random probability at distance *r*.

Each PDF was computed in a series of three primary steps (Figure A.1). First, distances between the voxels of origin and all other voxels in the gauge section (within 3 mm from the current voxel of origin—a means of reducing the computation time to include only the more relevant, relatively close voxels) were computed using the 3-D distance formula. Second, 3-D distances between the voxels of origin and each feature of interest (PV, LMV, or HMV) were computed in segmented image volumes in the same manner as in step (1). Each computed distance from steps (1) and (2) was rounded to the nearest integer and a histogram consisting of the occurrence of each integer distance was stored. In the final step, all the feature of interest distance histograms from step (2) (one for each unique voxel of origin) were aggregated and then fully normalized on a local and global scale. The aggregate feature of interest distance histogram, also called a two-point correlation function (Torquato, 2002), was first normalized locally by the volume sampled (step 1) at each discrete distance (i.e., the radial volume fraction) from each unique voxel of origin. The feature of interest distance histogram was further normalized

by the overall volume fraction of the feature of interest, resulting in the PDF for each feature of interest.

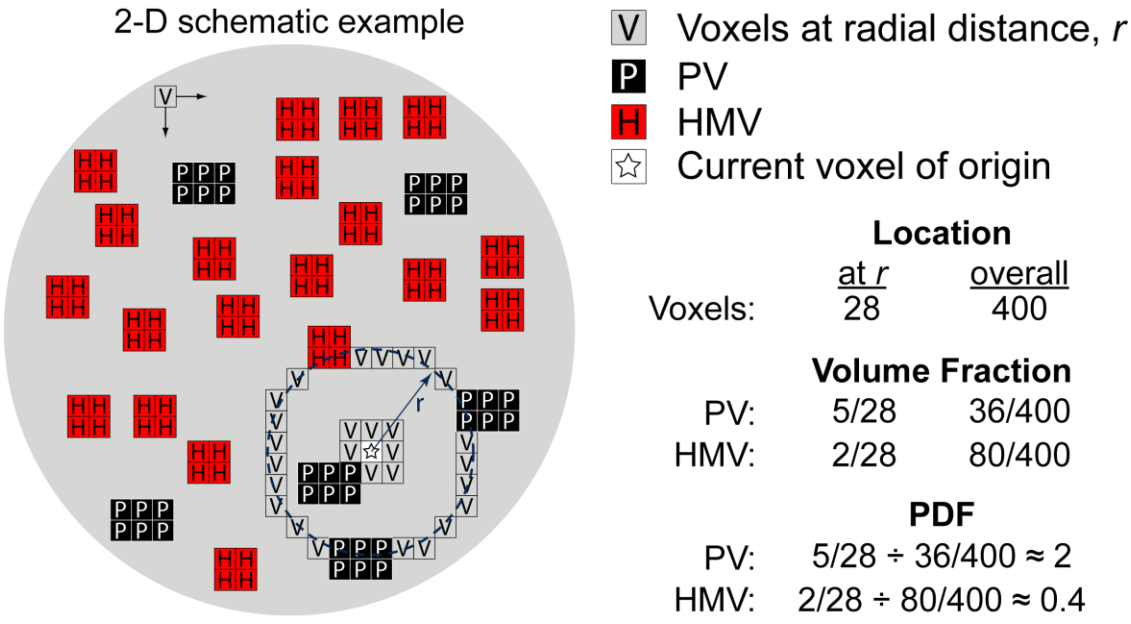

Figure A.1: Schematic diagram in 2-D, for a single voxel of origin illustrating the fundamental concepts and calculations involved for computation of the 3-D normalized two-point correlation function, or probability density function (PDF).

A.3 Inter-specimen Probability Density Function (PDF) Variability for Chapter 3 Specimens

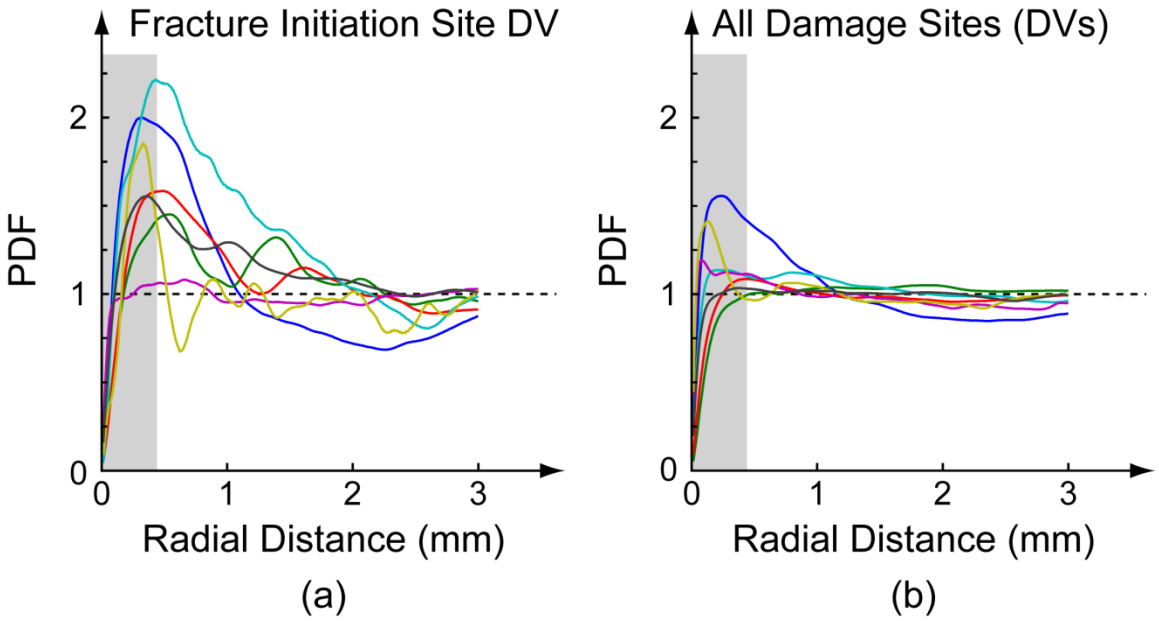

Figure A.2: Individual specimen PDFs for PV near (a) the fracture initiation site damage and (b) all damage sites showing inter-specimen variability. Note that each colored trace represents the PDF for a single specimen and coloring is consistent between locations (a) and (b).

BIBLIOGRAPHY

Akkus, O., Knott, D.F., Jepsen, K.J., Davy, D.T., Rimnac, C.M., 2003. Relationship between damage accumulation and mechanical property degradation in cortical bone: microcrack orientation is important. Journal of Biomedical Materials Research 65A, 482-488.

Albrand, G., Munoz, F., Sornay-Rendu, E., DuBoeuf, F., Delmas, P.D., 2003. Independent predictors of all osteoporosis-related fractures in healthy postmenopausal women: the OFELY Study. Bone 32, 78-85.

Allen, M.R., Burr, D.B., 2011. Bisphosphonate effects on bone turnover, microdamage, and mechanical properties: what we think we know and what we know that we don't know. Bone 49, 56-65.

Anderson, T.L., 2005. Fracture mechanics: fundamentals and applications, 3rd ed. CRC Press, Boca Raton, FL.

Armstrong III, D.W., Rue, J.-P.H., Wilckens, J.H., Frassica, F.J., 2004. Stress fracture injury in young military men and women. Bone 35, 806-816.

Bennell, K., Matheson, G., Meeuwisse, W., Brukner, P., 1999. Risk factors for stress fractures. Sports Medicine 28, 91-122.

Bigley, R.F., Singh, M., Hernandez, C.J., Kazakia, G.J., Martin, R.B., Keeveny, T.M., 2008. Validity of serial milling-based imaging system for microdamage quantification. Bone 42, 212-215.

Blau, M., Ganatra, R., Bender, M., 1972. 18 F-fluoride for bone imaging. Seminars in Nuclear Medicine 2, 31-37.

Bousson, V., Bergot, C., Meunier, A., Barbot, F., Parlier-Cuau, C., Laval-Jeantet, A.-M., Laredo, J.D., 2000. CT of the middiaphyseal femur: cortical bone mineral density and relation to porosity. Radiology 217, 179-187.

Bousson, V., Meunier, A., Bergot, C., Vicaut, E., Rocha, M.A., Morais, M.H., Laval-Jeantet, A.-M., Laredo, J.D., 2001. Distribution of intracortical porosity in human midfemoral cortex by age and gender. Journal of Bone and Mineral Research 16, 1308-1317.

Boyce, T.M., Fyhrie, D.P., Glotkowski, M.C., Radin, E.L., Schaffler, M.B., 1998. Damage type and strain mode associations in human compact bone bending fatigue. Journal of Orthopaedic Research 16, 322-329.

Buckwalter, J.A., Brandser, E.A., 1997. Stress and insufficiency fractures. American Family Physician 56, 175-182.

Burge, R., Dawson-Hughes, B., Solomon, D.H., Wong, J.B., King, A., Tosteson, A., 2007. Incidence and economic burden of osteoporosis-related fractures in the United States, 2005-2025. Journal of Bone and Mineral Research 22, 465-475.

Burghardt, A.J., Buie, H.R., Laib, A., Majumdar, S., Boyd, S.K., 2010a. Reproducibility of direct quantitative measures of cortical bone microarchitecture of the distal radius and tibia by HR-pQCT. Bone 47, 519-528.

Burghardt, A.J., Kazakia, G.J., Ramachandran, S., Link, T.M., Majumdar, S., 2010b. Age- and gender-related differences in the geometric properties and biomechanical significance of intracortical porosity in the distal radius and tibia. Journal of Bone and Mineral Research 25, 983-993.

Burghardt, A.J., Kazakia, G.J., Sode, M., de Papp, A.E., Link, T.M., Majumdar, S., 2010c. A longitudinal HR-pQCT study of alendronate treatment in postmenopausal women with low bone density: relations among density, cortical and trabecular microarchitecture, biomechanics, and bone turnover. Journal of Bone and Mineral Research 25, 2558-2571.

Burr, D.B., 2002. Targeted and nontargeted remodeling. Bone 30, 2-4.

Burr, D.B., Forwood, M.R., Fyhrie, D.P., Martin, R.B., Schaffler, M.B., Turner, C.H., 1997. Bone microdamage and skeletal fragility in osteoporotic and stress fractures. Journal of Bone and Mineral Research 12, 6-15.

Burr, D.B., Hooser, M., 1995. Alterations to the en bloc basic fuchsin staining protocol for the demonstration of microdamage produced *in vivo*. Bone 17, 431-433.

Burr, D.B., Milgrom, C., Fyhrie, D., Forwood, M., Nyska, M., Finestone, A., Hoshaw, S., Saiag, E., Simkin, A., 1996. *In vivo* measurement of human tibial strains during vigorous activity. Bone 18, 405-410.

Burr, D.B., Schaffler, M.B., Frederickson, R.G., 1988. Composition of the cement line and its possible mechanical role as a local interface in human compact bone. Journal of Biomechanics 21, 939-945.

Burr, D.B., Stafford, T., 1990. Validity of the bulk-staining technique to separate artifactual from *in vivo* bone microdamage. Clinical Orthopaedics and Related Research 260, 305-308.

Burr, D.B., Turner, C.H., Naick, P., Forwood, M.R., Ambrosius, W., Hasan, M.S., Pidaparti, R., 1998. Does microdamage accumulation affect the mechanical properties of bone? Journal of Biomechanics 31, 337-345.

Chapurlat, B.D., Delmas, P.D., 2009. Bone microdamage: a clinical perspective. Osteoporosis International 20, 1299-1308.

Currey, J.D., 1962. Stress concentrations in bone. Quarterly Journal of Microscopical Science 103, 111-133.

Currey, J.D., 1988. The effect of porosity and mineral content on the Young's modulus of elasticity of compact bone. Journal of Biomechanics 21, 131-139.

Danova, N.A., Colopy, S.A., Radtke, C.L., Kalscheur, V.L., Markel, M.D., Vanderby Jr., R., McCabe, R.P., Escarcega, A.J., Muir, P., 2003. Degradation of bone structural properties by accumulation and coalescence of microcracks. Bone 33, 197-205.

Deuerling, J.M., Rudy, D.J., Niebur, G.L., Roeder, R.K., 2010. Improved accuracy of cortical bone mineralization measured by polychromatic microcomputed tomography using a novel high mineral density composite calibration phantom. Medical Physics 37, 5138-5145.

Diab, T., Vashishth, D., 2005. Effects of damage morphology on cortical bone fragility. Bone 37, 96-102.

Fazzalari, N.L., Forwood, M.R., Manthey, B.A., Smith, K., Kolesik, P., 1998. Three-dimensional confocal images of microdamage in cancellous bone. Bone 23, 373-378.

Feik, S.A., Thomas, C.D.L., Clement, D.B., 1997. Age-related changes in cortical porosity of the midshaft of the human femur. Journal of Anatomy 191, 407-416.

Fleck, C., Eifler, D., 2003. Deformation behaviour and damage accumulation of cortical bone specimens from the equine tibia under cyclic loading. Journal of Biomechanics 36, 179-189.

Forwood, M.R., Parker, A.W., 1989. Microdamage in response to repetitive torsional loading in the rat tibia. Calcified Tissue International 45, 47-53.

Frost, H.M., 1960. Presence of microscopic cracks *in vivo* in bone. Henry Ford Hospital Medical Bulletin 8, 27-35.

Gargac, J.A., Turnbull, T.L., Roeder, R.K., Niebur, G.L., 2013. A probabilistic damage model based on direct 3-D correlation of strain to damage formation following fatigue loading of rat remora. In preparation for submission to: Journal of the Mechanical Behavior of Biomedical Materials.

Genant, H.K., Bautovich, G.J., Singh, M., Lathrop, K.A., Harper, P.V., 1974. Bone-seeking radionuclides: an *in vivo* study of factors affecting skeletal uptake. Radiology 113, 373-382.

Genant, H.K., Engelke, K., Fuerst, T., Gluer, C.-C., Grampp, S., Harris, S.T., Jergas, M., Lang, T., Lu, Y., Majumdar, S., Mathur, A., Takada, M., 1996. Noninvasive assessment of bone mineral and structure: state of the art. Journal of Bone and Mineral Research 11, 707-730.

Hirano, T., Turner, C.H., Forwood, M.R., Johnston, C.C., Burr, D.B., 2000. Does suppression of bone turnover impair mechanical properties by allowing microdamage accumulation? Bone 27, 13-20.

Kazakia, G.J., Burghardt, A.J., Link, T.M., Majumdar, S., 2011. Variations in morphological and biomechanical indices at the distal radius in subjects with identical BMD. Journal of Biomechanics 44, 257-266.

Kennedy, O.D., Brennan, O., Mauer, P., Rackard, S.M., O'Brien, F.J., Taylor, D., Lee, T.C., 2008. The effects of increased intracortical remodeling on microcrack behaviour in compact bone. Bone 43, 889-893.

Kennedy, O.D., Brennan, O., Rackard, S.M., Staines, A., O'Brien, F.J., Taylor, D., Lee, T.C., 2009. Effects of ovariectomy on bone turnover, porosity, and biomechanical properties in ovine compact bone 12 months postsurgery. Journal of Orthopaedic Research 27, 303-309.

Klein-Nulend, J., Bonewald, L.F., 2008. The Osteocyte, in: Bilezikian, J.P., Raisz, L.G., Martin, T.J. (Eds.), Principles of Bone Biology (3rd ed.), 3 ed. Elsevier: Academic Press, San Diego.

Koester, K.J., Ager III, J.W., Ritchie, R.O., 2008. The true toughness of human cortical bone measured with realisitically short cracks. Nature Materials 7, 672-677.

Kotha, S.P., Hsieh, Y.-F., Strigel, R.M., Müller, R., Silva, M.J., 2004. Experimental and finite element analysis of the rat ulnar loading model—correlations between strain and bone formation following fatigue loading. Journal of Biomechanics 37, 541-548.

Landrigan, M.D., Flatley, J.C., Turnbull, T.L., Kruzic, J.J., Ferracane, J.L., Hilton, T.J., Roeder, R.K., 2010. Detection of dentinal cracks using contrast-enhanced micro-computed tomography. Journal of the Mechanical Behavior of Biomedical Materials 3, 223-227.

Landrigan, M.D., Li, J., Turnbull, T.L., Burr, D.B., Niebur, G.L., Roeder, R.K., 2011. Contrast-enhanced micro-computed tomography of fatigue microdamage accumulation in human cortical bone. Bone 48, 443-450.

Landrigan, M.D., Roeder, R.K., 2009. Systematic error in mechanical measures of damage during four-point bending fatigue of cortical bone. Journal of Biomechanics 42, 1212-1217.

Lanyon, L.E., 1980. The influence of function on the development of bone curvature. An experimental study on the rat tibia. Journal of Zoology 192, 457-466.

Lanyon, L.E., Hampson, W.G.J., Goodship, A.E., Shah, J.S., 1975. Bone deformation recorded *in vivo* from strain gauges attached to the human tibial shaft. Acta Orthopaedica Scandinavica 46, 256-268.

Lee, T.C., Arthur, T.L., Gibson, L.J., Hayes, W.C., 2000. Sequential labelling of microdamage in bone using chelating agents. Journal of Orthopaedic Research 18, 322-325.

Lee, T.C., Mohsin, S., Taylor, D., Parkesh, R., Gunnlaugsson, T., O'Brien, F.J., Giehl, M., Gowin, W., 2003. Detecting microdamage in bone. Journal of Anatomy 203, 161-172.

Lee, T.C., Myers, E.R., Hayes, W.C., 1998. Fluorescence-aided detection of microdamage in compact bone. Journal of Anatomy 193, 179-184.

Lees, S., Davidson, C.L., 1977. The role of collagen in the elastic properties of calcified tissues. Journal of Biomechanics 10, 473-486.

Leibson, C.L., Tosteson, A.N., Gabriel, S.E., Ransom, J.E., Melton, L.J., 2002. Mortality, disability, and nursing home use for persons with and without hip fracture: a population-based study. Journal of the American Geriatric Society 50, 1644-1650.

Lenart, B.A., Lorich, D.G., Lane, J.M., 2008. Atypical fractures of the femoral diaphysis in postmenopausal women taking alendronate. New England Journal of Medicine 258, 1304-1306.

Leng, H., 2006. Micro-computed tomography of microdamage in cortical bone., University of Notre Dame, Notre Dame, IN.

Leng, H., Wang, X., Ross, R.D., Niebur, G.L., Roeder, R.K., 2008. Micro-computed tomography of fatigue microdamage in cortical bone using a barium sulfate contrast agent. Journal of the Mechanical Behavior of Biomedical Materials 1, 68-75.

Li, J., Miller, M.A., Hutchins, G.D., Burr, D.B., 2005. Imaging bone microdamage *in vivo* with positron emission tomography. Bone 37, 819-824.

Liu, X.S., Zhang, X.H., Sekhon, K.K., Adams, M.F., McMahon, D.J., Bilezikian, J.P., Shane, E., Guo, X.E., 2010. High-resolution peripheral quantitative computed tomography can assess microstructural and mechanical properties of human distal tibial bone. Journal of Bone and Mineral Research 25, 746-756.

Macdonald, H.M., Nishiyama, K.K., Kang, J., Hanley, D.A., Boyd, S.K., 2011. Age-related patterns of trabecular and cortical bone loss differ between sexes and skeletal sites: a population-based HR-pQCT study. Journal of Bone and Mineral Research 26, 50-62.

MacNeil, J.A., Boyd, S.K., 2008. Bone strength at the distal radius can be estimated from high-resolution peripheral quantitative computed tomography and the finite element method. Bone 42, 1203-1213.

Marshall, D., Johnell, O., Wedel, H., 1996. Meta-analysis of how well measures of bone mineral density predict occurrence of osteoporotic fractures. British Medical Journal 312, 1254-1259.

Martin, R.B., 1995. Mathematical model for repair of fatigue damage and stress fracture in osteonal bone. Journal of Orthopaedic Research 13, 309-316.

Martin, R.B., Burr, D.B., 1982. A hypothetical mechanism for the stimulation of osteonal remodelling by fatigue damage. Journal of Biomechanics 15, 137-139.

Matheson, G.O., Clement, D.B., McKenzie, D.C., Taunton, J.E., Lloyd-Smith, D.R., MacIntyre, J.G., 1987. Stress fractures in athletes. The American Journal of Sports Medicine 15, 46-58.

Milgrom, C., Finestone, A., Simkin, A., Ekenman, I., Mendelson, S., Millgram, M., Nyska, M., Larsson, E., Burr, D.B., 2000. *In vivo* strain measurements to evaluate the strengthening potential of exercises on the tibial bone. Journal of Bone and Joint Surgery 82-B, 591-594.

Miller, P.D., Siris, E.S., Barrett-Connor, E., Faulkner, K.G., Wehren, L.E., Abbott, T.A., Chang, Y.-T., Berger, M.L., Santora, A.C., Sherwood, L.M., 2002. Prediction of fracture risk in postmenopausal women with peripheral bone densiometry: evidence from the National Osteoporosis Risk Assessment. Journal of Bone and Mineral Research 17, 2222-2230.

Mohsin, S., O'Brien, F.J., Lee, T.C., 2006a. Microcracks in compact bone: a three-dimensional view. Journal of Anatomy 209, 119-124.

Mohsin, S., O'Brien, F.J., Lee, T.C., 2006b. Osteonal crack barriers in ovine compact bone. Journal of Anatomy 208, 81-89.

MOMRP Fact Sheet, A., 1999. Bone health and military medical readiness, in: Program, M.O.M.R. (Ed.), MOMRP Fact Sheet Number 2. USAMRMC, Military Operational Medicine Research Program, Fort Detrick, MD, Fort Detrick, MD.

Moradian-Oldak, J., Weiner, S., Addadi, L., Landis, W.J., Traub, W., 1991. Electron imaging and diffraction study of individual crystals of bone, mineralized tendon and synthetic carbonate apatite. Connective Tissue Research 25, 219-228.

Moreno, L.D., Waldman, S.D., Grynpas, M.D., 2006. Sex differences in long bone fatigue using a rat model. Journal of Orthopaedic Research 24, 1926-1932.

Nalla, R.K., Kruzic, J.J., Kinney, J.H., Ritchie, R.O., 2005. Mechanistic aspects of fracture and R-curve behavior in human cortical bone. Biomaterials 26, 217-231.

Norman, T.L., Little, T.M., Yeni, Y.N., 2008. Age-related changes in porosity and mineralization and in-service damage accumulation. Journal of Biomechanics 41, 2868-2873.

Norman, T.L., Wang, Z., 1997. Microdamage of human cortical bone: incidence and morphology in long bones. Bone 20, 375-379.

Norman, T.L., Yeni, Y.N., Brown, C.U., Wang, X., 1998. Influence of microdamage on fracture toughness of the human femur and tibia. Bone 23, 303-306.

Nyman, J.S., Leng, H., Dong, X.N., Wang, X., 2009. Differences in the mechanical behavior of cortical bone between compression and tension when subjected to progressive loading. Journal of the Mechanical Behavior of Biomedical Materials 2, 613-619.

Nyman, J.S., Reyes, M., Wang, X., 2005. Effect of ultrastructural changes on the toughness of bone. Micron 36, 566-582.

O'Brien, F.J., Taylor, D., Dickson, G.R., Lee, T.C., 2000. Visualization of three-dimensional microcracks in compact bone. Journal of Anatomy 197, 413-420.

O'Brien, F.J., Taylor, D., Lee, T.C., 2002. An improved labelling technique for monitoring microcrack growth in compact bone. Journal of Biomechanics 35, 523-526.

O'Brien, F.J., Taylor, D., Lee, T.C., 2003. Microcrack accumulation at different intervals during fatigue testing of compact bone. Journal of Biomechanics 36, 973-980.

Parkesh, R., Lee, T.C., Gunnlaugsson, T., 2009. Fluorescence imaging of bone cracks (microdamage) using visibly emitting 1,8-naphthalimide-based PET sensors. Tetrahedron Letters 50, 4114-4116.

Parkesh, R., Lee, T.C., Gunnlaugsson, T., Gowin, W., 2006. Microdamage in bone: surface analysis and radiological detection. Journal of Biomechanics 39, 1552-1556.

Parkesh, R., Mohsin, S., Lee, T.C., Gunnlaugsson, T., 2007. Histological, spectroscopic, and surface analysis of microdamage in bone: toward real-time analysis using fluorescent sensors. Chemical Materials 19, 1656-1663.

Pattin, C.A., Calert, W.E., Carter, D.R., 1996. Cyclic mechanical property degradation during fatigue loading of cortical bone. Journal of Biomechanics 29, 69-79.

Placide, J., Martens, M.G., 2003. Comparing screening methods for osteoporosis. Current Women's Health Reports 3, 207-210.

Raum, K., Leguerney, I., Chandelier, F., Talmant, M., Saied, A., Peyrin, F., Laugier, P., 2006. Site-matched assessment of structural and tissue properties of cortical bone using scanning acoustic microscopy and synchrotron radiation μCT. Physics in Medicine and Biology 51, 733-746.

Reilly, G.C., Currey, J.D., 1999. The development of microcracking and failure in bone depends on the loading mode to which it is adapted. The Journal of Experimental Biology 202, 543-552.

Reilly, G.C., Currey, J.D., 2000. The effects of damage and microcracking on the impact strength of bone. Journal of Biomechanics 33, 337-343.

Rho, J.-Y., Kuhn-Spearing, L., Zioupos, P., 1998. Mechanical properties and the hierarchical structure of bone. Medical Engineering and Physics 20, 92-102.

Roeder, R.K., 2013. Mechanical characterization of biomaterials, in: Bandyopadhyay, A., Bose, S. (Eds.), Characterization of biomaterials. Elsevier, Waltham, MA.

Ross, R.D., Roeder, R.K., 2010. Functionalized gold nanoparticles for targeted labeling of damaged bone tissue in X-ray tomography. Transactions of the Orthopaedic Research Society 35, 1368.

Ross, R.D., Roeder, R.K., 2011. Binding affinity of surface functionalized gold nanoparticles to hydroxyapatite. Journal of Biomedical Materials Research Part A 99A, 58-66.

Sanders, K.M., Nicholson, G.C., Watts, J.J., Pasco, J.A., Henry, M.J., Kotowicz, M.A., Seeman, E., 2006. Half the burden of fragility fractures in the community occur in women without osteoporosis. When is fracture prevention cost-effective? Bone 38, 694-700.

Schaffler, M.B., Burr, D.B., 1988. Stiffness of compact bone: effects of porosity and density. Journal of Biomechanics 21, 13-16.

Schaffler, M.B., Choi, K., Milgrom, C., 1995. Aging and matrix microdamage accumulation in human compact bone. Bone 17, 521-525.

Schaffler, M.B., Pitchford, W.C., Choi, K., Riddle, J.M., 1994. Examination of compact bone microdamage using back-scattered electron microscopy. Bone 15, 483-488.

Schaffler, M.B., Radin, E.L., Burr, D.B., 1989. Mechanical and morphological effects of strain rate on fatigue of compact bone. Bone 10, 207-214.

Seeman, E., 2009. To stop or not to stop, that is the question. Osteoporosis International 20, 187-195.

Seeman, E., Delmas, P.D., 2006. Bone quality — the material and structural basis of bone strength and fragility. New England Journal of Medicine 354, 2250-2261.

Shi, N., Foley, K., Lenhart, G., Badamgarav, E., 2009. Direct healthcare costs of hip, vertebral, and non-hip, non-vertebral fractures. Bone 45, 1084-1090.

Silva, M.J., Uthgenannt, B.A., Rutlin, J.R., Wohl, G.R., Lewis, J.S., Welch, M.J., 2006. *In vivo* skeletal imaging of 18F-fluoride with positron emission tomography reveals damage- and time-dependent responses to fatigue loading in the rat ulna. Bone 39, 229-236.

Siris, E.S., Miller, P.D., Barrett-Connor, E., Faulkner, K.G., Wehren, L.E., Abbott, T.A., Berger, M.L., Santora, A.C., Sherwood, L.M., 2001. Identification and fracture outcomes of undiagnosed low bone mineral density in postmenopausal women. Journal of the American Medical Association 286, 2815-2822.

Soicher, M.A., Wang, X., Zauel, R.R., Fyhrie, D.P., 2011. Damage initiation sites in osteoporotic and normal human cancellous bone. Bone 48, 663-666.

Sornay-Rendu, E., Boutroy, S., Munoz, F., Delmas, P.D., 2007. Alterations of cortical and trabecular architecture are associated with fractures in postmenopausal women, partially independent of decreased BMD measured by DXA: the OFELY Study. Journal of Bone and Mineral Research 22, 425-433.

Sornay-Rendu, E., Munoz, F., Garnero, P., Duboeuf, F., Delmas, P.D., 2005. Identification of osteopenic women at high risk of fracture: the OFELY Study. Journal of Bone and Mineral Research 20, 1813-1819.

Stein, M.S., Feik, S.A., Thomas, C.D.L., Clement, J.G., Wark, J.D., 1999. An automated analysis of intracortical porosity in human femoral bone across age. Journal of Bone and Mineral Research 14, 624-632.

Swanson, M.B., Davis, G.A., Kincaid, L.E., Schultz, T.W., Bartmess, J.E., Jones, S.L., George, E.L., 1997. A screening method for ranking and scoring chemicals by potential human health and environmental impacts. Environmental Toxicology and Chemistry 16, 372-383.

Tang, S.Y., Vashishth, D., 2007. A non-invasive *in vitro* technique for the three-dimensional quantification of microdamage in trabecular bone. Bone 40, 1259-1264.

Taylor, D., Hazenberg, J.G., Lee, T.C., 2007. Living with cracks: damage and repair in human bone. Nature Materials 6, 263-268.

Thomas, C.D.L., Feik, S.A., Clement, J.G., 2005. Regional variation of intracortical porosity in the midshaft of the human femur: age and sex differences. Journal of Anatomy 206, 115-125.

Torquato, S., 2002. Random heterogeneous materials: microstructure and macroscopic properties, in: Antman, S.S., Marsden, J.E., Sirovich, L., Wiggins, S. (Eds.), Interdisciplinary applied mathematics. Springer-Verlag, New York, NY.

Turnbull, T.L., Gargac, J.A., Niebur, G.L., Roeder, R.K., 2011. Detection of fatigue microdamage in whole rat femora using contrast-enhanced micro-computed tomography. Journal of Biomechanics 44, 2395-2400.

Turner, C.H., Burr, D.B., 1993. Basic biomechanical measurements of bone: a tutorial. Bone 14, 595-608.

Ural, A., Vashishth, D., 2007. Effects of intracortical porosity on fracture toughness in aging human bone: a μCT-based cohesive finite element study. Journal of Biomechanical Engineering 129, 625-631.

Uthgenannt, B.A., Silva, M.J., 2007. Use of the rat forelimb compression model to create discrete levels of bone damage in vivo. Journal of Biomechanics 40, 317-324.

Valimaki, V.-V., Alfthan, H., Lehmuskallio, E., Loyttyniemi, E., Sahi, T., Suominen, H., Valimaki, M.J., 2005. Risk factors for clinical stress fractures in male military recruits: a prospective cohort study. Bone 37, 267-273.

van Lenthe, G.H., Voide, R., Boyd, S.K., Müller, R., 2008. Tissue modulus calculated from beam theory is biased by bone size and geometry: implications for the use of three-point bending tests to determine bone tissue modulus. Bone 43, 717-723.

Voide, R., Schneider, P., Stauber, M., Wyss, P., Stampanoni, M., Sennhauser, U., van Lenthe, G.H., Müller, R., 2009. Time-lapsed assessment of microcrack initiation and propagation in murine cortical bone at submicrometer resolution. Bone 45, 164-173.

Wang, X., Masse, D.B., Leng, H., Hess, K.P., Ross, R.D., Roeder, R.K., Niebur, G.L., 2007. Detection of trabecular bone microdamage by micro-computed tomography. Journal of Biomechanics 40, 3397-3403.

Wasserman, N., Yerramshetty, J., Akkus, O., 2005. Microcracks colocalize within highly mineralized regions of cortical bone tissue. European Journal of Morphology 42, 43-51.

Yeni, Y.N., Brown, C.U., Wang, Z., Norman, T.L., 1997. The influence of bone morphology on fracture toughness of the human femur and tibia. Bone 21, 453-459.

Zebaze, R.M.D., Ghasem-Zadeh, A., Bohte, A., Juliano-Burns, S., Mirams, M., Price, R.I., Mackie, E.J., Seeman, E., 2010. Intracortical remodeling and porosity in the distal radius and post-mortem femurs of women: a cross-sectional study. Lancet 375, 1729-1736.

Zhang, Z., Ross, R.D., Roeder, R.K., 2010. Preparation of functionalized gold nanoparticles as a targeted X-ray contrast agent for damaged bone tissue. Nanoscale 2, 582-586.

Zioupos, P., 2001. Accumulation of *in vivo* fatigue microdamage and its relation to biomechanical properties in ageing human cortical bone. Journal of Microscopy 201, 270-278.

Zioupos, P., Currey, J.D., 1994. The extent of microcracking and the morphology of microcracks in damaged bone. Journal of Materials Science 29, 978-986.

Zioupos, P., Wang, X.T., Currey, J.D., 1996. The accumulation of fatigue microdamage in human cortical bone of two different ages *in vitro*. Clinical Biomechanics 11, 365-375.